Masses, Dynamics and Shock Kinematics of Coronal Mass Ejections

A dissertation submitted to the University of Dublin
for the degree of *Philosophiæ Doctor (PhD)*

Eoin P. Carley
Supervisor: Dr. Peter T. Gallagher
Trinity College Dublin, December 2013

School of Physics
University of Dublin
Trinity College

Declaration

I declare that this thesis has not been submitted as an exercise for a degree at this or any other university and it is entirely my own work.

I agree to deposit this thesis in the University's open access institutional repository or allow the library to do so on my behalf, subject to Irish Copyright Legislation and Trinity College Library conditions of use and acknowledgement.

Name: Eoin Carley

Signature: .... **Date:** ....

Summary

Coronal mass ejections (CMEs) are large-scale eruptions of magnetized plasma from the low solar atmosphere into interplanetary space. With energies of up to 10^{26} J, they are the most energetic eruptive phenomena in the solar system and are also the driver of plasma shocks from the corona into the heliosphere. Despite many years of study, the nature of the forces governing their eruption, and the kinematical behavior of the resulting shock, remain poorly understood. This thesis will presents the first accurate calculation of the magnitude of the total force on a CME. I will also show a previously unseen plasma shock behavior that sheds new light into the kinematical nature of CME-driven shocks in the corona.

In the past, measurement of the forces governing the propagation of CMEs have been hindered by highly uncertain estimates of the total mass of the ejection. The primary source of uncertainty is the unknown position and geometry of the CME, leading to an erroneous treatment of the Thomson scattering equations which are used to estimate the mass. Geometrical uncertainty on the CMEs position and size has primarily been due to observations of the eruption from a single vantage point. However, with the launch of the STEREO spacecraft, the two viewpoints can be exploited to derive the CMEs position and size, ultimately resulting in mass uncertainty that is both reliably quantified and much reduced. These much better estimates for the mass can then be combined with kinematical results that are also more reliable and hence lead to the first reliable quantification of the total force acting on the CME. Using the magnetohydrodynamical equation of motion, the relative sizes of the forces at each stage

in the CME propagation are estimated, revealing the Lorentz force is the largest source of CME acceleration early in its propagation. Quantification of the Lorentz force magnitude from observations has never been achieved in the past.

The second part of this thesis will involve an investigation into the behaviour of radio bright shocks driven by CMEs. CMEs often erupt at speeds in excess of the local MHD wave speeds in the corona. Traveling in excess of Mach 1, they often drive shocks which can have a variety of observational manifestations, such as radio bursts, coronal bright fronts, to the in-situ detection of solar energetic particles. Despite such a variety of shock phenomena being observed for decades, the unifying physical mechanism remains unknown. This thesis will provide an analysis that clearly shows this mechanism to be a shock driven by CME flank expansion which resulted in particle acceleration, radio bursts, and coronal bright front propagating in the low corona. This previously unseen behavior sheds new light on the physics governing radio burst generation and the relationship to CMEs and EUV pulses.

For my parents.

Acknowledgements

Some sincere acknowledgements...

List of Publications

1. **Carley, E. P.**, MacAteer, R. T. J., & Gallagher, P. T.
"Coronal Mass Ejection Masses, Energies, and Force Estimates Using *STEREO*",
The Astrophysical Journal, Volume 752, Issue 1, article id. 36, 8 pp. (2012).

2. Zucca, P., **Carley, E. P.**, McCauley, J., Gallagher, P. T. ,Monstein, C., & MacAteer, R. T. J.,
"Observations of Low Frequency Solar Radio Bursts from the Rosse Solar-Terrestrial Observatory",
Solar Physics, Volume 280, Issue 2, pp.591-602. (2012).

3. **Carley, E. P.**, Long, D. M., Byrne P. J., Zucca, P., & Gallagher, P. T.
"Quasi-periodic Acceleration of Electrons by a Plasmoid Driven Shock in the Solar Atmosphere ",
Nature Physics, in press

4. Zucca, P., **Carley, E. P.**, Bloomfield, S. D., & Gallagher, P. T.
"Density and Alfvén....",
Some Journal, Volume X, Issue Y, article id. (2013)

5. Bloomfield, S. D., **Carley, E. P.**,
"A Comprehensive Overview of the 2011 June 7 Solar Storm",
Astronomy & Astrophysics, Volume X, Issue Y, article id. (2013)

Contents

List of Figures

List of Tables

1
Introduction

The Sun has long been the focus of humanity's curiosity. Throughout history it has been the harbinger of new religions, philosophies, and sciences. It has changed our understanding of our place in the Universe and allowed us to push forward the frontiers of stellar astronomy. Although our understanding of the Sun is nowadays more advanced, the curiosity we hold for it has not changed since the very early humans. Now, we understand the Sun is a star similar to any other in its class, currently going through a relatively unchanging 11 year cycle of activity that is extremely rich in physical complexity. The study of such complex phenomena has yielded immeasurable advances in many areas of physics such as spectroscopy, plasma physics, magnetohydrodynamics (MHD), particle physics, to name but a few. Although some of these sciences have grown over decades (or even centuries) they are still incomplete. I hope this theses will contribute to the continuing growth of these sciences and to the understanding of our nearest star.

1.1 The Sun

The Sun is our nearest star, located 1.49×10^6 km from Earth at the centre of our solar system. Located on the main sequence of the Hetzpring-Russel (HR) diagram, it has a spectral class of G2V, with a luminosity of $L_\odot = (3.84 \pm 0.04) \times 10^{26}$ W, mass of $M_\odot = (1.989 \pm 0.0003) \times 10^{30}$ kg and radius of $R_\odot = (6.959 \pm 0.007) \times 10^8$ m (Foukal, 2004). It was born approximately 4.6×10^9 years ago when a giant molecular cloud underwent gravitational collapse and began hydrogen nuclear fusion at its centre (reference). The energy produced from this fusion resulted in enough pressure to counteract gravitational contraction and bring about a hydrostatic equilibrium, allowing the young star to reach a stability that is sustained today. It is estimated the Sun will maintain this stability for another 5 billion years, at which point, it will move off the main sequence and into a red giant phase. During this later part of its life, it will grow in size to 100 times its current radius and begin nuclear burning of heavier elements such as carbon and oxygen. Once carbon burning in the core has ceased it can no longer sustain nuclear fusion of heavier elements, resulting in a gravitational instability that will eventually lead to a stellar nova. This nova will result in the loss of the outer envelopes and ultimately the Sun's death, leaving behind a compact and dense white-dwarf.

Until such time, the Sun will remain on the main sequence in a regular state of hydrogen fusion in its core. The energy released during this process is the ultimate source of light and all energetic activity that we observe from Earth and beyond. Before we can understand how this energy manifests in the solar atmosphere as a variety of energetic phenomena, it is important to understand how the energy is generated and transported through its interior and finally released into its atmosphere and interplanetary space.

1.1.1 Solar Interior

The theoretical development on how the solar interior is structured and how it behaves has been through what is known as the 'standard solar model' or SSM. The SSM is a grouping of theories that described how the Sun was formed, how it maintains its stability, how it generates energy, and how this energy is transported through its interior and released at the surface. Much of the major developments of this theory have been in the 20th century, due mainly to the pioneering experiments in solar neutrino physics and helioseismsology. Hence, the development of the SSM has mainly been through a refinement of the theory based on these observational fields. Although the SSM has increased in sophistication, its four main aspects remain the most general framework for describing the behavior of the solar interior.

The SSM firstly states that the Sun was born from the gravitational collapse of a primordial gas of hydrogen, helium, and traces of other heavy elements. Secondly, it maintains its structural stability via a hydrostatic equilibrium such that the gravitational force is balanced by a pressure gradient ($\nabla P = -\rho g$) at each radial distance inside the star. The third main aspect of the SSM involves the source of the Sun's energy. Much of the early ideas proposed during the 19th century involved some form of chemical reaction or energy released during a slow gravitational contraction. However, during the first half of the 20th century the theory that the Sun is at least as old as the Earth began to come into focus. The idea of the Sun being more than 4.5 billion years old prompted the question of what energy source could sustain the Sun's luminosity for such a length of time. It was soon realised that thermonuclear fusion must be the source of such energy, and, as a result, it should be possible to observe the neutrino products of this fusion. Hence, starting in the 1950s a number of pioneering neutrino physics experiments were developed in an attempt to detect solar-generated neutrinos at Earth. These pioneering experiments, as well as there more sophisticated counterparts today, confirm much of the theories on solar core energy generation.

From the 1950s onwards there has been a confirmed detection of neutrinos generated in a hydrogen fusion process, namely the proton-proton or 'pp'-chain, in the solar core. In this process, four protons are fused to form a helium nucleus. This can occur in a variety of ways, but at the Sun's core temperature of 15 MK, the dominant reaction is the pp 1 chain given by

$$ {}^{1}_{1}\mathrm{H} + {}^{1}_{1}\mathrm{H} \rightarrow {}^{2}_{1}\mathrm{H} + e^{+} + \nu_e \tag{1.1} $$

$$ {}^{2}_{1}\mathrm{H} + {}^{1}_{1}\mathrm{H} \rightarrow {}^{3}_{2}\mathrm{He} + \gamma \tag{1.2} $$

$$ {}^{3}_{2}\mathrm{He} + {}^{3}_{2}\mathrm{He} \rightarrow {}^{4}_{2}\mathrm{He} + 2\,{}^{1}_{1}\mathrm{H} \tag{1.3} $$

where ${}^{1}_{1}\mathrm{H}$ is a hydrogen nucelus, ${}^{2}_{1}\mathrm{H}$ is deuterium, ${}^{3}_{2}\mathrm{He}$ is tritium, ${}^{4}_{2}\mathrm{He}$ is helium, e^{+} is a positron, ν_e is an electron neutrino, and γ is a gamma ray photon. Reactions (1.1) and (1.2) must happen twice for (1.3) to occur. Taking this into account, the entire process may be summarised as

$$ 4\,{}^{1}_{1}\mathrm{H} \rightarrow {}^{4}_{2}\mathrm{He} + 2e^{+} + 2\nu_e + 2\gamma \tag{1.4} $$

liberating 4.2×10^{-12}J of energy, with $\sim 2.4\%$ of the energy carried away by the neutrinos. This particular form of the pp-chain (pp 1) occurs in 86% of the cases (Turck-Chièze & Couvidat, 2011). However, there are other reactions capable of producing He from H catagorized into pp II, pp III etc, which each involve production of ${}^{7}_{4}\mathrm{Be}$ and ${}^{8}_{5}\mathrm{B}$ (Davis *et al.*, 1968).. These early detections and the results of more recent experiments such as the SuperKamiokande (Fukuda *et al.*, 1998) show that the expected neutrino flux given by the standard solar model is smaller than the observed. This deficit in in neutrino flux observations became the famed 'solar neutrino problem' during the 1970s. One of the proposed explanations for the neutrino deficit was via an oscillation of the neutrino amongst three sets of 'flavors' i.e., the neutrino can be either an electron ν_e, muon ν_μ, or tau ν_τ neutrino, of which only one flavor was detected. This oscillation amongst three flavors was given the name the 'MSW effect' after Mikheev & Smirnov (1986) and Wolfenstein (1978), and later confirmed experimentally by the SuperKamionkande experiment.

The neutrino experiments together with the standard solar model SSM provide much of what we know about the solar energy generation and the solar core. They imply a temperature of 15.6×10^6K and density of $1.48 \times 10^5\,\mathrm{kg\,m^{-3}}$ at solar centre, where energy generation is via fusion which occurs $0.0 - 0.25\,R_\odot$ (Figure 1.1). This range in heights defines the solar core and outside this range Outside the core the temperature drops to a value such that fusion ceases. While thermonuclear fusion is the third aspect of the SSM involves the generation of solar energy, the fourth aspect involves exactly what happens to this energy once it is generated i.e., it describes an energy transport mechanism.

Beyond $0.25\,R_\odot$ the temperature drops to 8 MK, such that fusion stops but only free protons and electrons exist. In this environment, the photons continuously scatter off free particles, undergoing a random walk toward the surface over a distance of $0.25 - 0.7\,R_\odot$. This region is known as the radiative zone and has densities of $2 \times 10^4 - 2 \times 10^2\,\mathrm{kg\,m^{-3}}$, resulting in a small photon mean free path (mfp) of 9.0×10^{-4} m. The photons proceed towards the solar surface over a very long time scale, taking on the order of 10^5 years to traverse this region (Mitalas

& Sills, 1992). If radiative energy transport occurs, it will result in the following temperature gradient

$$\frac{dT}{dr} = -\frac{3}{16\sigma}\frac{\kappa\rho}{T^3}F_{rad} \tag{1.5}$$

where σ is the Stefan-Boltzman constant, κ is the mass extinction coefficient (opacity per unit mass), ρ is mass density, T is temperature, and F_{rad} is the outward radiative flux. This implies that for a particular outward flux, if the opacity increases, a steeper temperature gradient is required to maintain such a flux. At $0.7\,R_\odot$ the temperature drops to 1 MK allowing protons to capture electrons into a bound orbit. The existence of electrons in atomic orbit results in a dramatic increase in opacity of the plasma (Turck-Chièze & Couvidat, 2011) and hence the temperature gradient increases. The increased temperature gradient required to sustain the energy flow may lead to the onset of a convective instability beyond $0.7\,R_\odot$ toward the solar surface. This instability will occur if the temperature gradient in the star is steeper than the adiabatic temperature gradient

$$\left|\frac{dT}{dr}\right|_{star} > \left|\frac{dT}{dr}\right|_{adiabatic} \tag{1.6}$$

This is known as the Schwarzchild criterion, and it is fulfilled from $0.7 - 1\,R_\odot$ $-$a region known as the convection zone. The temperature and density drop as height increases and finally reaches T$\sim$6000 K and mass densities of $\rho \sim 1 \times 10^{-5}\,\mathrm{kg\,m^{-3}}$. Although no complete theoretical treatment of convection exists, mixing length theory and hydrodynamical modeling are used to determine how convection occurs in the solar interior. Convection ceases at $1\,R_\odot$, where the environment makes a sudden transition to convectively stability. At this point the opacity drops and energy is released in the form of radiation, demarcating the start of the solar surface, known as the photosphere.

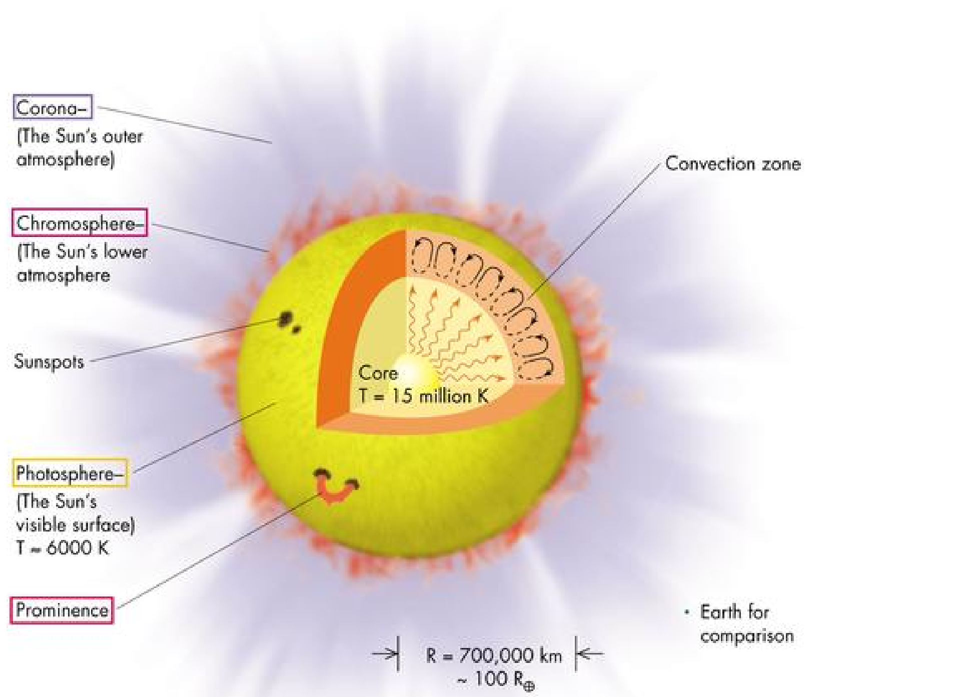

Figure 1.1: The internal structure of the Sun, including the core, radiative zone, and convective zone. Also shown is the structure of the its atmosphere, including the photosphere, chromosphere, and corona. The layers of the solar atmosphere are usually demarcated by temperature changes as height above the solar surface increases. The temperature ranges from ~6000 K in the photosphere to above 1 MK in the corona.

Much of what we know about the depth, temperature, and density of the convection zones come from a fine-tuning of the standard solar model, such that the model reproduces observations from neutrino and helioseismology experiments. This field helioseismology makes use of the fact the Sun acts as a resonator for acoustic waves which manifest as detectable oscillations in the doppler shift of photospheric Fraunhofer lines. These acoustic waves are referred to as pressure or p-modes, and a variety of wavelengths exist, generally with a period of approximately 5 minutes (Turck-Chièze & Couvidat, 2011).

The shorter wavelengths in the mode propagate into the solar convection zone and experience a total internal reflection at a shallow depth, while longer

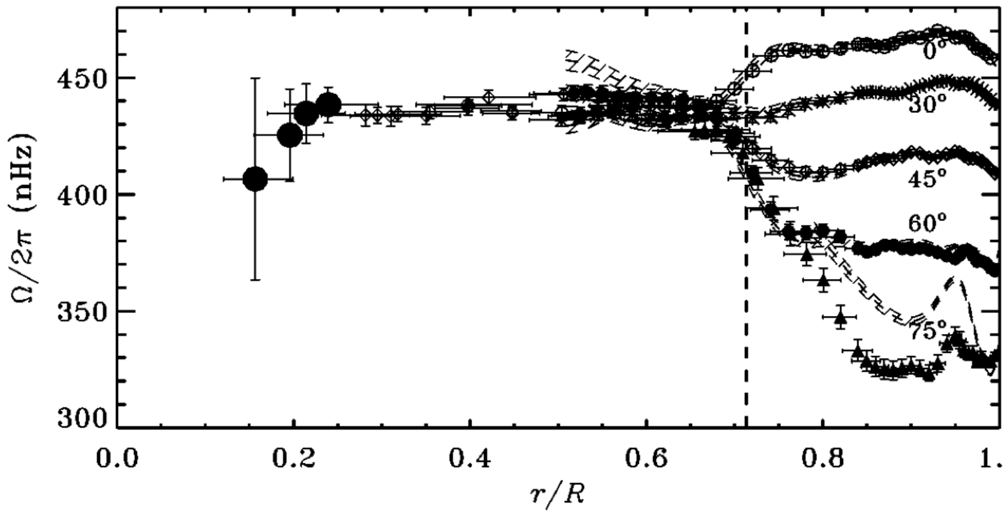

Figure 1.2: Helioseismological determination of interior rotation rate in nanoHertz (nHz) as a function solar radius, starting from solar centre ($r = 0.0$) to surface ($r = 1.0$). The separate symbols show different latitudes, from 0° to 75°. The data show that the interior rotates differentially down to $\sim 0.7\, R_{\odot}$. The dashed line demarcates the boundary between solid body rotation and differential rotation (Thompson *et al.*, 2003).

wavelengths can penetrate into much deeper layers. Hence depending on the period observed, the oscillations provide a probe of the dynamical properties at a particular level. Helioseismology has revealed that differential rotation that is observed at the surface continues down into the convection zone, however the deeper radiative zone rotates as a solid body Figure 1.2. In going from the convection zone to the radiative zone there is a sudden dramatic transition in the rotational dynamics of the solar interior. This sudden changes occurs in a region sandwiched in between radiative and convective, known as the tachocline. The study of this layer is extremely active as it is believed to play an important role in the generation and evolution of the solar magnetic field (Thompson *et al.*, 2003).

1.1.2 Solar Magnetic Field and Dynamo

The solar magnetic field is the ultimately source of all energetic activity ocurring in the atmosphere. At solar activity minimum the solar magnetic field has a poloidal dipolar structure, with the polar axes generally being coincident with the rotational axes. However as the the activity cycle progresses towards a maximum, the field gains a strong toroidal component, making it far more dynamic and complex. This complex toroidal component manifests at the surface as sunspots, hence the number of sunspots on disk has been used as a proxy for the activity cycle for over 100 years, often showing an approximate 11 year periodicity (Figure 1.3, bottom panel). At the beginning of the cycle sunspots tend to appear on disk with a latitudinal distribution of $\pm 30°$ of the equator. As the cycle progresses, sunspots appear at lower and lower latitude (known as Spörer's law), until they eventually disappear at the end of a cycle. Sunspot latitude with respect to time is shown in Figure 1.3, top panel, and is known as the butterfly diagram.

Sunspots in there simplest case emerge as a dipole structure, with the leading spot being closer to the equator, such that the dipole is titled relative to the solar equator (Joy's law). In a given hemisphere, the leading sunspot and trailing spot have opposite polarities, with the polarities reversed in the other hemisphere (Hayle's law). The trailing polarity can often be more fragmented and dispersed that the leading polarity. Despite sunspots generally having a dipolar structure, spot groups can be far more complex, having a multipolar structure.

Over the course of a solar cycle, the sun changes polarity (at the time of sunspot maximum). For example, an overall dipolar configuration of North-South will become South-North, another cycle will bring it back to N-S once more. While the activity cycle usually last 11 years, one full magnetic cycle has

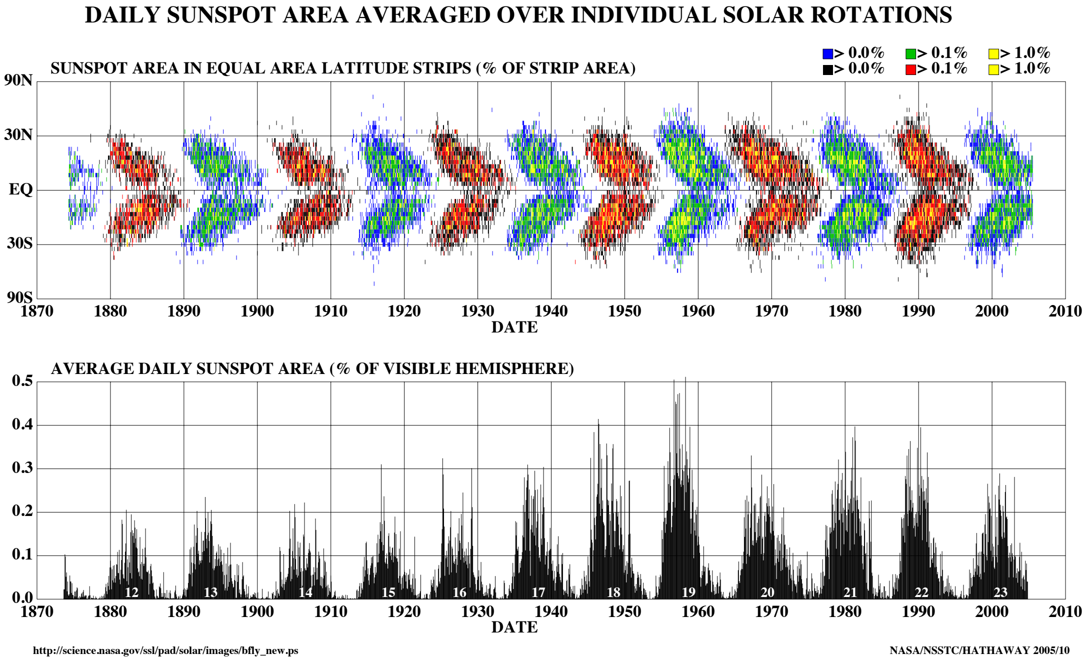

Figure 1.3: Top: The latitude of sunspots as a function of time. During the rise phase of each cycle the sunspots have a latitudinal distribution of ±30° from the equator. As the solar cycle progresses, sunspots emergence takes place at an increasingly lower latitude. Bottom: Sunspot area as a function of time. The approximate 11 year periodicity is clearly shown.

a period of 22 years. The complex behavior of the solar magnetic field over an 11 year activity cycle, during which the dipole reverses sign, is generally explained by solar dynamo theory. The theory employs magnetohydrodynamic models are employed that involves large-scale flow patterns of the solar interior that act to both induct and diffuse the magnetic field such that it produces the familiar 11 year magnetic activity cycle (Charbonneau, 2010).

The generally accepted paradigm for tha activity cycle was first proposed by Babcock (1961). The mechanism involves differential rotation of the solar convection zone tends to drag the field from a poloidal position into a toroidal one (known as the Ω-effect), eventually winding the field into a a stressed state, see Figure 1.4. The main storage of this wound field is in the region below

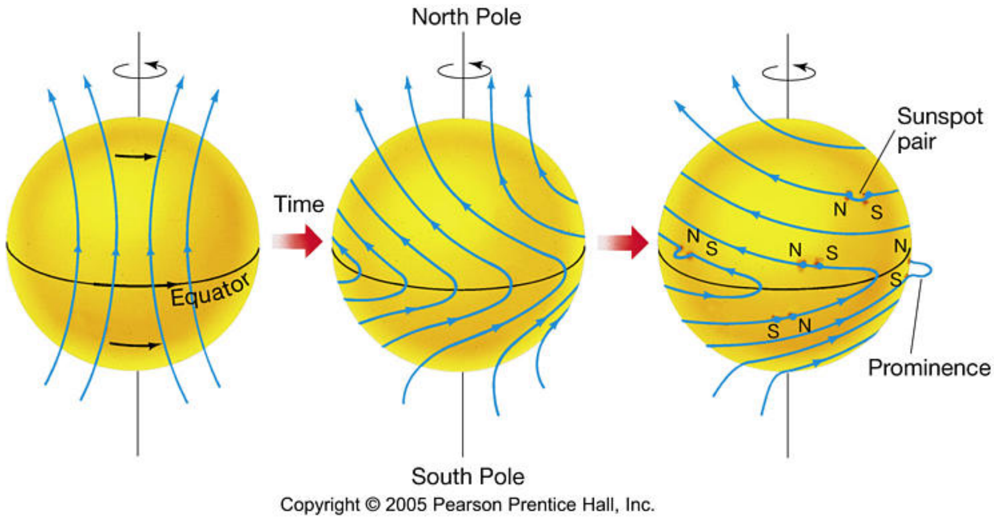

Figure 1.4: Differential rotation and flux freezing result in the poloidal dipolar magnetic field, generated by dynamo action, to be dragged around in a toroidal direction, an action known as the omega effect. Buoyancy of the field lines results in them rising and twisting, known as the alpha effect, eventually surfacing to become bipolar fields that extend far into the corona.

the convection zone known as the tachocline. This region has an 'overshoot' layer, in which descending convective flows are a trapped due the subadiabicity of the region (convectively stable). This stability allows field to be built up and stored into complex magnetic structures that may form a twisted 'flux-ropes' due to the continuous wrapping of the field during the Ω-effect. Due to the rope's excess magnetic pressure, it becomes convectively unstable and begins to rise and experience a Coriolis force that induces a tilt of the rope with respect to the equatorial plane (known as the α-effect and explanation of Joy's law). The field eventually surfaces creating sunspots in the photosphere and a complex magnetic structure in the solar atmosphere known as an active region (Fan, 2009).

1.1.3 Solar Atmosphere

The solar atmosphere begins above the visible surface of the sun, known as the photosphere. At this point, the Sun become optically thin to visible radiation and light escapes from this surface. Beyond this visible surface is the solar chromosphere, the corona, which eventually becomes the solar wind. Each of these layers is home to a complex array of phenomena, and each layer with it's accompanying attributes is described here.

1.1.3.1 Photosphere

As mentioned the photosphere begins where the atmosphere become optically thin. 'Visible light' in this instance is usually taken to mean light with a wavelength of 5000 Å, hence the emergent light from the photosphere is taken to come from the surface at which $\tau_{5000} = 2/3$. This is a consequence of the Eddington-Barbier approximation, and says that emergent flux F_ν from the photosphere is given by

$$F_\nu = \pi B_\nu(\tau = 2/3) \tag{1.7}$$

e.g., the emergent flux is given by π times blackbody intensity at an optical depth of 2/3, where blackbody intensity B_ν is given by Planck's law

$$B_\nu = \frac{2h\pi\nu^3}{c^2}\frac{1}{\exp(h\nu/k_BT) - 1} \tag{1.8}$$

where h is Planck's constant, ν is frequency, c is the speed of light, k_B is Boltzmann's constant, and T is temperature. Integrated over frequency this results in $F = \sigma T^4(\tau = 2/3)$, where the frequency integrated flux is proportional to the temperature at $\tau = 2/3$, hence the effective temperature of solar blackbody radiation is $T_{eff} = T(\tau = 2/3) = 5800\,\mathrm{K}$. Solar radiation at visible wavelengths is most closely characterised by a blackbody of temperature 5800 K, although the brightness temperature T_B the solar photosphere can deviate from this value, since not all frequencies emerge from the same optical depth.

The visible appearance of the photosphere reveals a small scale granular structure, with granules of typical size scale of 1000 km with a lifetime of 5-10 minutes. The granules typically show bright centers surrounded by darker intergranular lanes. Doppler measurements reveal that granule centres have a positive (upward) velocity of up to $\sim 1\,\mathrm{km\,s^{-1}}$, with intergranular lanes having a negative (downward) velocity. Such upward and downward flow reveals that granulation at the photosphere are the surface manifestation of convective activity in the deeper layers of the sun, although the size scales of granules are much smaller than the convective plumes believed to permeate the convection zone. As well as the conspicuous granulation at the photospheric surface there is also a much larger scale 'super-granulation' which has much the same mechanism as the granules e.g, upflows at granule centre and downflows at the edges in the granular network. The flow speeds are much slower with typical speeds of $0.1\,\mathrm{km\,s^{-1}}$. The have a much larger size of $10,000 - 30,000\,\mathrm{km}$ and longer lifetimes of several days. They have an important role in the build up and concentration of magnetic flux in the intergranular lanes. Apart from, granules and supergranules, the most conspicuous features of the photosphere are sunspots. As discussed in the previous section, these are the surface manifestation of concentrated magnetic flux that has penetrated from the solar convective zone into the solar atmosphere. The spots have a temperature of $\sim 4000\,\mathrm{K}$, which is cooler than the typical solar blackbody temperature of 5800 K. The spots have typical magnetic field strengths of on the order of kilo-Gauss, and have an important role to play in solar activity.

Although the the intensity of the Sun in the visible may be approximated closely by a blackbody continuum, there are also the presence of dark absorption or Fraunhofer lines in the spectrum. The most notable of which are the Hα and CaII H and K lines. The presence of these lines reveals that cooler part of the photosphere must overly the hotter base at $\tau_{5000} = 1$ (Phillips *et al.*, 2008). In fact, the variety of lines that are produced in the solar atmosphere (both emission and absorption) are used to determine the temperature and density stratification of the solar atmosphere. That has most notably been done in the models of (Fontenla *et al.*, 1988; Gabriel, 1976; Vernazza *et al.*, 1981), whereby a temperature and density profile of the solar atmosphere is used to calculate the emergent intensity, using radiative transfer theory. This temperature and density profile is adjusted until the the modeled emergent intensities match the observed ones. The results of this these models is shown in Figure 1.5. From this Figure we see that there is a temperature minimum at $\sim$500 km above the photosphere where the temperature drops to $\sim$4400 K. Beyond this point the temperature begins to rise again, eventually showing a rapid increase at $\sim$2000 km. The region between the temperature minimum up the height at which temperature begins to rise rapidly is known as the chromosphere[1].

1.1.3.2 Chromosphere

As predicted by the models of (Fontenla *et al.*, 1988; Gabriel, 1976; Vernazza *et al.*, 1981), at $\sim$500 km above the $\tau_{5000} = 1$ surface the temperature drops to a minimum of $\sim$4400 K. Beyond this minimum the temperature begins to rise again, demarcating the beginning of the chromosphere. This layer of the atmo-

[1]These boundaries can vary, depending on the phenomenon observed e.g., spicules are chromospheric phenomenon which can extend far beyond the upper boundary of $\sim$2000 km

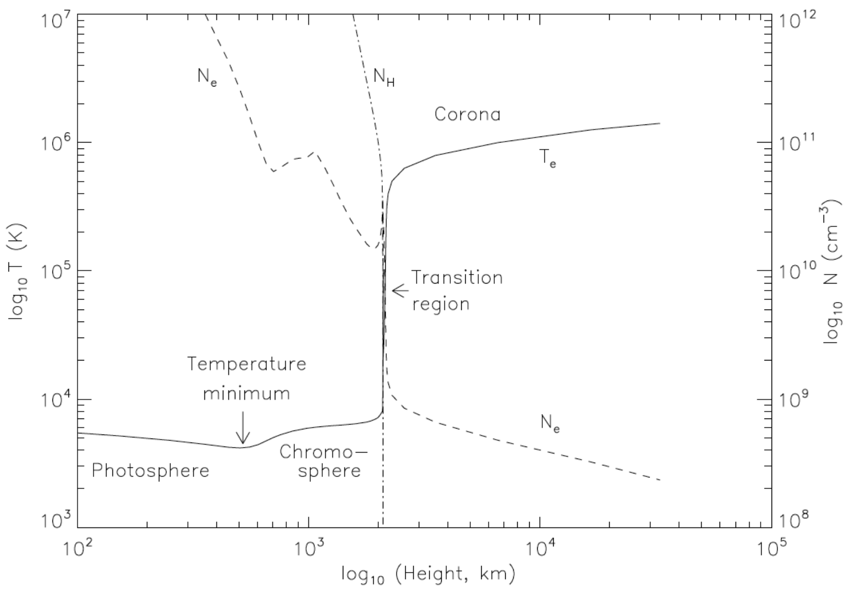

Figure 1.5: Temperature and density variation in the solar atmosphere constructed from the models of (Fontenla *et al.*, 1988; Gabriel, 1976; Vernazza *et al.*, 1981), adopted from (Phillips *et al.*, 2008).

sphere is generally accepted to extend to a height at which temperatures reach 20,000 K, however temperatures as high as $\sim 1 \times 10^5$ K are sometimes attributed to chromospheric heights, hence it is observable at ultraviolet (UV) wavelengths as well as visible.

Beyond the temperature minimum there is a broad temperature plateau between $\sim 1000 - 2000$ km, after which the temperature starts to increase dramatically. When the temperature reaches 20,000 K the extremely prominent Ly-α emission line is formed, with a wavelength of 191.5 nm, and this is accompanied by other prominent ultraviolet lines such as those of C IV, formed at temperatures of $\sim$110,000 K. Such high temperatures are generally considered to be outside the range of the chromosphere and are indicative of a thin layer of the atmosphere known as the transition region. This layer is on the order of a few hundred kilometers thick but has an extremely steep temperature gradient, carrying temperatures into the mega-Kelvin range. The region of the atmosphere with temperatures greater than 1×10^6 K is known as the solar corona.

1.1.3.3 Corona

The outermost layer of the solar atmosphere is known as the solar corona, beginning at ~2500 km above the photosphere. It has an electron number density of $10^9\,\mathrm{cm}^{-3}$ at its base in quiet regions, decreasing to $10^6\,\mathrm{cm}^{-3}$ at distance of $1\,R_\odot$ from the solar surface. The models of (Fontenla *et al.*, 1988; Gabriel, 1976; Vernazza *et al.*, 1981) reveal that beyond the transition region (~2500 km) the temperature in the corona reaches well over 1×10^6 K. Such high temperatures allow the formation of emission features that belong to highly ionized heavy elements, for example Fe IX, up to as high as Fe XXIV. The presence of these highly ionized species (and many others) show that the corona has temperatures in the $1 - 2$ MK range in quiet regions, active regions may exhibit temperatures in the range of $2 - 6$ MK, while coronal holes may be lower than 1 MK. The temperatures of a flaring active region can be even higher than this, reaching tens of mega-Kelvin. The high temperatures and presence of highly ionized species of heavy elements means the corona is an emitter in the ultraviolet and X-ray. When viewed at these wavelengths, the corona appears highly structured, showing concentrations of bright loops known as active regions (Fig. 1.6).

Ultraviolet wavelengths allow observations of the very low corona, perhaps to only a few scale heights. However, the most extensive observations of the corona are in the visible, generally known as the 'white-light' corona. The corona's white-light radiation is primarily due to scattering of photospheric light by particles and dust grains. The component which is due to Thomson scattering by free electrons is known as the *Kontinuierlich* or K-corona. The spectrum of this light is same

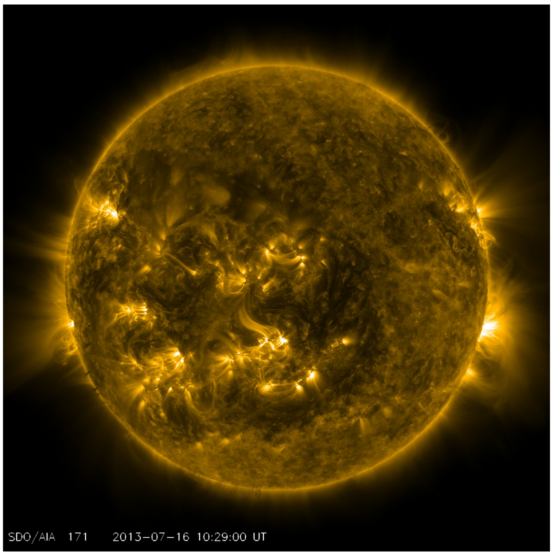

Figure 1.6: Atmospheric Imaging Assembly 171 Å image of the solar corona. Bright regions are strong concentrations of magnetic fields known as active regions (temperatures of $2-6$ MK). Areas outside these regions are known as quiet sun (temperatures $1-2$ MK).

as the photospheric continuum except for the absence of Fraunhofer lines. These lines are 'washed-out' of the spectrum due to thermal Doppler broadening of the high-velocity free electrons on the corona. The emission is optically thin, so the intensity is due to the number of scattering agents along the line of site. The emission is also highly polarized, depending on he line of site of the observer (we will return to this important aspect later). The K-corona dominates white-light emission from low atmosphere to $\sim 4R_{\odot}$. After this height, there is an increasing contribution from Rayleigh or Mie scattering from interplanetary dust grains, known as the the Fraunhofer F-corona. Since these dust grains move at a much slower velocity than the electrons, they do not wash out the Fraunhofer lines of the photospheric spectrum. The F-corona extend far beyond Earth and a can be viewed in the night sky as *Zodiacal light*.

Ultraviolet and white-light observations remain the primary method of imaging the low and extended corona, respectively. However, the corona is also a

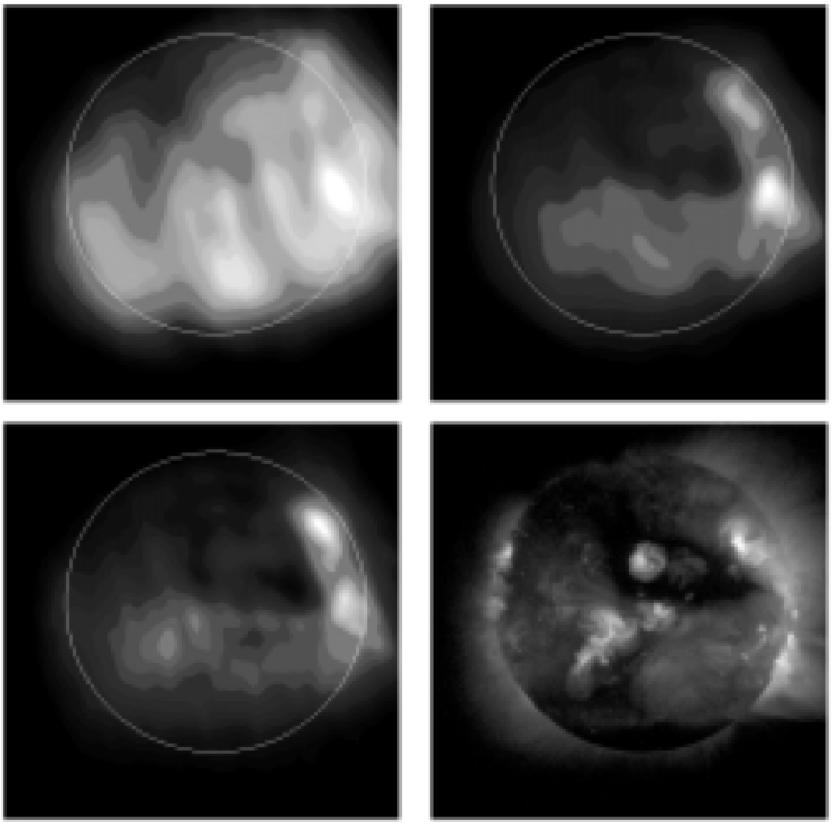

Figure 1.7: Low frequency observations of the solar atmosphere. Nan cay Radioheliograph (NRH) 164MHz (top left), 327 MHz (upper right), and 410 MHz bottom left. Yohkoh Soft X-ray Telescope (SXT) image for comparison. Note the coronal holes in the SXT image is also in the 164 MHz image of NRH. The active regions are also bright at 327 MHz and 410 MHz (Lantos, 1999)

strong emitter across the entire radio wavelength range, from microwave to kilometric wavelengths. Indeed, metric wavelengths provide a method of imaging the quiet and thermal corona in an optically thick regime beyond 1 $R_{\odot}$, an ability that does not exist in white-light and UV observations. These radio observations can reveal much of the same features as other wavelengths (albeit at lower spatial resolution) such as bright emission of active regions and also coronal holes (Fig. **??**).

The quiet corona at metric wavelengths is primarily an emitter of thermal Bremsstrahlung i.e., thermal electrons accelerating in the Coloumb electric fields of protons. The height at which metric radiation escapes from the corona depends on the Bremsstrahlung absorption process, known as free-free opacity and given by

$$\kappa_{ff} \sim \frac{n^2}{\nu^2 T^{3/2}} \tag{1.9}$$

where n is the electron number density, ν is the frequency of electromagnetic radiation, and T is the temperature. Qualitatively, for a given frequency the density must drop below a certain value for the radiation to become optically thin and escape the solar atmosphere. In the radio band, even the highest frequency (microwaves) do not escape until densities drop to chromospheric values. Hence a microwave image of the sun will provide a direct observation of light escaping from the chromosphere. Reducing the frequency further still to the 10^8Hz (metric wavelengths), the density must drop to coronal values before the free-free opacity is low enough for radiation to be optically thin. Hence, metric wavelength radiation escapes the solar atmosphere only in the outer corona. For example 150 MHz imaging of the solar atmosphere may image an optically thick atmosphere out to a height of $\sim 0.5\,R_\odot$. The existence of an optically thick atmosphere at these wavelengths allows a direct probing of coronal temperatures at these heights. Using the solution to the radiative transfer equation

$$T_B = T_0 e^{-\tau_\nu} + T_e(1 - e^{-\tau_\nu}) \tag{1.10}$$

where T_B is the observed brightness temperature, T_0 is the background source brightness temperature, and T_e is the electron temperature of a cloud of plasma between observer and source[1], we can separate the this equation into two regimes.

[1]Note that radio observations often use brightness and electron temperatures in place of specific intensity and the source function because radio observations are often calibrated via a load of known temperature

Firstly, in the optically thick regime $\tau_\nu >> 1$ equation 1.10 reduces to $T_B = T_e$, indicating that the brightness temperature is a direct measure of the electron temperature in solar atmospheric plasma. Secondly, in the optically thin regime $\tau_\nu << 1$, equation 1.10 reduces to

$$T_B = T_0(1 - \tau_\tau) + T_e\tau_\nu \tag{1.11}$$

Considering the case of no background source we see that for the optically thin regime $T_B = T_e\tau_\nu$ i.e., the brightness temperature is not a direct measure of the electron temperature, but is reduced by a factor of τ_ν. Note if the electrons are thermodynamic equilibrium then T_e is simply the temperature of the plasma T, given by the Maxwell-Boltzmann distribution, meaning a measure of brightness temperature allows a direct probing of the coronas thermal properties at this height. For example, a measure of brightness temperature at 100 MHz will given $T_b \sim 10^6$ K. However, beyond 1 GHz the corona becomes optically thin and brightness temperature then drops to $\sim 10^5$ K. It is also possible to observe non-thermal source, which is related to the average energy of the emitting particles $< E >= kT_{eff}$, where k is Boltzmann's constant. In such a case, the brightness temperatures may be in excess of 10^9 K

1.2 Coronal Mass Ejections

The solar corona is home to a variety of dynamic and highly energetic activity, the cause of which is the build-up and release of magnetic energy. Of all the activity taking place in the corona, the most spectacular manifestation of energy release is the coronal mass ejection (CME). A modern understanding of corona mass ejectionss tells us that they are large-scale eruptions of plasma and magnetic field that propagate from the low solar corona into interplanetary space. They have speeds in the range $10-2500\,\mathrm{km \cdot s^{-1}}$ (Gopalswamy & Thompson, 2000), masses of $10^{13}-10^{16}$ g, and kinetic energies of $10^{22}-10^{25}$ J (Vourlidas *et al.*, 2010), making them the most energetic explosive events in the solar system and a major cause of adverse space weather in the near-Earth environment. The following provides an observational overview and open questions concerning the general properties of CMEs, including their morphology, kinematics, and dynamics, as well as their ability to drive shocks, accelerate particles, and produce a variety of radio bursts.

1.2.1 A Brief History

The largest flare ever to have been recorded occurred on September 1st 1859, observed by the astronomer Richard Carrington (Carrington, 1859). Approximately 17 hours after Carrington recorded the event, a powerful geomagnetic storm began at Earth, producing brilliant aurora and damaging telegraph systems on both sides of the Atlantic ocean. The event aroused much speculation on a causal link between the phenomena Carrrington observed on the Sun and the magnetic activity recorded throughout the Earth (Balfour, 1861). It was not until 1919 that a theory was put forward to suggest plasma transients emitted from the Sun may impact the Earth and cause geomagnetic activity and the aurora Lindemann (1919), a process later elaborated upon by Chapman & Ferraro (1930). Up until 1940s, the only evidence confirming the the plasma transient hypothesis was the correlation between solar and geomagnetic activity. However, following the development of radio receiver technology during World War Two, much interest was given to solar radio bursts and their indication that disturbances travel away from the Sun at speeds of up to $500\,\mathrm{km\,s^{-1}}$(Wild *et al.*, 1959). Further evidence came from the fields of cosmic rays studies, when it was suggested the ground level detections of particles at Earth such as those reported by (Forbush, 1946) may be related to a acceleration of particles by a shock moving through the solar atmosphere (Wild *et al.*, 1963). Eventually this activity was summarised by Gold (1962), who hypothesised the expulsion of magnetized plasma from the solar atmosphere and the driving of a shock by this expulsion tha accelerates particles into interplanetary space.

Gold's paper marked over 100 years of indirect evidence for the expulsion of plasma transients from the surface of the Sun toward Earth. However, it was not until December 14th, 1971 (112 years after the Carrington event) that the first direct images of one of these plasma expulsions was made with the coronagraph on board the 7th Orbiting Solar Observatory (OSO-7) satellite (Tousey, 1973). This marked the beginning of white-light CME studies as we know them today, and it was followed by a number of other instruments, including Skylab (MacQueen *et al.*, 1980), P78-1 (Sheeley *et al.*, 1980), and the Solar Maximum Mission (SMM) (Hundhausen, 1999), which provided corongraph observations up until 1989. The modern era of CME observations began 1995 with the launch of the Solar and Heliospheric Observatory (*SOHO*; Domingo *et al.*, 1995) and it more sophisticated suite of instruments, including the Large Angle Spectrometric Coronagraphs (LASCO). In 2006 LASCO was joined by the COR coronagraphs onboard the Solar Terrestrial Relations Observatory (*STEREO*; Kaiser *et al.*, 2008) and together they provide observations of of CMEs from the low solar atmosphere into interplanetary distances. The past 40 years of coronagraph operations in space have yielded observations of tens of thousands of CMEs, allowing a direct determination of their physical properties and a confirmation of what was first postulated by Carrington and others over 150 years ago.

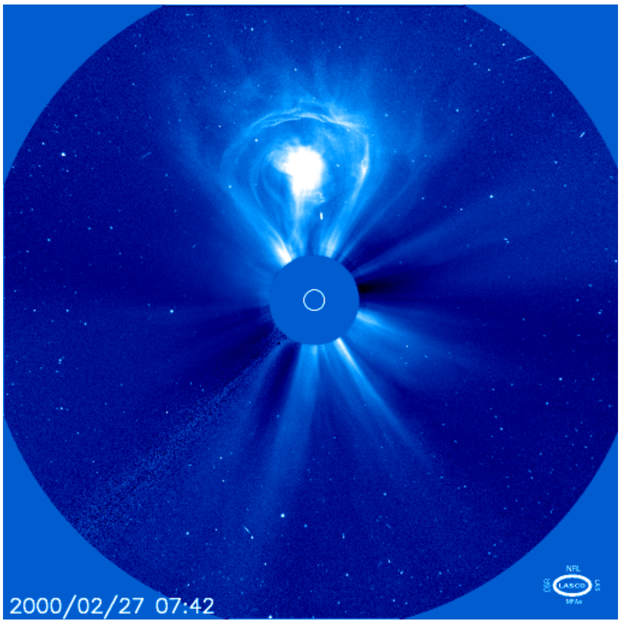

Figure 1.8: Large Angle Spectrometric Coronagraph (LASCO) C3 coronagraph image of a 'typical' CME, showing a bright front surrounding a dark cavity, with a bright core at the centre.

1.2.2 Morphology and Kinematics

CMEs are most often observed using a coronagraph, an instrument that creates an artifical eclipse of the bright solar disk so the much fainter corona can be images. Figure 1.8 shows the typical appearance of a CME in white light coronagraph images, having a three-part structure of bright front, followed by a darker cavity, and a bright core (Illing & Hundhausen, 1985). Although this CME is regarded as 'typical' in appearance, many CMEs do not have all of these features and some appear to have more complex morphological structures (Pick *et al.*, 2006), with only around 30% of all CMEs exhibiting the three part structure (Webb & Hundhausen, 1987). The varied nature of their appearance and morphology can usually be attributed to projection effects (Burkepile *et al.*, 2004) i.e., the CME is a 3-D object projected onto a 2-D image, hence its appearance depends on its orientation in the corona. With this in mind, a 'plane-of-sky' or limb CME (one that propagates a right angles to the observer-sun lines, erupting from the limb), offer the best measure of their properties i.e., the measured widths, appearance, speeds etc. do not suffer projection effects. Limb CMEs have a typical angular extent of approximately 50° (Burkepile *et al.*, 2004), and any CME that has width much greater than this ($> 120°$) is generally regarded as a 'partial halo' CME (Yashiro *et al.*, 2004). Halos or partial halos are CMEs that propagate toward the observer and hence appear to have a very wide angular extent (full halos can appear to have a 360° width), due to projection effects. However, statistics to characterize a typical CME size often only consider large 'classical' CMEs i.e., those ejection that have that generally appear typical are included, but the much smaller and very narrow ejections (widths $< 15°$) are excluded. The exclusion of small ejections means that typical CME size is normally distributed about $40 - 50°$. However, some studies account for these small ejections and simply consider any mass ejection, no matter how small, as a CME (Robbrecht *et al.*, 2009). Inclusion of the very small ejections has found the possibility of scale invariance in CME size, with the distribution being described by a power law. Robbrecht *et al.* (2009) has suggested that their is no 'typical' CME size.

The majority of CME observations rely on a 2-D projection onto the plane of sky, thereby disguising their true three-dimensional shape an geometry. Despite the majority of CME studies being constrained to 2-D measurements, there have been various studies whereby the full 3D extent of the CME bubble has been reconstructed. (Moran & Davila, 2004) used polarimetry measurements from the LASCO coronagraphs to reconstruct the three dimensional extent of the CME using Thomson scattering theory (the degree of polarization of white-light depends on the location of the scattering agent in 3-D space). When the STEREO spacecraft was launched in 2006 a number of stereoscopy techniques were developed that use geometric localization, whereby the CME is constrained to be within a polygon constructed from lines of sight from the two STEREO spacecraft (Byrne *et al.*, 2010; de Koning *et al.*, 2009). Other techniques use a pre-assume 3D construct that is oriented so that a 2-D projection of construct matches the observed 2-D image of the CME. This technique is known as foward-modelling an usually employs a graduated cylindrical shell or 'croissant' model as the pre-assumed shape of the CME (Thernisien *et al.*, 2006). Finally, other techniques employ a number of the above techniques simultaneously or for comparison of which preforms best (Mierla *et al.*, 2009). Although each of these studies have derived much more accurate CME properties such as size, shape, and kinematics that do not suffer projection effects, this has only been performed for a handful of cases. Unfortunately the typical CME statistics must suffer the unavoidable uncertainties of 2-D coronagraph observations. Perhaps the most egregious errors brought about by lack of three dimensional CME measurements are CME mass calculations, subject of chapter 4 of this thesis.

Despite the projection effects, reasonable CME kinematic properties may be derived if the CME is located in the limb or the general direction of propagation is accounted for. A number of CME catalogues exist that have tracked analysed thousands of CMEs, most throughout the SOHO mission. Measured properties include, CME launch latitude, speed, acceleration, and, where possible, masses and energies. The latitudinal distribution of of CME launch latitudes depends on the solar cycle, with the majority of CMEs erupting close the equator at solar minimum, and generally at all latitudes occurring during solar maximum (Yashiro *et al.*, 2004).

The amount of CMEs observed during the SOHO era (which continues today) has allowed many statistical studies of CME speeds and accelerations. CME speeds can range from 20 to 2500 $\mathrm{km\,s^{-1}}$ (Gopalswamy & Thompson, 2000), however average CME speed tends to be on the order of 480 $\mathrm{km\,s^{-1}}$ (Webb & Howard, 2012; Yurchyshyn *et al.*, 2005)[1]. The yearly average of CME speeds tends to change with the solar cycle, with an average of 280 $\mathrm{km\,s^{-1}}$ at solar minimum (1996), followed by a year on year increase in speed until an average of 520 $\mathrm{km\,s^{-1}}$ is reached even after solar maximum (2002) i.e., for solar cycle 23 the CME speed continued to rise even during the declining phase of the solar activity cycle (Yashiro *et al.*, 2004). There has been some debate surrounding the possibility of a bimodal distribution of CME speeds, generally considered a distinction between fast and slow CMEs. Slow CMEs with a speed of $400 - 600\,\mathrm{km\,s^{-1}}$ and gradual acceleration are usually associated with prominence lift-off, while fast CMEs with speeds in excess of 700 $\mathrm{km\,s^{-1}}$, no acceleration (or small deceleration), and are usually associated with flaring active regions (Gopalswamy & Thompson, 2000; Moon *et al.*, 2002; Sheeley *et al.*, 1999). Other statistical studies have suggested that there is no such distinction between the speeds of filament-associated and flare-associated CMEs (Vršnak *et al.*, 2005; Yurchyshyn *et al.*, 2005), with all CME having a more continuous distribution in speeds rather than a bimodal one.

This more continuous distribution is also reflected in statistical studies of CME acceleration magnitudes and timescales in the inner corona. Although typical CME accelerations in the later phases of propagation tend to be centered around zero with a narrow variation of $\pm 30\,\mathrm{m\,s^{-2}}$, CME accelerations in the very early phases of eruption can be considerably larger. Gallagher *et al.* (2003) found used TRACE and LASCO data to study the development of CME kinematics from its very early impulsive phase with peak acceleration of 1500 $\mathrm{m\,s^{-2}}$ to a more gradual

[1]Statistical studies from the era of Solar Maximum Mission and Solwind have found similar average speeds (Burkepile *et al.*, 2004)

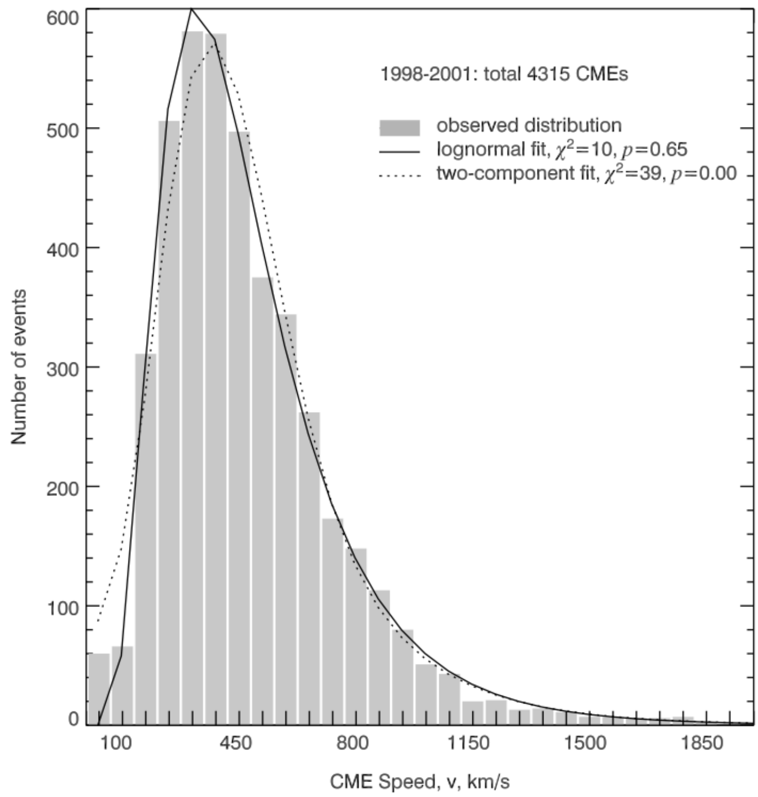

Figure 1.9: Distribution of speeds of 4315 CMEs observed by SOHO LASCO. The bin widths are $70\,\mathrm{km\,s^{-1}}$. The solid line represents a single lognormal fit to the observed data, while the dashed line is the sum of a Gaussian and a lognormal fit. (Yurchyshyn *et al.*, 2005)

phase of zero acceleration (Fig. 1.10).

A larger statistical study by (Zhang & Dere, 2006) using all three LASCO coronagraphs covering $1.1 - 30\,R_\odot$ found accelerations in the range of $2.8 - 4464\,\mathrm{m\,s^{-2}}$ with an average of $330\,\mathrm{m\,s^{-2}}$, with the acceleration timescales ranging $6 - 1200$ minutes (average of 180 minutes). An interesting outcome of this study was the discovery that the magnitude of acceleration appears to be inversely proportional to the duration of acceleration (Fig. 1.11), following the relationship $a = 1 \times 10^4 t^{-1}$.

Unfortunately the innermost coronagraph of LASCO (C1) failed in 1998, making early phase studies of CMEs difficult. Due to the failure of C1, the only ob-

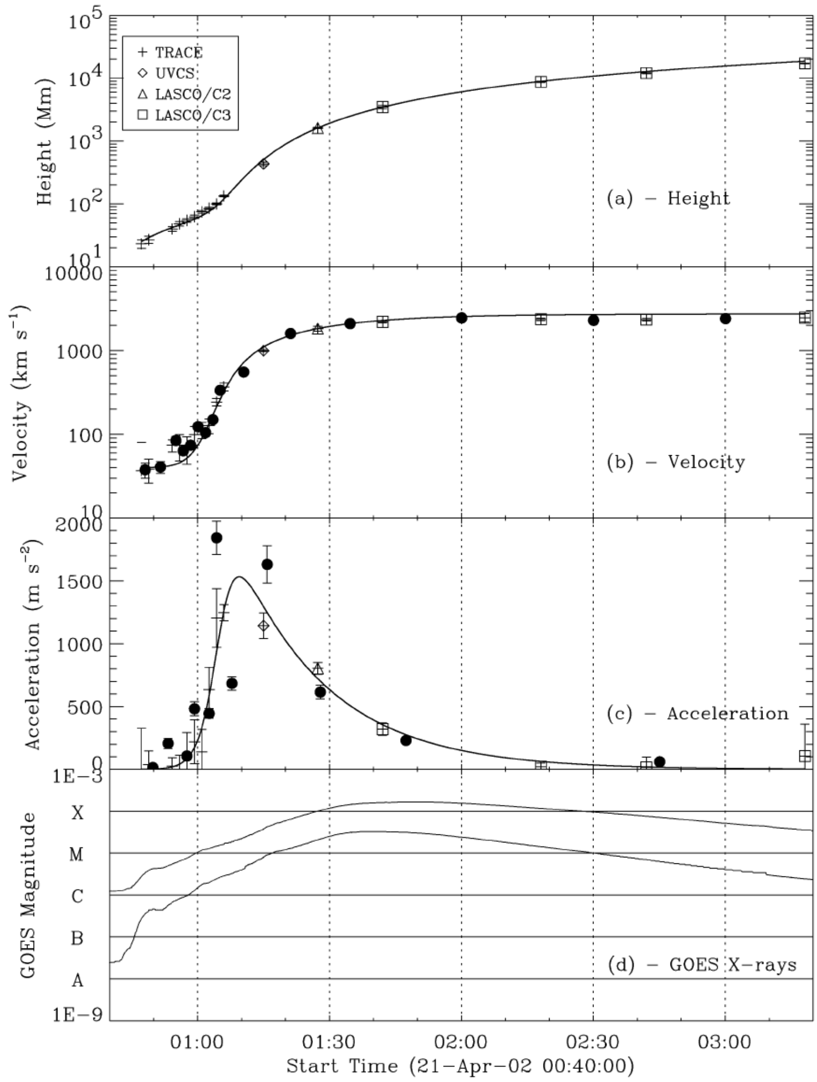

Figure 1.10: CME kinematics derived from TRACE, UVCS and the SOHO LASCO coronagraphs. The height time data is used to derive velocity and acceleration. The CME shows a peak in acceleration early in its propagation, this peak is coincident with the flare impulsive phase (indicated by the GOES) light curves in the bottom plot Gallagher *et al.* (2003)

servational method to determine the early phase eruption kinematics is in EUV imaging Larger statistical studies also show similar results of initial impulsive phase accelerations of $\sim 10 - 4000\,\mathrm{m\,s^{-2}}$, followed by a residual phase of near zero acceleration (Temmer *et al.*, 2010; Vršnak *et al.*, 2007). A large acceleration during the impulsive phase followed by a smaller (or zero) acceleration is recog-

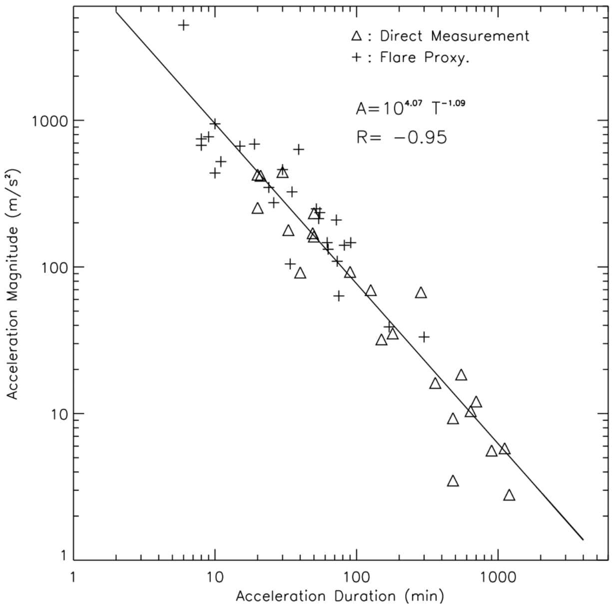

Figure 1.11: Acceleration of CMEs vs the duration of the acceleration. The data show an inverse proportionality i.e., shorter acceleration durations leads to larger magnitudes of acceleration (Zhang & Dere, 2006)

nized as being part of three distinct phases of eruption that closely tie the CME process to the flaring process, Fig. 1.12. Zhang *et al.* (2001, 2004) reported that CMEs show a very slow rise phase of coronal loops with a speed of $10-100\,\mathrm{km\,s^{-1}}$ over tens of minutes. This is followed by a phase of rapid acceleration which is accompanied by a simultaneous rise in soft x-ray (SXR) emission, as seen in a GOES light curve. After the flare and during the decline of SXRs the CME shows a near constant velocity with very little acceleration. The simultaneous rise of SXR emission at the time of maximum CME acceleration is taken to be an effect of the CME and the flare both being manifestations of the same reconnection process.

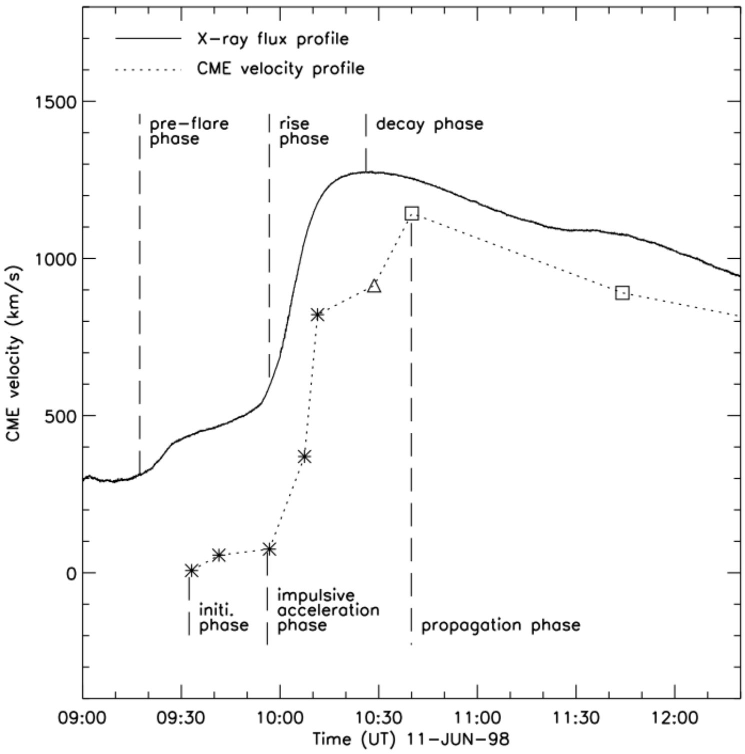

Figure 1.12: Correspondence between CME velocity profile and soft x-ray light curve from GOES. The two profiles follow each other closely showing that CME acceleration occurs during the flare rise phase. this is taken to be an effect of the CME and the flare both being manifestations of the same reconnection process Zhang *et al.* (2001).

1.2.3 Masses and Dynamics

As mentioned above, many properties of CMEs derived from two-dimensional coronagraph images suffer large uncertainties due to lack of knowledge about the true three-dimensional shape of the object. Despite this, much work has been done on CME kinematics and the general velocity and acceleration evolution is well known known. However, much less work has been done on the observational properties of CME dynamics e.g., calculating their mass, mechanical energies and forces.

Some of the first measurement of CME mass using scattering theory were carried out by Munro *et al.* (1979) and Poland *et al.* (1981) using space-based white light coronagraphs on board *SkyLab* and U.S. military satellite *P78-1*. Both the early studies and later statistical investigations determined that the majority of CMEs have masses in the range of 10^{13}–10^{16} g, (Vourlidas *et al.*, 2002, 2010). However, due to only a single viewpoint of observation, the longitudinal angle at which the CME propagates outwards was largely unknown in these studies and it is generally assumed that the CME propagates perpendicular to the observers line-of-sight (LOS). There is also the added assumption that all CME mass lies in the two-dimensional plane-of-sky (POS). Such assumptions can lead to a mass underestimation of up to 50% or more (Vourlidas *et al.*, 2000). More recent studies have employed the two viewpoint capabilities of the *STEREO* mission to determine the mass of numerous CMEs with much less uncertainty (Colaninno & Vourlidas, 2009). While the majority of mass estimates have come from white-light observations of CMEs, other wavelengths offer an independent measure of CME mass estimates, usually via a different technique which pertains to the wavelength. The eruption of a CME as seen by EUV imaging of the corona often shows a region of diminished intensity around the active region from which the the eruption took place. This is known as an EUV dimming, and is indicative of a mass evacuation i.e., the CME carries mass away when it erupts leaving behind a deficiency in emitting material. Aschwanden *et al.* (2009) calculated the mass from rom EUV dimming m_{EUV} and compared it to the mass measured in white-light m_{wl} and found a close match of $m_{euvi}/m_{wl} = 1.1 - 1.3$.

Perhaps the only measurement of CME mass via direct low frequency raio imaging was performed by Gopalswamy & Kundu (1992). an event observed on 6 February 1986 by Clarke Lake multifrequency radioheliograph showed an erupting structure at 73 MHz. On the assumption that the emission mechanism was thermal bremsstrahlung in an optically thin environment, an estimate of the emitting mass was calculated and shown to be 2.7×10^{15} g, similar to what is generally reported in white-light studies. Despite the interesting techniques afforded by EUV and radio observations, they are still not as popular as the white-light measurements of mass.

Given the relative ease with which CME positions and velocities may be determine, there are a small number of studies which combine these kinematic properties with the mass estimates in an effort to derive CME mechanical energy budgets. The first study to address the issue in the SOHO era attempted to quantified the magnitude of the kinetic and gravitational potential energy and compared this to a proxy for the magnetic energy from in-situ measurements of magnetic clouds (Vourlidas *et al.*, 2000). Out of the 11 CMEs that were studies, it was found that the CMEs mechanical energy increases at the expense of magnetic energy; The total energy of the CME (kinetic + potential + magnetic, usually on the order of 10^{30} erg) remains constant, indicating that there is no external driver of the CME between $3 - 30\,R_{\odot}$. Hence, CMEs much achieve escape velocity to exit the Sun's gravitational potential well, which they do so between $8 - 10\,R_{\odot}$. For slow to average speed events, the potential energy dominates the kinetic energy by an order of magnitude, the opposite is found for faster events.

A much larger statistical estimate of CME mechanical energy distribution was performed by (Vourlidas *et al.*, 2010) for 7668 CMEs observed by LASCO from 1996 January 22 to 2009 July 31.This is the most comprehensive CME mechanical energy statistics study to date and shows that both kinetic energy and total mechanical energy are are normally distributed about 2.3×10^{29} erg and 9.0×10^{29} erg, again showing that potential energy (mechanical - kinetic) is dominant over kinetic energy on avarege.

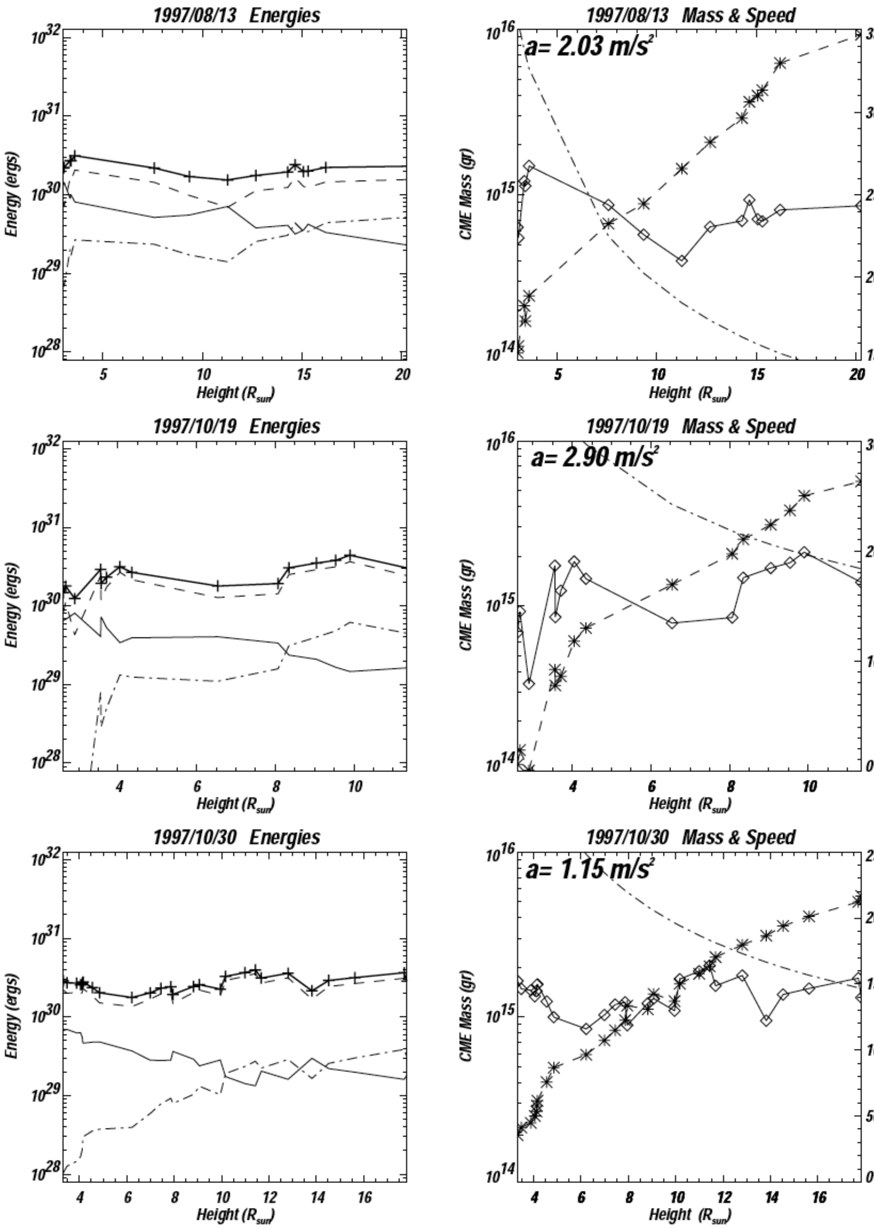

FIG. 4.—Same as Fig. 3

Figure 1.13: Coronal mass ejection energies and masses as a function of height for three different events. Left coulumn shows the CME kinetic (solid), potential (dashed), magnetic (dot-dashed), and total energy as a function height. In each of the plots, kinetic an potential energy increases at the expense of decreasing magnetic energy. The total energy remains quite constant, showing that there is no external driver of the system. Right column, CME mass (solid), center of mass speed (dashed), and escape velocity (dot-dash) as a function of height (Vourlidas *et al.*, 2000)

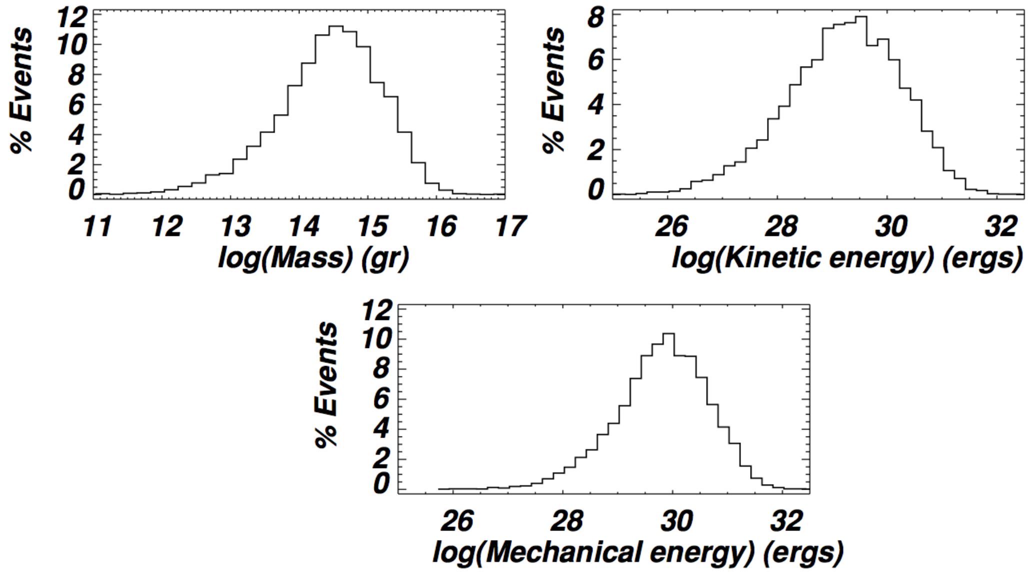

Figure 1.14: Distribution of CME masses, kinetic and total mechanical energies for 7668 CMEs observed by the LASCO coronagraphs between 1996 January 22 to 2009 July 31. The peak in kinetic energy is 2.3×10^{29} erg, while total mechanical energy is 9.0×10^{29} erg (Vourlidas *et al.*, 2010)

(Subramanian & Vourlidas, 2007) investigated the energetic properties of 39 CMEs in an effort to determine of CMEs in the outer corona ($2-20\,R_\odot$) are driven by momentum coupling to the solar wind or if internal magnetic energy is a viable source of driving power. They found that in 69% of the cases the mechanical energy of the CME increased linearly with time, and effect that suggests CMEs have driven by the release of some form of energy. The estimated total power delivered to the CME to increase its mechanical energy was $1.6\,\mathrm{erg\,hr^{-1}}$, which is far below the upper limit to the total power dissipated by the magnetic field in the CME ($14.4\,\mathrm{erg\,hr^{-1}}$). This is taken to be a suggestion that the CMEs magnetic field is the ultimate source of energy that drives its propagation, even out to large heliocentric distances distances. However the magnetic field estimates in this study are tenuous at best, and any magnetic power estimated derived from them should be treated with caution. Lewis & Simnett (2002) found that the solar wind may be a significant contributor to CME driving power, accounting for some proportion of an average $2.2 \times 10^6\,\mathrm{W\,kg^{-1}}$ required to drive the CME, however the authors do not mention quantitatively the possible driving power of the wind, merely calling the wind an 'infinite energy reservoir'. Hence it is difficult to affirm the possibility of their assertions.

Perhaps one of the only studies to make an observational estimate of the forces acting on CMEs is Vršnak (2006), although this study made use of kinematics to infer the dominant forces at play during CME propagation (acceleration is treated 'force-density' or Newtons per kilogram, a pseudo-measurement of force). The early phase eruption characteristics of a H-α spray ejection were analysed to derived the ejection's total acceleration a. This is recognized as being due to a combination of accelerations due to the Lorentz force a_L, gravity g, and aerodynamic drag a_d, such that $a = a_L - g + a_d$. Estimates of acceleration due to gravity can be made simply; expression for drag generally take into account the interaction of the CMe with the solar wind whereby drag is given by the difference between the ejecta and wind velocity $|v_{cme} - v_{sw}|$, the area of the ejecta exposed to drag by the wind A and a drag coefficient C_d which usually accounts for the shape of object. The expression can be either quadratic $a_d = -\gamma(v_{cme} - v_{sw})|v_{cme} - v_{sw}|$, where $\gamma = C_d A \rho_{sw}/M_{cme}$ (Cargill, 2004)[1]. v_{sw} may be given from a model of the solar wind, for example Sheeley *et al.* (1997). As for the γ term,Vršnak (2006) uses empirical scaling laws whereby $\gamma = 23R^{-2.2}\,\mathrm{km^{-1}}$, where R is the heliocentric distance of the ejecta. When gravity and drag are estimated in this way, a peak Lorentz acceleration is derived to be to be $1400\,\mathrm{m\,s^{-2}}$. Taking the particle density of the ejection to be $10^{16} - 10^{17}\,\mathrm{m^{-3}}$ the volume force can then be evaluated as $f_L = 10^{-8} - 10^{-7}\,\mathrm{N\,m^{-3}}$. This is one of the only studies (perhaps the only) in the literature that attempted to derive a size for the Lorentz force, albeit by using

[1]Solar wind drag on the CME is discussed further in Chapter 4

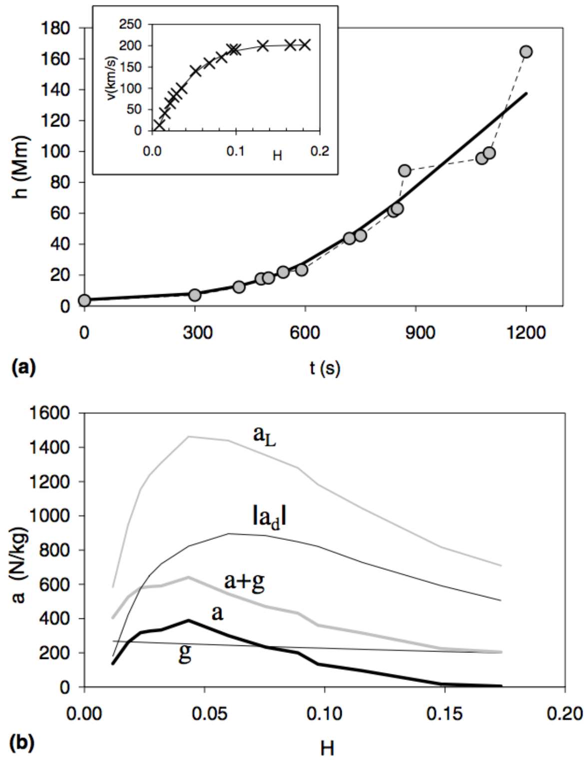

Figure 1.15: Top: the height-time velocity of a h-alpha spray, with velocity as a function of height inset. Bottom: the acceleration of the spray a as a function of height (derivative of inset in top panel), as well as the acceleration experienced from gravity a_g (also $a + a_g$), drag $|a_d|$, and acceleration due to the Lorentz force a_L (Vršnak, 2006)

an indirect proxy, and also by only looking at a H-α spray.

A statistical kinematical study was considered by (Bein *et al.*, 2011), where a number of parameters were compared, such as max acceleration experienced by the CME, duration of acceleration, and height of maximum acceleration. They find that, as in the Zhang & Dere (2006) (Fig. **??**), the acceleration experienced is inversely proportional to the duration of acceleration, and further, the acceleration experienced and the height of peak acceleration are inversely related. This is taken to be indicative of a compact source size having a more impulsive acceleration, an effect that is consistent with the Lorentz force. Again, the nature of forces acting on CMEs in this case is only inferred from kinematics studies, and not measured directly.

Finally, a word on the CME energy budget as compared to the total eruptive energy, including the flare and all by-products. Emslie *et al.* (2004) studied to eruptive energy budgets, taking into account (i) the CME, (ii) the flaring thermal plasma, (iii), the electrons responsible for hard X-rays, (iv) gamma-ray producing ions, and (v) solar energetic particles detected in-situ. Accumulating all of this into an energy budget for the two events found that the CME mechanical energy of $\sim 10^{32}$ erg is the dominant single component of energy consumption, with the flare thermal plasma, non-thermal electrons and ions, and in-situ detected particles, each consuming $\sim 10^{31}$ erg. A similar study was then carried out where the same analysis was applied to 38 eruptive events, which again found that the CME is the dominant consumer of total energy released (Emslie *et al.*, 2012)

1.3 Coronal Shocks

1.3.1 Type II Radio Bursts

Perhaps the first evidence of shocks transits in the corona came in the form of solar radio bursts, most notably a class known as type IIs. These bursts are characterized by bands of emission observed to drift slowly toward lower frequency over time in dynamic spectra. They have a typical drift rate of $\sim$-0.3 MHz s^{-1}, last on the order of 10 minutes, and are sometimes observed to have two emission bands with a 2:1 ratio. Although they are now recognized as one of the chief signatures of the transit of a coronal shock (Mann *et al.*, 1996; Nelson & Melrose, 1985), the driver of this shock has remained a topic of contention since their discovery in the first half of the 20th century.

The development of radio instrumentation during and after the second world

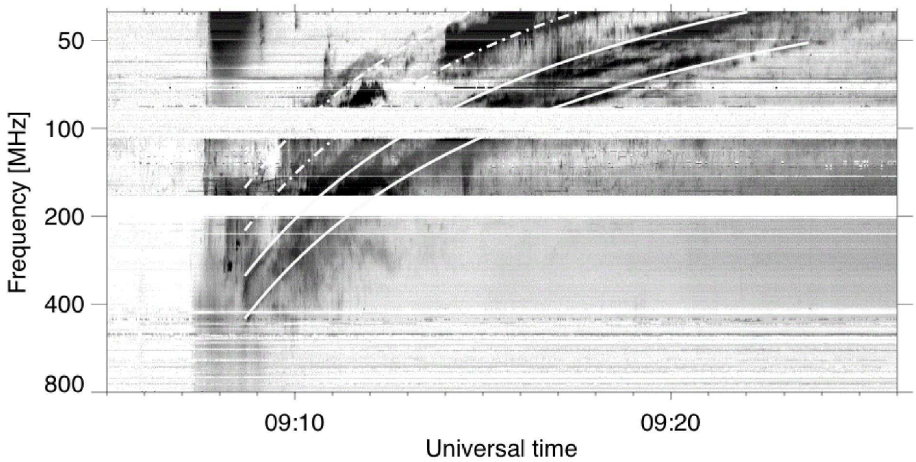

Figure 1.16: Type II radio burst observed at the Observatory Solar RadioAstronomy (OSRA) at Tremsdorf on 1997 November 3rd. Both the fundamental (dot-dash lines), and harmonic (solid lines) bands of emission are evident (Khan & Aurass, 2002).

war presented scientists with the opportunity of (sometimes inadvertently) observing radio activity on the sun. Whilst performing radar tests using British military equipment, (Hey, 1946) reported a very high intensity radio source (10^7 Jy) at 4-6 meters wavelength coming from the Sun. The relationship of these solar radio bursts with solar flaring activity was then reported by (Allen, 1947). In the same year, Payne-Scott *et al.* (1947) observed time series of single frequencies at 60 MHz, 100 MHz, 200 MHz and noted that a delay in onset time of the burst from high to low frequency may suggest *'the excitation of radiation at successive levels by an agency traveling at finite velocity'.* The analysis of single frequency intensity time series was then superseded by the employment radiospectrographs to produce dynamic spectra of solar radio bursts. This allowed the identification of slowly drifting type IIs that are well characterized by modern radio-spectral observations. The hypothesis for the origin of these bursts was the same as that of Payne-Scott *et al.* (1947) (a disturbance traveling into the corona at speeds of $10^2 - 10^3\,\mathrm{km\,s^{-1}}$), except Wild *et al.* (1954) correctly identified the emission to be generated at the frequency of plasma oscillation at the source height in the corona. (Uchida, 1960) and others eventually attributed these radio bursts to the activity that are they associated with today: type IIs are generated by mageto-hydrodynamic shocks transiting the corona. As the shocks propagate they excite radio emission at the local plasma frequency

$$f_p = \left(\frac{n_e e^2}{m_e \epsilon_0}\right)^{\frac{1}{2}} \tag{1.12}$$

Since the plasma frequency is only dependent on electron number density, as the shock propagates to larger heights in the corona the frequency of emission drops owing to the dropping density. Hence the shock excites emission at decreasing frequency over time. This effect is further described in section 2.X

At the time Uchida and others made the assertion that type IIs were generated by MHD shocks, CMEs were as yet an undiscovered phenomena. Hence, the hypothesis that the origin of the shock was a flare-induced blast wave was a common one. The close onset times of flare maximum and type II onset supported this idea (Maxwell & Thompson, 1962). The association of type II radio bursts with a Moreton wave (a disturbance propagating away from flare site, observe in H-alpha), and the modeling of the two phenomena as a flare-induced explosive MHD disturbance gave credence to the idea that type IIs were indeed signatures of blast waves (Uchida, 1974), a hypothesis later applied to type II observations (Kosugi, 1976).

Following the discovery CMEs, the idea that mass motions (and not blast-waves) could produce type IIs came under consideration. Part of this idea came from the confirmation of the detection of in-situ shocks ahead of interplanetary CMEs, then called 'plasma clouds' or 'magnetic clouds' (Hundhausen, 1972). Later, (Stewart *et al.*, 1974) showed good correspondence of the height-time kine-

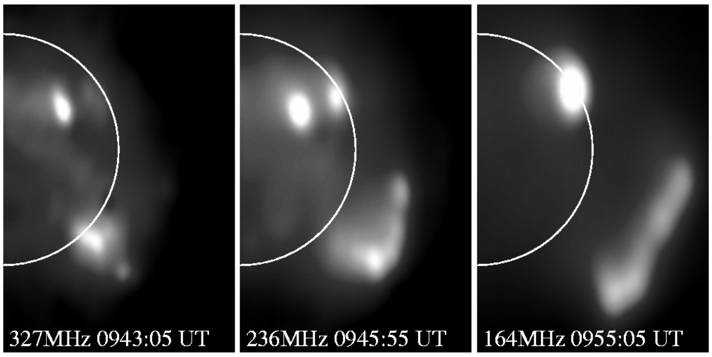

Figure 1.17: Propagating radio emission source imaged at 327, 236, 164 MHz using the Nancay Radioheliograph. The position of the emitting source is coincident with the CME leading edge (Maia *et al.*, 2000)

matics of a CME as observed by the coronagraph on OSO-7 and a type II burst source in images from the Culgoora Radioheliograph. This was taken as evidence that a piston-driven shock (CME-driven) was responsible for the type II. Following this was a statistical study that showed type II bursts to be highly associated with fast coronal mass ejections observed by the coronagraph on board Skylab (Gosling *et al.*, 1976). However, some doubts on the relationship were raised when (Robinson & Stewart, 1985) showed that while 42% of type IIs could be placed near the leading edge of a CME, some were located well behind the leading edge, this was considered to be evidence against the CME-driven shock idea. The CME hypothesis suffered another blow when it was shown that of an observed 116 metric type II bursts, 45 had a clear association with CMEs and soft x-ray flares, but up to 19 were observed to occur without any associated CME. (Claßen & Aurass, 2002) later showed that type II burst onset time have been shown to occur up to more than one hour before CME onset time in some cases. The contradicting accounts of the association of CMEs with type IIs fueled a debate on which was the more reasonable explanation: are CMEs or flares more likely to drive a shock that causes type IIs?

Direct evidence of radio bright shocks have at least shown that CMEs are capable of driving radio bright shocks (Maia *et al.*, 2000). In more recent times the debate continues, but the more sophisticated instrumentations, such as the Atmospheric Imaging Assembly, and multi-wavelength studies have offered a clearer picture. Bain *et al.* (2012) has shown clear evidence of an erupting plasmoid with a type II radio source that sits at its nose, very direct evidence for CME driven type II. Material motions imaged at soft X-rays also suggest a driven shock (Klein *et al.*, 1999). Kinematics of the shock derived from the type II drift and position often show a good correspondence with CME kinematics (Mancuso, 2011), however a statistical study by Reiner *et al.* (2001) showed there to be little correlation between CME and type II speeds. These has been described as a discrepancy attributed to the shock possibly being located on the CME flank, the kinematics match better under this assertion (Cho *et al.*, 2007, 2011; Mancuso & Raymond, 2004). Later UV spectroscopic evidence that a shock on the CME flank is indeed possible (Fig. 1.21).

Despite the fact that there is a large body of evidence for CME-driven shocks (at either the nose or flank) being associated with type IIs, there still remains convincing studies on the blast-wave possibility. The most recent direct evidence was given by (Magdalenić *et al.*, 2012), when they showed a compact flare with no sign of any eruption in h-alpha, EUV or white-light imaging. The debate rages on, and there is no consensus on either CME-driven shocks or flare-ignited blast waves (Vršnak & Cliver, 2008) [1].

Finally, a part of the controversy with determining the source of all radio bursts (not just type II) is to do with the the method by which radio burst

[1] It should be noted there is no ambiguity on the nature type IIs in the hecto-kilometric range. The accepted paradigm for these type IIs is a shock driven by a CME at interplanetary distances which may then be detected in situ as a shock. However, another controversy stemming from the flare-driven/CME-driven argument for type IIs is whether interplanetary type IIs and low coronal type IIs belong to the same driver (Cane & Erickson, 2005).

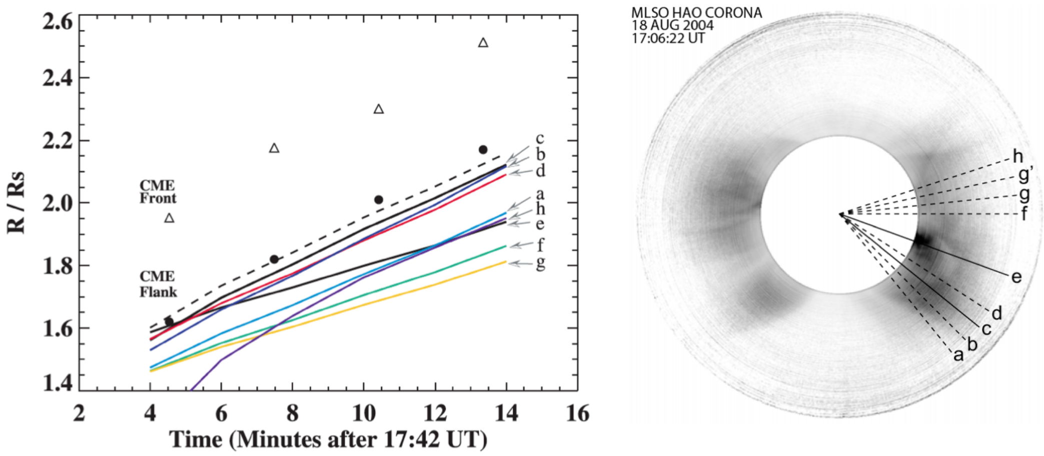

Figure 1.18: Comparison of height-time kinematics of a type II radio burst, observed using the Green Bank Solar Radio Burst Spectrometer (GBRBS), and CME as observed by the Mauna Loa coronagraph. Kinematics of CME at front an flank are shown, triangles and circles respectively. Lines $a-h$ show the kinematics of the radio burst derived from density measurements performed along the trajectories (right panel). The CME and type II show the best match at the CME flank along trajectory c. Figure adopted (Cho *et al.*, 2007)

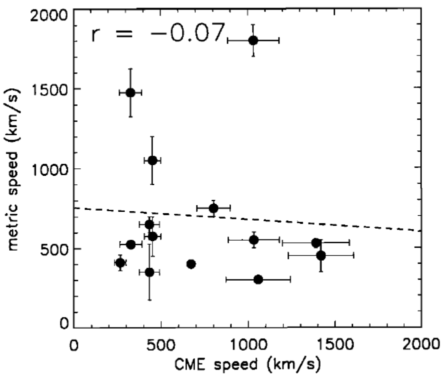

Figure 1.19: A statistical comparison of metric type II speeds and CME speed Reiner *et al.* (2001). The two show no obvious relationship, taken to be evidence that a CME may not be the driver of the metric type IIs i.e., a CME was not responsible for the low coronal shock that caused these type IIs

kinematics are deduced from density models of the solar atmosphere. The models ca often lead to questionable kinematics and heights of the radio sources. This is further discussed in Section 2.X.

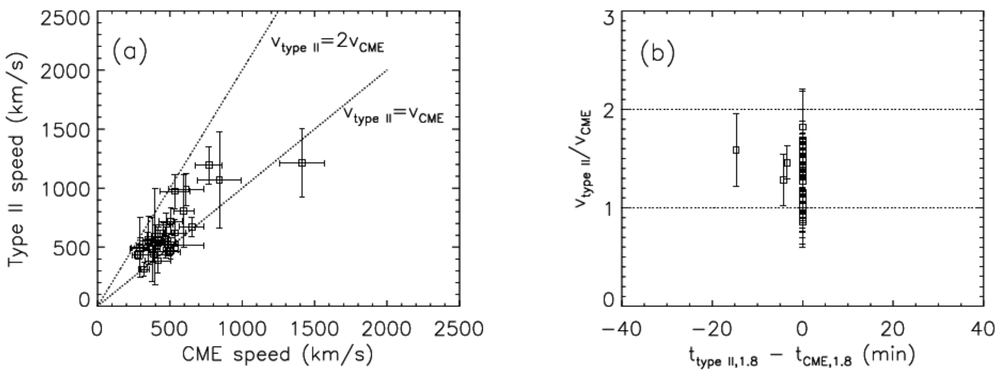

Figure 1.20: Comparison of type II and CME kinematics taking into account that the type II may be along the CME flank, showing a much better correlation (Mancuso & Raymond, 2004).

1.3.2 Herringbones and Type IIIs

As will be shown in Chapter 2, radio burst such as type IIs are believed to be the result of a plasma instability in the presence of high velocity electron beams. There is a subset of type II radio bursts which directly observe the electron beam nature of these radio bursts, known as 'herringbone' radio bursts (Cairns & Robinson, 1987; Cane & White, 1989). These are the signature of bursty electron acceleration occurring at a coronal shock front (Mann & Klassen, 2005). The 'herringbone' spike is an individual beam of electrons traveling away from the shock.

The fact they drift towards both low and high frequencies simultaneously means they are bi-directional in space e.g., drifting toward and away from the sun simultaneously. The 'bursty' or quasi-periodic nature of the herringbones occurs over timescales of seconds (Mann & Classen, 1995; Mann & Klassen, 2005) and they are believed to be a result of the shock drift acceleration (SDA) process (Miteva & Mann, 2007). The burstiness has been suggested to be due to inhomogeneity on the shock front, and may be signature of a so-called 'wavy' or 'rippled'

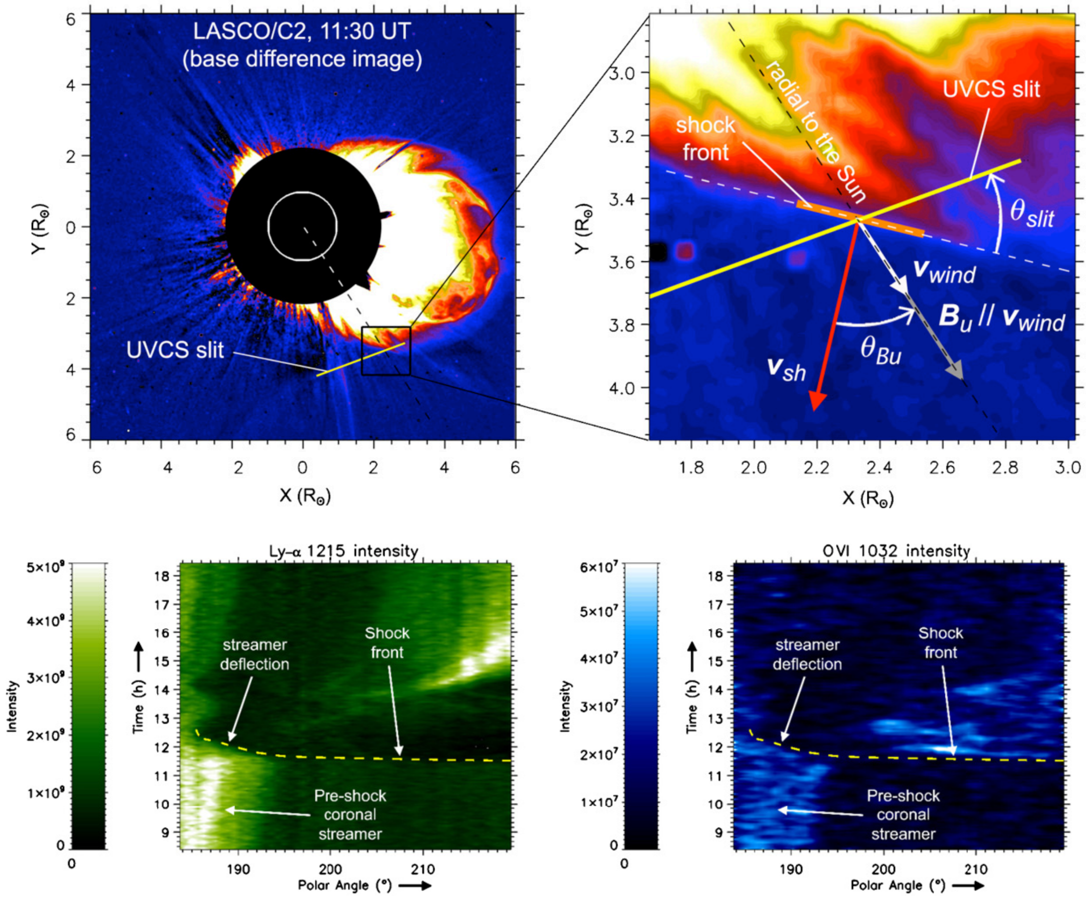

Figure 1.21: (Top) A LASCO C2 base-difference image of a CME on 2002 March 22, the yellow line marks the Ultraviolet Coronagraph Spectrometer (UVCS) slit located at CME flank. The event was associated with a type II radio burst. (Bottom) Space-time dependence of the H I Ly-α (left) and O VI 1032 Å (right) lines. The dashed yellow line shows the passage of the shock front. It results in a dimming of Ly-α, caused by a deficiency in the resonant scattering of the line. This is due the scattering agent experiencing a bulk flow velocity that doppler shifts its absorption profile with respect to the incoming radiation, hence reducing its ability to scatter Ly-α efficiently−known as the Doppler dimming effect. The oxygen line, on the other hand, is collisionally controlled and depends on the ambient free electron density. As the shock transits it heats the plasma, resulting in more further free electrons and more efficient excitation of the O VI 1032 Å, leading to brightening. The overall result is a dimming in the hydrogen line and a brightening of the oxygen line. This indication of bulk flow velocity as well as high levels of heating in the flow is evidence for a shock.

shock front (Guo & Giacalone, 2010; Vandas & Karlický, 2011; Zlobec *et al.*, 1993). This means they provide a measure of shock structure and and a timing of the particle acceleration process itself. The bursts are rare, so complete theory on their formation does not exist. they have been attributed to shocks propagating parallel to the surface (tangentially across radial field lines) whereby 'shock fronts propagate normal to the magnetic field and continuously eject bunches of fast electrons long the field' (verbatim from Wild (1964)), assertion was also illustrated in Stewart & Magun (1980). An alternative theory is one where the herringbones are produced in the termination shocks of super-Alfvénic outflow jets of a reconnection region (Aurass & Mann, 2004; Aurass *et al.*, 2002). Such a process could be the result of a reconnection region in a current sheet in the wake of a CME, as described by the standard solar flare model. Observational studies of herringbones are few and far between, as a result, the mechanism of their formations are inconclusive and remain to be confirmed.

Related to particle accelerations in the corona are type III radio bursts. These are fast drifting features in dynamic spectra ($\sim$20 MHz s^{-1}) and are the characteristic radio signature of electrons beams traveling on open magnetic field lines in the corona (Pick & Vilmer, 2008). Type IIIs are mainly associated with an acceleration process directly from the flaring active region e.g., acceleration directly out of the reconnection process. However, some type IIIs are thought to be associated with the in-situ detection of shock accelerated electrons. Indeed sometimes type II shock signatures are seen to occur with type IIIs, an indication of electron acceleration from the shock − these type IIIs are sometimes labelled 'shock-associated' or SA type IIIs (Bougeret *et al.*, 1998). In certain instances the particle acceleration as indicated by type III bursts has been related to shock feature seen the corona. This is usually in the context coronal bright front studies.

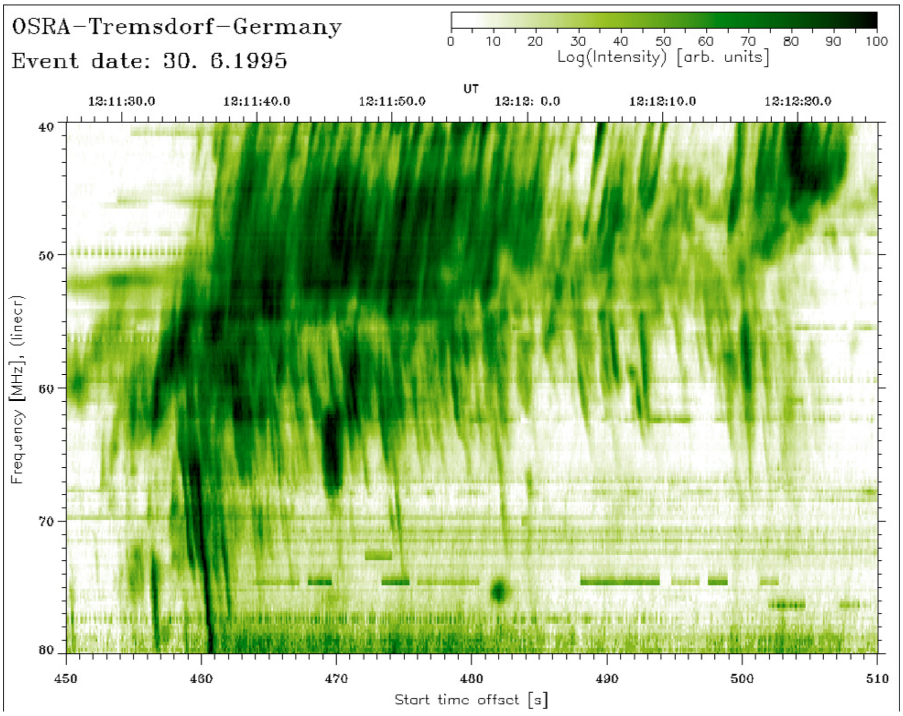

Figure 1.22: Fine structure observed in a type II radio burst known as 'Herringbones'. Each spike is an individual beam of electrons accelerated away from the coronal shock. The presence of herringbones drifting to both low and high frequencies is indicative of electron beams traveling toward and away from the Sun.

1.3.3 Coronal Bright Fronts

As mentioned, some of the explanations as to why a type II source may appear behind the CME front was the possibility of a shock driven by the CME flanks. As well as this, certain studies of type III radio burst associated with in-situ detection of solar energetic particles have been related to some shock driver low in the corona. One possible observational signature of shock activity in the low corona is a coronal bright front (CBF), also known as an 'EUV' wave.

CBFs were discovered in 1997-1998 (Moses *et al.*, 1997; Thompson *et al.*, 1998) by the EIT instrument on SOHO (hence they are sometimes called 'EIT' waves). Since the, CBFs have been considered a candidate for an wave-like phenomenon

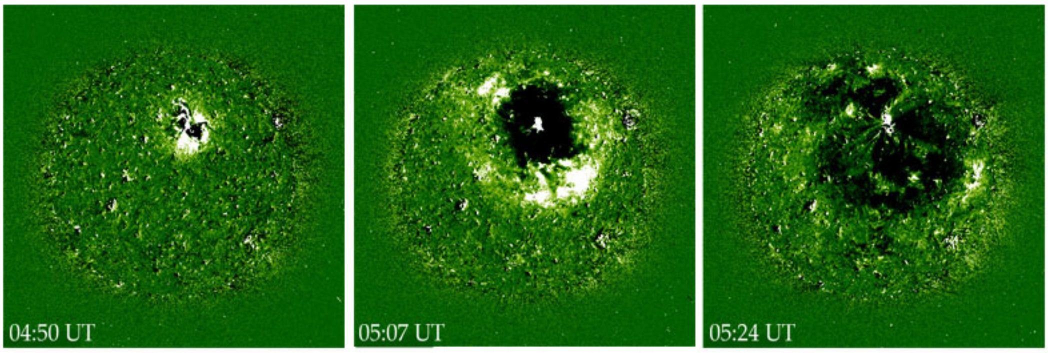

Figure 1.23: One of the first observed coronal bright fronts, reported by (Thompson *et al.*, 1998). The images are EIT Å base differenced so the bright front can be seen expanding across the solar disk. This bright front is postulated to be a magnetohydrodynamic wave propagating in response to an eruptive event in the solar corona.

propagating the low corona in response to a flare eruptive event. CBFs are are bight fronts imaged in EUV that propagate from an eruptive active at speeds of between 200-400 $\mathrm{km\,s^{-1}}$ (Thompson & Myers, 2009). Given their speed of propagation and their tendency to undergo reflection (Gopalswamy *et al.*, 2009), refraction (Wang, 2000), and pulse broadening (Long *et al.*, 2011), there is a prevailing hypothesis that these features are fast mode magnetohydrodynamic waves propagating through corona (Veronig *et al.*, 2010). They are known to accompany CME eruption quite closely (Biesecker *et al.*, 2002), so it is thought that a CME may be their driver i.e., as the CME expands it drives a disturbance through the corona which manifests itself as bright front in EUV images. Like CME eruption, CBFs show a clear association with type II radio bursts, with up 90% of type IIs being associated with CBFs (Klassen *et al.*, 2000). The fact that this MHD wave-like phenomena shows a clear association with a shock signature prompted the interpretation that they belong to the same MHD disturbance in the corona (Warmuth *et al.*, 2004), both driven by a CME. Indeed, type II kinematics can sometimes show a very closely correspondence with CBF kinematics (Grechnev

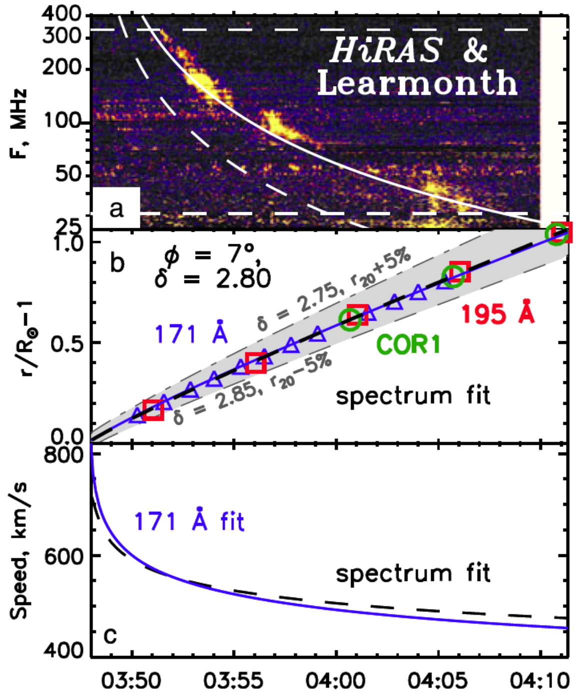

Figure 1.24: Top: Type II radio burst observed by the HiRAS spectrograph at Learmonth, Australia. Middle: Coronal bright front height time measurements from EUVI 195 Å (red squares), 171 Å (blue triangles), and COR1 (green circles). Fit to the type II burst converted to height is shown by the dashed black line. The type II burst height-time perfectly matches the eruption of the CBF as seen by EUVI and CME as seen by COR1 (Grechnev *et al.*, 2011a)

et al., 2011b; Vršnak *et al.*, 2005). Also, CBFs images at EUV may also have a counterpart images at soft X-ray (SXR) with a type II closely tied to the event e.g., the type II burst in Fig. 1.16 showed such a relationship with SXR activity (Khan & Aurass, 2002)

To further this hypothesis, there area number of studies which suggest that the origin of in-situ detection of SEPs and the type III bursts they are associated with gave their origin in the same disturbance responsible for the CBF (Klassen *et al.*, 2002; Kozarev *et al.*, 2011; Krucker *et al.*, 1999). The idea naturally leads to the following physical scenario: the CME eruption drives a pressure pulse, observable in the low corona as a propagating wave (CBF). Higher in the corona this same pulse forms a shock, accelerating particles and producing type II. If

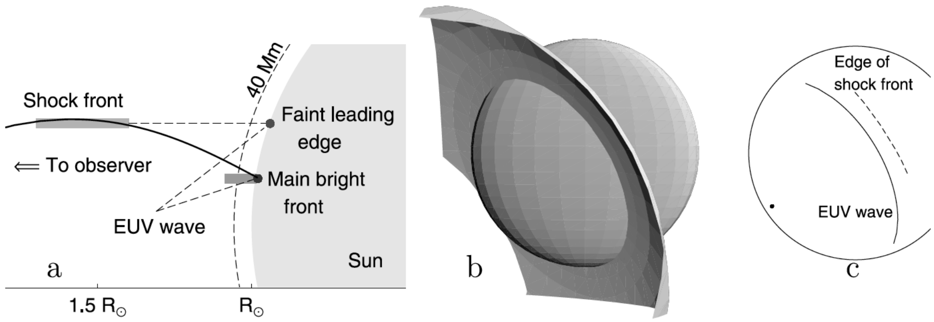

Figure 1.25: Model of a coronal disturbance resulting in a CBF in the low corona, and a steepening into a shock higher in the corona (Grechnev *et al.*, 2011a).

this shock encounters open magnetic field lines it may accelerate particles along the open field, producing type III emission and possible the subsequent detection of in-situ SEPs. Hence the unifying theme amongst the CME, CBF, radio burst, and particles is a CME driven shock.

However, such a mechanism may be called into doubt, given that CBFs can often display kinematics that may not be explained by a wave. This has prompted a sort of pseudo wave interpretation, whereby the erupting CME produces a large-scale restructuring or reconnecting of coronal magnetic field (Attrill *et al.*, 2007; Chen *et al.*, 2002). The bright front may also be due to current shell around the CME as it encounters the coronal field during eruption, this may result in a bright pulse via Joule plasma heating (Delannée *et al.*, 2008) that is not actually a driven wave. In this scenario, any relationship with shock observables is indirect, and the relationship with the particle acceleration process may be brought about by magnetic reconnection, such as interchange reconnection at the flanks of a CME (Maia & Pick, 2004). Hence it is not clear how close the relationship of CBFs is to the many shock observables in the corona e.g., is the CBF a low-coronal low-amplitude counterpart of a shock front higher in the corona? Are radio bursts and particle acceleration in any way associated with this shock front? Despite a

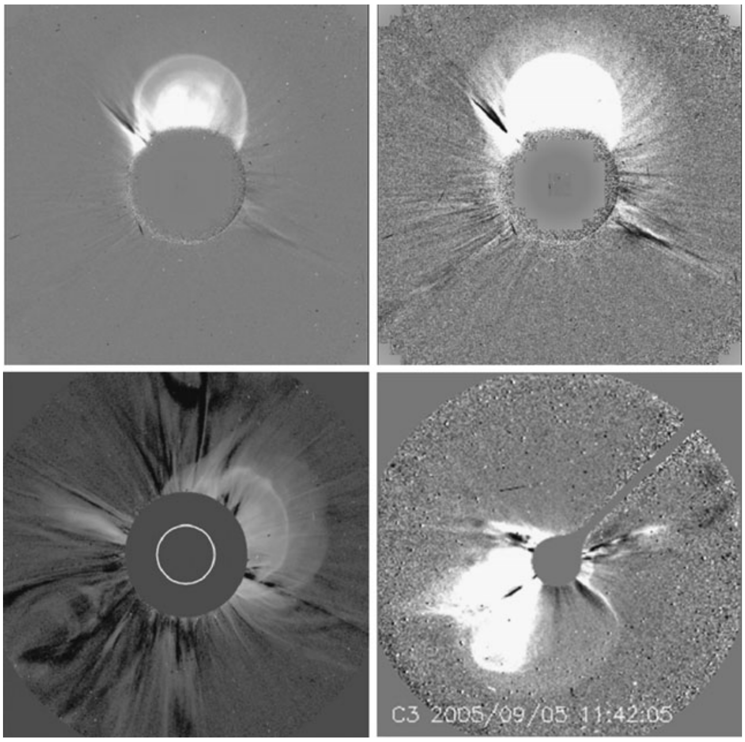

Figure 1.26: White-light shock (Vourlidas *et al.*, 2013)

close temporal correspondence between radio bursts and CBFs, the link has not been definitively proven or discredited.

1.3.4 White-light Shocks

There is a wealth of evidence in radio and ultraviolet to suggest the transit of CME driven shocks in the corona. Some of this evidence suggests that these shocks may occur at the CME flank as well as ahead of its apex. It has been suggested in some studies that these shocks may be directly images in white-light coronagraph images (Vourlidas & Bemporad, 2012; Vourlidas *et al.*, 2013). Under high contrast a much fainter front may be seen ahead of the main front. This 'two-front' morphology is a common occurrence in white-light CME structure and constitutes a reliable signature of a CME front followed by a stand-off shock (Vourlidas *et al.*, 2013). In many instances they have been used as qualitative confirmation for the presence of a CME driven shock in the corona. Indeed, it has been used to identify shock candidates at the flank of a CME (Vourlidas *et al.*, 2003). However, some studies have inferred various quantitative shock parameters such as the compression ratio (Ontiveros & Vourlidas, 2009), or by considering the shock geometry. Stand-off shocks are a common occurrence in nature and their theoretical development in an astrophysical context has been applied to planetary magnetospheric bow shocks whereby the radius of curvature of the driver and the stand-off distance between the nose of the driver and the bow shock may allow a calculation of the Mach number (Spreiter *et al.*, 1966). This applies to shocks on all physical scales, from bullets and aircraft, to planetary planetary magnetospheres and CMEs (Russell & Mulligan, 2002). In its application to CMEs, the theory was used to derived coronal magnetic field (Kim *et al.*, 2012), shock Machs in the low corona (Gopalswamy *et al.*, 2012), as well as Mach numbers in the outer corona as far as $\sim 0.5\,A.U.$ (Maloney & Gallagher, 2011).

1.4 Thesis Outline

The work in this thesis advances the understanding of CME masses, energies and forces. To date, these properties have been severely hindered by the very large uncertainties in CME masses. This has been due to the unknown propagation direction and width of the CME, making a determination of the uncertainties on the mass impossible. This has lead to uncertain kinematics, and nearly no CME forces studies from observation. Hence this thesis will show how CME mass, energies quantified more reliably and with much reduced uncertainty, as well as for the first time in the field, a quantification the forces acting on CMEs. Secondly, this thesis will outline the behavior of CMEs and radio bright shocks in the low corona. Up until now, the relationship between CME, CBFs, and radio bursts has been speculative. This work will show that the relationship between these phenomena is a plasma shock. Furthermore, it will show that this shock was driven by the expansion of the CME flank, and was responsible for bursty particle acceleration.

Chapter 2 will first discuss CME theory and related phenomena. Secondly it will discuss the plasma shock theory that is relevant to this study i.e., the MHD Rankine-Hugoniot relations, shock particle acceleration, and radio burst generation. Chapter 3 will discussed the variety of instrumentation used in this study, including the installation of the Rosse Solar Terrestrial Observatory (RSTO). Chapter 4 involves the CME masses, kinematics and dynamics work, while Chapter 5 will discuss the CME, CBF, radio bursts and plasma shock work. Chapter 6 will summarise the main findings and conclusions of this thesis.

2

Coronal Mass Ejection and Plasma Shock Theory

This chapter introduces the theory used to study coronal mass ejections and coronal shocks. Since the corona is a plasma, the theoretical framework under which all coronal phenomena are treated is in plasma physics and a fluid description of plasmas known as magnetohydrodynamics (MHD). Coronal mass ejections are a large scale phenomena and can therefore be treated using MHD. While plasma shocks on the large scale may also be treated in an MHD continuum framework, it is necessary to consider individual particle motions when describing particle acceleration and radio emission in shocks, requiring a departure from MHD and the use of distribution functions, the Boltzmann equation, and individual particle kinematics. Therefore, both the MHD equations and the Boltzmann equation are presented in this chapter, followed by an application of this theory to CMEs and plasma shocks.

2.1 Plasma Physics and Magnetohydrodynamics

2.1.1 Maxwell's Equations

Maxwell's equations forma closed set of four unknowns and four equations describing relationships between the electric field **E**, the magnetic field **B**, the current density j, and the charge density ρ_q

$$\nabla \cdot \mathbf{E} = \frac{\rho_q}{\epsilon_0} \tag{2.1}$$

$$\nabla \cdot \mathbf{B} = 0 \tag{2.2}$$

$$\nabla \times \mathbf{E} = -\frac{d\mathbf{B}}{dt} \tag{2.3}$$

$$\nabla \times \mathbf{B} = \mu_0 \mathbf{j} + \frac{1}{c^2}\frac{d\mathbf{E}}{dt} \tag{2.4}$$

μ_0 and ϵ_0 are the magnetic permeability and electric permittivity of free space, respectively, and all bold face quantities represent vector variables. At velocities typically found in a plasma (2.4) (Ampére's law) reduces to

$$\nabla \times \mathbf{B} = \mu_0 \mathbf{j} \tag{2.5}$$

where the displacement current is no longer included. Maxwell's equations describe electromagnetic beahviour and they constitute an important part of the fluid description of plasmas. Before we define this fluid description a brief discussion of plasma kinetic theory, from which the fluid theory is derived, is provided here.

2.1.2 Plasma Kinetic Theory

The general approach to the majority of plasma phenomenon is in a collective description using particle distribution functions and the use of differential equations to describe the evolution of these distribution functions. This is known as plasma kinetic theory, and the distribution functions can be of the form of the Maxwell velocity distribution, while the differential equation used to describe its evolution is the Boltzmann equation. Many non-equilibrium or unstable states of a plasma, such as those that produce radio bursts described in section X,Y, Z, require a kinetic theory description of plasma. A brief overview of kinetic theory is therefore given here before describing specifically its application to plasma emission and radio bursts.

As with a neutral gas, the particle distribution function $f(\mathbf{r}, \mathbf{v}, t)d\mathbf{v}d\mathbf{r}$ described the number of particles having positions between $\mathbf{r}$ and $\mathbf{r} + d\mathbf{r}$ and velocities between $\mathbf{v}$ and $\mathbf{v} + d\mathbf{v}$, at time t. This ditribution function can be used derive a number of useful physical properties of the plasma, such as the particle number density at position r and time t is then

$$n(\mathbf{r}, t) = \int f(\mathbf{r}, \mathbf{v}, t)d\mathbf{v} \tag{2.6}$$

as well as the bulk velocity particle velocity is given by

$$\mathbf{v}(\mathbf{r}, t) = \frac{1}{n(\mathbf{r}, t)} \int \mathbf{v} f(\mathbf{r}, \mathbf{v}, t)d\mathbf{v} \tag{2.7}$$

The evolution of this distribution function in time and space is described by the

Boltzmann equation, given by

$$\frac{\partial f(\mathbf{r},\mathbf{v},t)}{\partial t} + (\mathbf{v}\cdot\nabla_r)f(\mathbf{r},\mathbf{v},t) + (\mathbf{a}\cdot\nabla_v)f(\mathbf{r},\mathbf{v},t) = \left(\frac{\partial f(\mathbf{r},\mathbf{v},t)}{\partial t}\right)_{coll} \tag{2.8}$$

This equation describes the changes in occupation number of particles at positions (r,v,t) is phase space due to a configuration space flux $\mathbf{v}\cdot\nabla_r f$, a velocity space flux $\mathbf{a}\cdot\nabla_v f$, as well as collisions experienced by the particles. It is the fundamental basis of all plasma and neutral gas kinetic theory and provides a very powerful tool for describing the time and space evolution of equilibrium and, more importantly, non-equilibrium distribution of particles. It is the most general description of the behavior of an ensemble of particles and all other macroscopic fluid dynamical equations may be derived from it.

Assuming the plasma to be collisionless and stating the accelerations in the plasma in terms of the electric field E and magnetic field B, the Boltzmann may be reduced to the Vlasov equation for a plasma interacting with electromagnetic fields.

$$\frac{\partial f}{\partial t} + (\mathbf{v}\cdot\nabla_r)f + (\frac{q}{m}[\mathbf{E}+\mathbf{v}\times\mathbf{B}]\cdot\nabla_v)f = 0 \tag{2.9}$$

where q is Coulomb charge, m is particle mass, and $f(\mathbf{r},\mathbf{v},t)$ is reduced to f for simplicity of notation. This form of the Vlasov equation is used in the formulation of wave-particle interactions, and wave growth in plasmas, that ultimately lead to plasma emission in solar radio bursts, this will be described in further detail section X.

In equations 2.6 and 2.7, the number density and bulk velocity of the plasma were obtained by taking appropriate weighted integrals of the distribution function. This is done to obtain information on the macroscopic properties of the plasma when the specific details of the particle distribution are not needed. A behaviour of the plasma on a macroscopic or fluid scale may be obtained by taking the appropriate integrals of the the Boltzmann equation in a procedure known as 'taking the moments of the Boltzmann equation'. The moments of a function are given by

$$\mu_n = \int x^n f(x) dx \tag{2.10}$$

where the n describe the moments e.g., $n = 0$ is the *zeroth moment*, $n = 1$ is the *first moment* etc. Taking the moments of the Boltzmann equation lead to a set of fluid conservation equations that describe the dynamics of a plasma on a continuum scale (no particle motion available). The moments are as follows

$$\begin{aligned}
\int [\text{Boltzmann eq.}] \times v^0 dv &\rightarrow \text{conservation of mass} \\
\int [\text{Boltzmann eq.}] \times v^1 dv &\rightarrow \text{conservation of momentum} \\
\int [\text{Boltzmann eq.}] \times \frac{v^2}{m} dv &\rightarrow \text{conservation of energy}
\end{aligned}$$

In its most fundamental form, these conservation equations are used in what is known as a multi-fluid description of the plasma, where the dynamics and conservations of the various properties are treated seperately for each particle species e.g., electrons and protons will have different conservation equations and described separately as an 'electron fluid' and 'proton fluid'. However, combining these separate fluids into one 'single fluid' framework constitutes a description of plasmas known as magnetohydrodynamics[1].

[1] The moments of the distribution function and the reduction of multi-fluid to single fluid conservation equations involve lengthy derivations that are not provided here but can be found in many texts (Goossens, 2003; Inan & Golkowski, 2011).

2.1.3 Magnetohydrodynamics

The conservation principles derived from moments of the Boltzmann equation are firstly the mass conservation equation

$$\frac{D\rho}{Dt} = -\rho\nabla \cdot \mathbf{v} \tag{2.11}$$

where ρ is mass density, $\mathbf{v}$ is bulk flow velocity, t is time, and D represents a Lagrangian derivative. This expression simply states that the rate of change of particle into or out of a volume is controlled by the fluid flow into and out of the volume.

The momentum conservation equation is

$$\rho\frac{D\mathbf{v}}{Dt} = -\nabla p + \mathbf{j} \times \mathbf{B} + \mathbf{f} + \nabla \cdot \mathbf{S} \tag{2.12}$$

where p is thermal pressure, $\mathbf{j}$ is the current density, $\mathbf{B}$ is the magnetic field, $\mathbf{f}$ are all body forces (gravity), and $\mathbf{S}$ is a stress tensor. This equation shows that the change in momentum of a fluid may be due to a pressure gradient, the 'j cross B' or Lorentz force, gravity, and any stresses in the plasma e.g., kinematic viscosity ν. Note that with $\nabla \cdot \mathbf{S} = \rho\nu\nabla^2\mathbf{v}$, and setting gravity and the Lorentz term to zero gives the Navier-Stokes equation of motion of a viscous fluid. Note that all terms in this equation have the form of a body force (force per unit volume), and integration of volume would render this equation an explicit version of Newton's second law ($m\mathbf{a} = \mathbf{F}$)

The third conservation equation is is the internal energy conservation

$$\rho\frac{De}{Dt} + p\nabla \cdot \mathbf{v} = \nabla \cdot (\kappa \cdot \nabla T) + \eta_e\mathbf{j}^2 + Q_\nu - Q_r \tag{2.13}$$

where

$$e = \frac{p}{(\gamma - 1)\rho} \tag{2.14}$$

is the internal energy per unit mass, γ is the ratio of specific heats, κ is the thermal conductivity, T is the temperature, η_e is electrical resistivity, Q_ν is heating by viscous dissipation, and Q_r is a radiative term. This equation demonstrates that any changes in the fluid internal energy are due to divergence in the flow field, conduction, ohmic and vicious dissipation, and radiative losses.

The fluid momentum equations can be used to formulate Ohm's law for a plasma which describes the behaviour of current in terms of electric and magnetic fields and the fluid flow velocity

$$\mathbf{j} = \sigma(\mathbf{E} + \mathbf{v} \times \mathbf{B}) \tag{2.15}$$

This is a reduced version of the generalised Ohm's law which contains terms for the Hall effect, ambipolar diffusion, and electron intertia. The set of equations (2.11 - 2.15), combined with an equation of state

$$p = nk_BT \tag{2.16}$$

results in a fully closed set of variables and equations which can be solved for any fluid or electromagnetic property. In order to further simplify these set of equations the electric field $\mathbf{E}$ and current $\mathbf{j}$ are often eliminated by using Faraday's law in combinations with Ampére's and Ohm's law to produce the induction equation

$$\frac{\partial \mathbf{B}}{\partial t} = \nabla \times (\mathbf{v} \times \mathbf{B}) + \eta \nabla^2 \mathbf{B} \tag{2.17}$$

which describes the evolution of the field in terms of the plasma flow and the magnetic diffusivity $\eta = \eta_e/\mu_0$. The mass, momentum, internal energy equation, the induction equation, and the solinoidal constraint then define a fully closed system of resistive MHD equations in terms of the variables $(\mathbf{B}, \mathbf{v}, p, \rho)$

$$\frac{D\rho}{Dt} = -\rho\nabla\cdot\mathbf{v} \tag{2.18}$$

$$\rho\frac{D\mathbf{v}}{Dt} = -\nabla p + \frac{1}{\mu_0}(\nabla\times\mathbf{B})\times\mathbf{B} + \mathbf{f} \tag{2.19}$$

$$\frac{D\rho}{Dt} = -\gamma p\nabla\cdot\mathbf{v} + (\gamma-1)\frac{\eta}{\mu_0^2}(\nabla\times\mathbf{B})^2 \tag{2.20}$$

$$\frac{\partial\mathbf{B}}{\partial t} = \nabla\times(\mathbf{v}\times\mathbf{B}) + \eta\nabla^2\mathbf{B} \tag{2.21}$$

$$\nabla\cdot\mathbf{B} = 0 \tag{2.22}$$

It is also assumed here that the fluid is inviscid and not subject to any conductive or radiative energy losses or gains. Under this reduced set of equations, the ideal MHD equations are simply produced by setting $\eta = 0$ e.g., zero resistivity, which would eliminate the second terms on the right in equations 2.20 and 2.10. Under such an assumption the ideal induction equation

$$\frac{\partial\mathbf{B}}{\partial t} = \nabla\times(\mathbf{v}\times\mathbf{B}) \tag{2.23}$$

may be used to show the ‘frozen flux’ condition. This shows that when $\eta = 0$ the field is advected with the plasma or the field is ‘frozen-in’ into the plasma and follows the flow velocity. On the other hand, a finite η leads to a variety of important diffusive effects for the magnetic field. The most important of these diffusive processes is magnetic reconnection.

2.1.4 Magnetic Reconnection

If the dissipation of concentrations of magnetic flux are due to diffusion processes only, a timescale for this diffusion process may be estimated from the magnetic induction equation. Assuming the diffusion term dominates over advection term

$$\frac{\partial B}{\partial t} = \eta \nabla^2 \mathbf{B} \tag{2.24}$$

As an order of magnetiude estimate for the derivatives we replace $\partial/\partial t \rightarrow 1/\tau_D$ and $\nabla^2 \rightarrow 1/L^2$. Equation 2.24 then gives

$$\tau_D = \frac{L^2}{\eta} \tag{2.25}$$

The typical length scales for a coronal active region are $10^7\,\mathrm{m}$, and assuming a Spitzer magnetic diffusivity $\eta = 10^9 T^{-3/2} = 1\,\mathrm{m}^2\,\mathrm{s}^{-1}$ (Spitzer, 1962), which gives a diffusive timescale of 3.1 million years. Given that active regions evolve quasi-statically over weeks and evolve dynamical over timescales of minutes during a flares and CMEs, there must be an evolution process other than a large scale diffusion in the solar atmosphere. Equation 2.25 indicates that there may be two different ways in which the evolution of magnetic fields may occur over a much shorter times scale: either typical length scale L is much shorter, or magnetic diffusivity η is much larger.

Magnetic reconnection is the dynamical process that describes the short timescale evolution of magnetic fields in the corona (and other astrophysical and laboratory systems). It involves a change in magnetic topology that converts magnetic energy in kinetic and thermal energy of the bulk plasma and accelerates particles to high speeds. Magnetic reconnection typically occurs in a boundary between two oppositely directed magnetic field regions. At the very center of the boundary layer the magnetic field must go to zero to account for a continuous change from positive to negative magnetic field. The total pressure balance in the boundary layer and on either side is

$$B_1 + p_1 = p_{dr} = B_2 + p_2 \tag{2.26}$$

where $p_{1,2}$ and $B_{1,2}$ represent thermal and magnetic pressure on either side of the diffusion region, respectively, and p_{dr} is the pressure inside the diffusion region (no magnetic pressure).

The existence of inflows into the neutral layer at right angles to the magnetic field creates an electric field in this later that is perpendicular to the inflow plane. This creates a current in this boundary layer, hence this boundary layer is often called a current sheet. The diffusion of magnetic fields occurs within this current sheet. Sweet and Parker were the first devise a mechanism by which magnetic reconnection occurs in such a current sheet Parker (1963); Sweet (1958). Although no complete analytical theory exists for the process, the MHD conservation equations may be applied to derive the reconnection rate. The application of resistive MHD only applies within the thin current sheet, while ideal MHD applies everywhere else.

The Sweet-Parker reconnection model consists of a current sheet (diffusion region) that is much longer than it is wide i.e., $L >> \delta$ where is current sheet half-length and δ is current sheet half-thickness. The reconnection rate depends on in the ratio of the inflow speed v_{in} to v_{out} in the form of the Mach number

$$M = \frac{v_{in}}{v_{out}} = \frac{1}{\sqrt{S}} \tag{2.27}$$

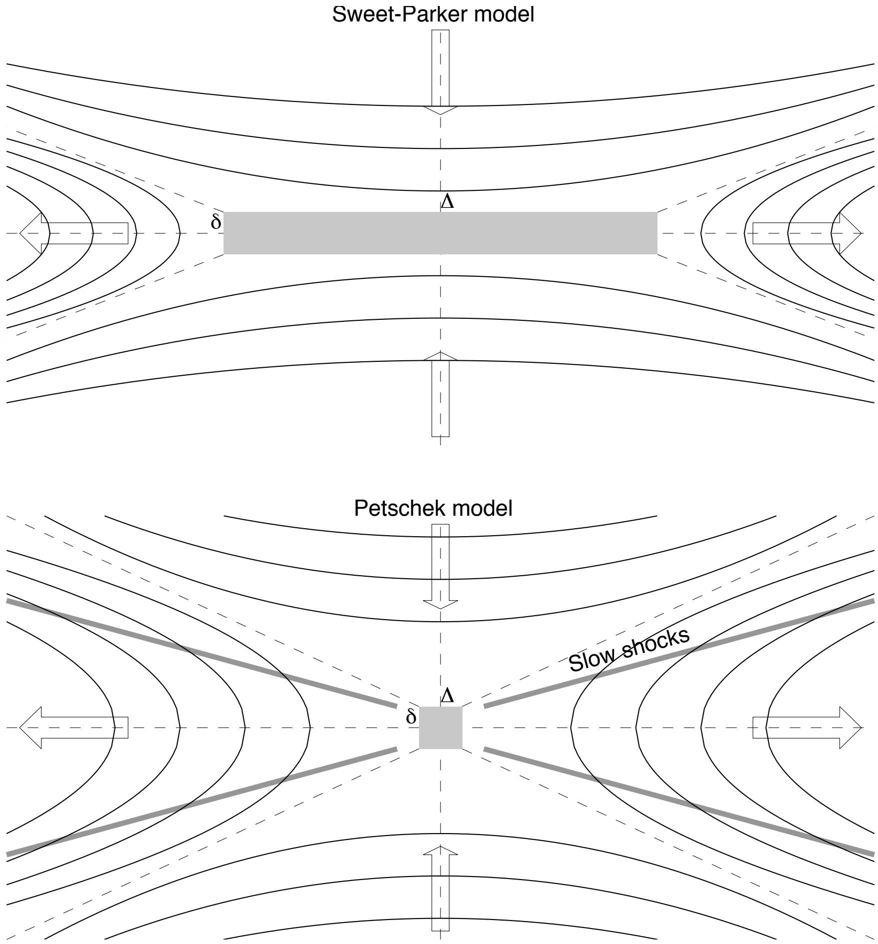

Figure 2.1: The reconnection models of Swee-Parker (top) and Petscheck (bottom). The Sweet-Parker mechanism employs a long and thin ($L >> \delta$) current sheet as the diffusion region. It produces reconnection rates that are much too slow to describe flare and CME energy dissipations rates. Petscheck proposed a similar model but with a diffusion region that is much smaller, with $L \approx \delta$, resulting in reconnection rates that are consistent with flare and CME timescales. The dissipation of energy in this model is partly controlled by the presence of two slow-mode shocks which separate the sub-Alfvénic inflow region and the super-Alfvénic outflow region (Aschwanden, 2004).

where $S = v_A L/\eta$ is the Lundquist number (equivalent to the magnetic Reynold's number at the Alfvén speed. The rate of reconnection depends on the length scale and magnetic diffusivity in the current sheet. Despite the fact that the Sweet-Parker mechanism provides a rate of magnetic energy dissipation that is faster than the global process, it is much too slow to explain the process of magnetic energy release in solar flares. The Sweet-Parker model is known as slow reconnection. PUT IN SOME NUMBERS

To over come the problem, Petscheck proposed a model with a much smaller diffusion region where $L \approx \delta$ (Petschek, 1964) . With this smaller diffusion region, the boundary between inflow and outflow regions are separated by slow mode magnetoacoustic shocks. Alongside the diffusion region, these shocks also help to dissipate some of the inflowing kinetic energy into thermal energy. Again, no analytical solution to the model exists but Petscheck found that when the diffusion regions is allowed to be small, the reconnection rate is given as

$$M \approx \frac{\pi}{8 \ln(S)} \tag{2.28}$$

This gives a much faster reconnection rate of X (hence it is known as fast reconnection), which is comparable to solar flares. When Petscheck presented the model it was thought to be a complete description of 2D magnetic reconnection, however other solutions would soon be discovered, with the Petscheck model being just one of a family of possible 2D reconnection mechanisms. These mechanisms describe steady, uniform, 2D reconnection, the rate of which may be summarised as (Priest & Forbes, 1986)

$$\left(\frac{M_e}{M_e}\right)^2 \approx \frac{4M_e(1-b)}{\pi}\left[0.834 - \ln\tan\left(\frac{4S\sqrt{M_e M_i}}{\pi}\right)^{-1}\right] \tag{2.29}$$

This contains the Sweet-Parker, the Petscheck ($b = 0$) and Sonnerup (Sonnerup, 1970)($b = 1$) reconnection rates.

2D reconnection, an the more complicated 3D models, play a role in many theoretical models describing the eruption of coronal mass ejections and flares. Although some CME models have no need for reconnection to occur, there is a growing consensus that it is an integral part of the solar eruptive process.

2.2 Coronal Mass Ejections

Magnetohydrodynamic models of eruptive coronal mass ejections use either ideal or resistive MHD to bring about a loss of equilibrium of some complex magnetic structure in the corona. The magnetic structure usually takes the form of a flux rope, a helical or twisted magnetic structure embedded in the coronal magnetic field. The main goal of every model is to induce a loss of equilibrium of the structure, but the mechanism by which this is done varies greatly amongst the models. *Storage models* assume a slow build up of magnetic stress in a non-potential field that may store free energy over long time scales before some loss of equilibrium occurs and the stored magnetic energy is rapidly converted to mechanical energy and the expulsion of a magnetic structure (Antiochos *et al.*, 1999a; Forbes & Priest, 1995; Wolfson & Saran, 1998). *Dynamo models* involve a rapid generation of magnetic flux by either stressing of the field or flux-injection into the system. As the name suggests, these models usually consider the interplay between current and magnetic field in the system that may bring about a Lorentz force which provides an expulsion of the flux rope from the low corona (Chen, 1989; Fan, 2005; Krall *et al.*, 2001; Schrijver *et al.*, 2008). Finally there are the *thermal blast models*, which produce an expulsion of the CME into interplanetary space by an enhanced pressure gradient due to the rapid heating of a flare i.e., an explosive ejection of plasma from the corona. This model is somewhat out-dated now since CMEs are no longer thought to be the result of flares, with some CMEs preceding flare onset and some occurring without ay flare (Gosling, 1993).

The main goal of every model is to induce a loss of equilibrium of the structure, but the mechanism by which this is done varies greatly amongst the models e.g., there is still some debate on whether the flux rope is formed as a result of eruption or it is a pre-existing structure. The need for reconnection is also a source of contention, with some models inducing eruption using only ideal MHD and other models employing resistive MHD (Chen, 2011). The most prominent of these models are discussed here.

2.2.1 Catastrophe Model

The catastrophe model assumes a flux-rope is formed in the corona prior to eruption and considers the balance between magnetic tension holding the flux rope in position, and magnetic pressure (from compression of field lines under the rope) that supply an outward directed force (Forbes & Isenberg, 1991; Lin & Forbes, 2000; Priest & Forbes, 2000). A loss of equilibrium is brought about by photospheric motions, either convergence or shearing of the foot points, which are well-known precursors to eruptive activity in the corona (Rust, 1972). the reduction of the distances between the foot points, 2λ, decreases and this initially causes an increase int the magnetic tension which makes the rope contract and reduce its height Fig. 2.2. However, continued contraction results in a magnetic compression that dominates tension, resulting in a flux rope rise. As the rope rises it forms a current sheet behind it, and its evolution after this point depends on whether or not reconnection occurs in the current sheet. If no reconnection is present then the flux rope simply rises and finds a new equilibrium position at a greater height, in this case the net release of magnetic energy is less than 1% of the energy stored in the pre-field configuration (Forbes & Isenberg, 1991). If reconnection occurs, then the eruption proceeds uninhibited and up to 95% of the stored magnetic energy is released (Forbes & Priest, 1995).

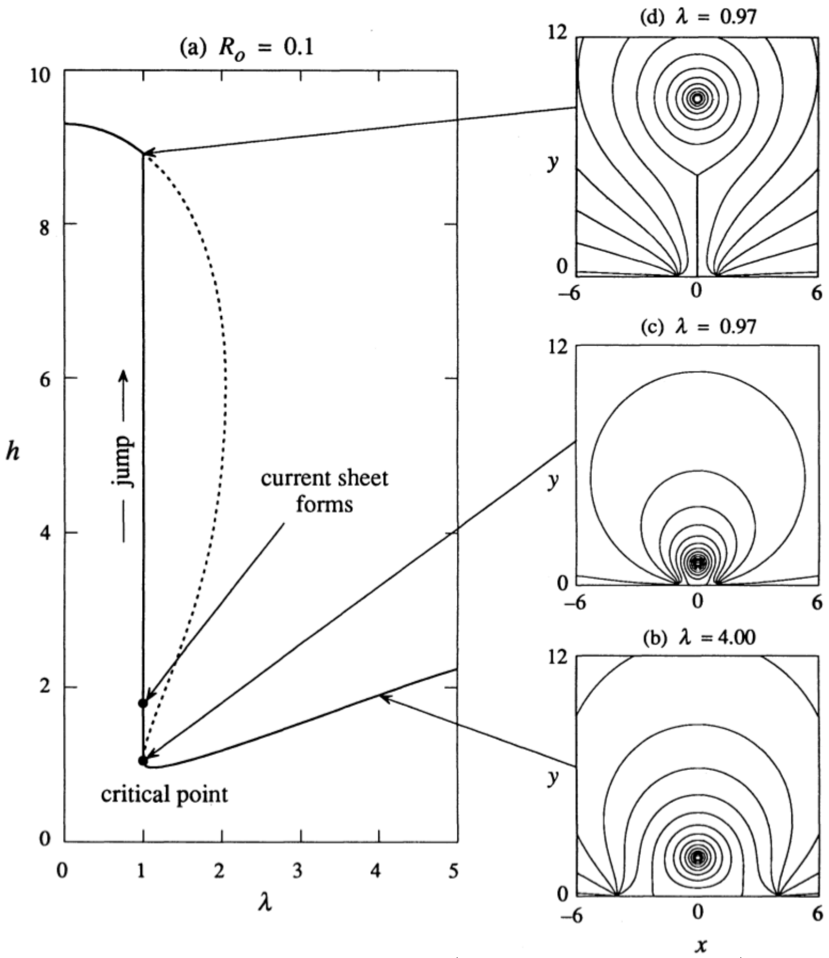

Figure 2.2: The catastrophe model of (Forbes & Priest, 1995). The model consists of a 2D pre-existing flux rope with foot points rooted in the photosphere. The fluxrope is driven toward instability by motions of the photospheric footpoints, in this case the distance between the footpoints λ decreases slowly (timescales much longer than the Alfvén crossing time $\tau = L/v_A$). As the foot points converge the fluxrope initially contracts indicated by a decreasing height in panel (a). Eventually this convergence brings the system to critical point where magnetic pressure outwards dominates inward magnetic tension. The system rises, reaches a new equilibrium position, and forms a current sheet. The evolution of the system after it reaches this new equilibrium largely depends on whether or not magnetic reconnection occurs in the sheet. the rate of reconnection may also bring about different evolutions in kinematics (Priest & Forbes, 2000).

Forbes & Priest (1995) provided expressions for the development of current in the flux rope with respect to height which was used to estimate the free magnetic energy in the system. By assuming a rapid reconnection rate, and that all of this free energy was converted to the rope's kinetic energy they were able to derive velocity-time kinematics, and under the constraint of the flux rope radius $a \to 0$ an analytical expression for the rope velocity may be derived as (Priest & Forbes, 2000)

$$v \approx \sqrt{\frac{8}{\pi}} v_{A0} \left[\ln\left(\frac{h}{\lambda_0}\right) + \frac{\pi}{2} - 2\tan^{-1}\left(\frac{h}{\lambda_0}\right) \right] + v_0 \tag{2.30}$$

where h is the fluxrope height, $2\lambda_0$ is the foot point separation at $\lambda = h$, v_0 is an initial perturbation velocity (1% of the Alfvén speed), and v_{A0} is the Alfvén speed where $\lambda = h$. Magnetic power output in the early phase of eruption is given by

$$\frac{dW}{dt} \approx -\frac{2A_0^2}{\pi\mu}\left(\frac{h}{\lambda_0} - 1\right)^2 \frac{v}{\lambda_0} \tag{2.31}$$

where $h \sim t + t^{5/2}$ and $v \sim t^{3/2}$ i.e., the initial power output grows with time. In the later phases of propagation the power output decays with time as

$$\frac{dW}{dt} \approx \frac{4A_0^2}{\pi\mu t} \tag{2.32}$$

so the growth in power output occurs approximately 100 times quicker than the decay in power output.

A later study by Priest & Forbes (2000) analysed how reconnection in the underlying current sheet may influence the eruption of the flux rope. The kinematics of the rope after equilibrium is lost depend on the rate of reconnection in the sheet, parameterised by the Alfvén Mach number of the inflow into the reconnection site. If $M_A = 0$ then the fluxrope does not escape but oscillates around an equilbrium height like a yo-yo. If $0 < M_A < 0.005$ then escape is possible but the rope may show a number of oscillations in height before escape, this behaviour has never been directly observed so reconnection must occur at a rate $M_A > 0.005$ to produce eruption. For $0.005 < M_A < 0.041$ to rope escape but undergoes a period of deceleration between 20 and 100 Alfvén crossing times, while for $M_A > 0.041$ no deceleration occurs and the fluxrope escapes and approaches an asymptotic velocity.

The catastrophe model provides a successful way of evolving a flux system to the point of catastrophic loss of equilibrium and consequent eruption. However, a major limitation is that it is a 2D model and does not take into account that the ends of the flux rope will be anchored in the photosphere. This would produce a curvature in the rope that would increase its tension and hence change the dynamics, but it is unlikely that it would prevent eruption (Steele *et al.*, 1989)

2.2.2 Magnetic Breakout Model

The magnetic breakout model was first proposed by (Antiochos *et al.*, 1999a) and involves a quadrupolar (or more complex) magnetic flux system. A core magnetic field is flanked by two side-lobe fields, which collectively lie underneath an over-arching field that stabilizes the whole system. The overarching field and core field are almost anti-parallel, creating a magnetic null point between the two Figure 2.3. Non potentiality is injected into the core by twisting/shearing of the foot points or by flux emergence. This non-potentiality causes the core field to grow and encounter the overarching field, distorting the null point into a current sheet and eventually allowing reconnection to occur. The reconnection removes field lines from the overarching field and adds it to the side-lobe systems, allowing further growth of the core field. The growth of the core field in turn drives further breakout reconnection resulting in a positive feedback required for explosive expulsion of the core. Finally, as the core is accelerated a current sheet forms in its wake, eventually leading to a separation of the core flux from the solar surface that forms a plasmoid structure typical of a three part CME (Lynch *et al.*, 2004); an important aspect of this is that flux rope formation happens as a

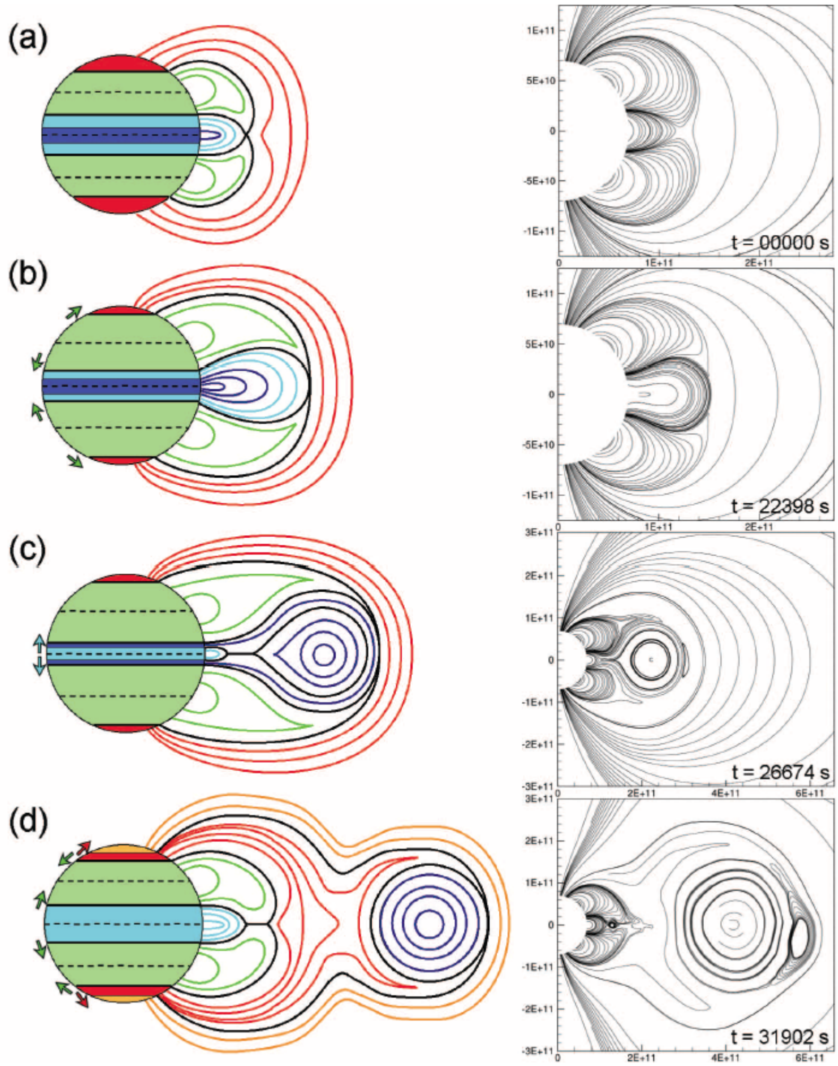

Figure 2.3: The breakout model, consisting of a quadrupolar flux system in which the central flux (blue) is flanked by to side lobe flux systems (green), with the entire system kept in stability by the tension of the overlying red field. Shearing and/or twisting on the underlying flux causes it to grow slowly. Eventually a current sheet forms at the magnetic null above the central flux, causing reconnection. This reconnection transfers overlying field to the side-lobes, effectively creating a conduit for the central flux to escape as a CME (Lynch *et al.*, 2008).

consequence of eruption i.e., it is not pre-existing. The magnetic breakout model was used to circumvent the Aly-Sturrock limit (Aly, 1991; Sturrock, 1991) i.e., it allowed a flux system to erupt, without having to open the constraining field lines to infinity.

Kinematically, the CME/central field system should experience a slow rise ($1\,\mathrm{km\,s^{-1}}$) for several hours due to shearing/twisting of the foot points. Once breakout reconnection has begun the CME experiences a much larger acceleration ($100\,\mathrm{km\,s^{-1}}$). The reconnection in the current sheet in the wake of the CME is the source of energetic particles that ultimately lead to flaring (ribbons and soft x-ray loops). Therefore magnetic breakout predicts that the flaring process and SXR peak should only begin after CME acceleration (after breakout reconnection) has begun (Lynch *et al.*, 2004). However, the precedence in breakout reconnection over flaring reconnection may not always be case, with the latter sometimes driving the former (MacNeice *et al.*, 2004).

There has been observational tests of the magnetic-breakout model, showing it to be a viable explanation of some flaring and CME events, the most notable of which is the Bastille Day event (Aulanier *et al.*, 2000). The observational signatures of the model include the presence of a null point in the corona above a complex multipolar flux system (inferred from potential field source surface extrapolations), a radio source imaged to be above the erupting structure (implying a reconnection site), and radio bursts beginning at frequencies indicative of high altitude (again indicating energy release above the erupting structure, prior to eruption) (**?**). However, in some instances magnetic breakout is implied by observations of the above, but the kinematics are inconsistent with model predictions. For example the model predicts a long slow rise of the central flux system as the underlying field is increasingly sheared, after which there is a rapid acceleration once breakout reconnection is initiated. However, in the study of Bong *et al.* (2006) the breakout reconnection occurred at the end of the CME acceleration phase, prompting a two-phase acceleration scenario.

2.2.3 Toroidal Instability

The toroidal instability model incorporates a pre-existing flux rope structure that is built from a torus of magnetic flux, some of which is buried beneath the photosphere (Chen, 1989). The flux system is can be broken down into a combination of toroidal magnetic, toroidal current and a poloidal magnetic field and current Figure 2.4. This flux rope system is embedded in a surrounding coronal magnetic field B_{corona}. The stability of the system depends on the nature of the $J \times B$ force due to the interaction toroidal and poloidal components of both the field and current. The interaction of J and B internal to the flux rope is usually termed the Lorentz self-force or the 'hoop' force. An instability may be induced via twisting of the fluxrope footpoints to increases the amount of poloidal flux (effectively increasing the helicity of the system). The instability arrises when the outward hoop force decreses more slowly within the ring radius than the opposing Lorentz force due to an external magnetic field. Once the instability is induced, the fluxrope begins a bulk motion as well as a growth in its semi-minor axis. Hence the motion of the system can be analysed by looking at the central axis or the minor axes (leading and trailing edges. The three axes display slightly different kinematics e.g., the leading edge has a faster velocity than the trailing edge (due to fluxrope expansion). this has proved a useful test of the model when comparing the observations of erupting fluxrope structures as seen in white-light coronagraphs. Krall *et al.* (2001) looked at the leading a trailing edges of erupting flux ropes, as well as the rope aspect ratio, an compared the observations to model expectations. Good agreement is found between the model kinematics and aspect ratio and the observed events. The equation of motion of the entire

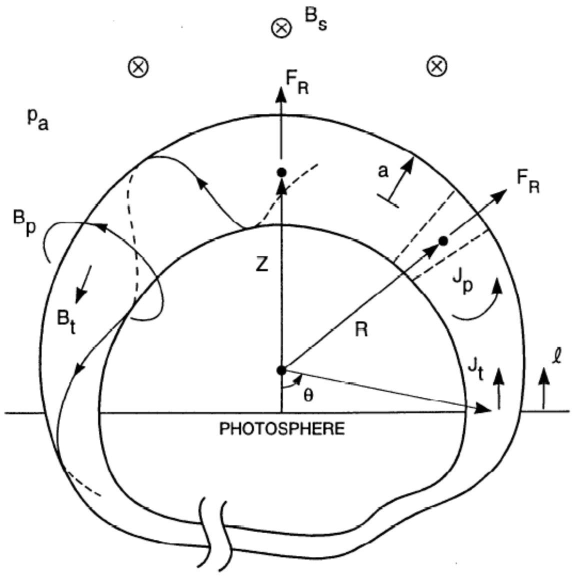

Figure 2.4: The flux rope model of Chen (1989), used to to study the toroidal instability of a twisted flux system in the corona.

system is given by

$$M\frac{d^2Z}{dt^2} = \frac{I_t}{c^2R} \times \left[\ln\left(\frac{8R}{a}\right) - 1 + \frac{\xi_i}{2} + \frac{\beta_p}{2} - \frac{B_t^2}{B_{pa}^2} - \frac{2RB_{\perp c}}{aB_{pa}}\right] - F_g - F_{drag} \quad (2.33)$$

where I_t is the toroidal current, R is the flux rope major radius, a is the rope minor radius, ξ_i is internal inductance of the flux system, B_t is the toroidal field, B_{pa} is the poloidal field at a, $B_{\perp c}$ is the perpendicular component of the ambient coronal field, F_g is the force due to gravity, F_{drag} is the drag force, M is the mass per unit length of the rope, and Z is the rope axis height above the photosphere. The equation of motion shows that an increase in the toroidal current (or poloidal flux) contributes positively to the acceleration. The terms in the square brackets are each unitless and take into account the rope geometry, self-inductance and interplay between poloidal and toroidal flux. The first three terms in the square brackets are what give rise to the hoop-force. If the rope is mass loaded with a prominence, this can contribute to the rope's stability via the gravity term. The drag term only becomes an important contributor to rope dynamics later in the propagation, when the solar wind speed begins to increase i.e., at around $10R_{\odot}$ reference Sheeley. The eruption is driven by flux-injection, which typically lasts for 4-8 hours, during which time the unstable system loses its equilibrium and begins to rise Krall *et al.* (2001).

It is significant the fluxrope is already established in the corona before eruption begins i.e., the rope formation is not addressed in the model and it is not a consequence of eruption. Hence magnetic reconnection is not a necessary aspect of the model and the eruption may proceed without employing resistive MHD. The model has been tested against observations and found to provide consistent result with the acceleration and jerk profiles of destabilized filaments during eruption (Schrijver *et al.*, 2008)

2.3 Coronal Shocks and Plasma Emission

2.3.1 Alfvén Speed in the Corona

The speed at which perturbations travel in a magnetized plasma is the Alfvén speed, given by

$$v_A = \frac{B_0}{\sqrt{\mu_0 \rho}} \tag{2.34}$$

where B_0 is the unperturbed (equilibrium) magnetic field, μ_0 is the magnetic permeability, and ρ_0 is the unperturbed mass density of the medium. This is a highly anisotropic wave driven by the restoring force of magnetic tension, with the inertia provided by the plasma mass density. Perturbations in the magnetic field, B_1, are transverse to the direction of B_0 and the group velocity always has a wave $\hat{k}$ vector parallel to the magnetic field direction. The

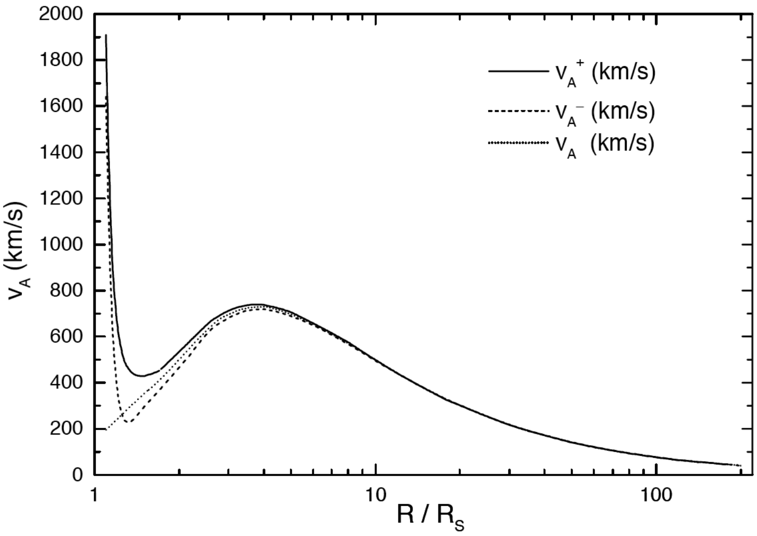

Figure 2.5: Alfvén speed of the corona as a function of heliocentric distance. The dotted line is the quite sun, with only the Sun's global dipole field. The solid line is the Alfvén speed calculated from a combination of te global dipole field and a smaller active region dipole field oriented parallel to the global dipole. The dashed line is the the speed when the active region dipole is anti-parallel to the global field. The two profiles from the active region show a distinct minimum in the coronal Alfvén speed at $\sim 1.5\, R_\odot$

quiet solar corona in the range of $1 - 3\, R_\odot$ has typical magnetic field strengths on the order of $1{-}100\,\mathrm{G} = 10^{-2}{-}10^{-3}\,\mathrm{T}$, and typical electron number densities of $10^6{-}10^9\,\mathrm{cm}^{-3} = 10^{12}{-}10^{15}\,\mathrm{m}^{-3}$, so for B_0=5 G and n_e=$10^8\,\mathrm{cm}^{-3}$ the Alfvén speed in the corona is $\sim$1000 km·s^{-1}. The variation in magnetic field and density in the corona, especially nearby an active region, v_A may be on the order of $10^2{-}10^3$ km·s^{-1}. If displacement components of the wave are perpendicular as well as parallel to the equilibrium magnetic field and non-zero perturbations in plasma thermal pressure and density occur, the result is a wave propagation known as a magnetoacoustic wave, such as the fast and slow mode MHD waves. However, given the corona is a low$-\beta$ plasma, magnetic perturbations are faster than thermal pressure ones, so the Alfvén speed is a good estimate of plasma perturbation speeds in the corona. Mann et al. produced a 1D model of the variation of Alvén speeds in the quiet and active region corona as a function of height Figure. Warmuth then improved this to a 2D model. It shows that CMEs are well capable of producing plasma hocks in the corona, since they may travel far in excess of the Alfvén speed. The theory of plasma shocks and the resulting effects of particle acceleration and plasma emission are discussed in the following sections.

2.3.2 MHD Shocks

For acoustic shock waves there are a number of conservation equations that quantify the strength of a shock by relating the upstream gas pressure, density, flow speed, and temperature to their downstream counterparts. Such conservation equations are known as the jump conditions and the shock is considered a surface at which the fluid properties change discontinuously. The shock thickness is usually of the order of a few mean free paths of the particles in the gas, in such a case the processes in the shock surface itself are inconsequential and the relationship between upstream and downstream parameters provide a sufficient description of the shock.

When the gas is ionized and a magnetic field is present, the jump conditions must be modified to take into account the magnetic pressure and the field orientation with respect to the flow velocity and shock normal $\hat{n}$ (unit vector normal to the shock plane). In the general case of oblique shock waves where the magnetic field direction has some arbitrary angle with respect to shock normal we may derive a set of conservation equations for the frame of the shock wave.

The flow velocity v and magnetic field B are considered to be in the xy-plane.

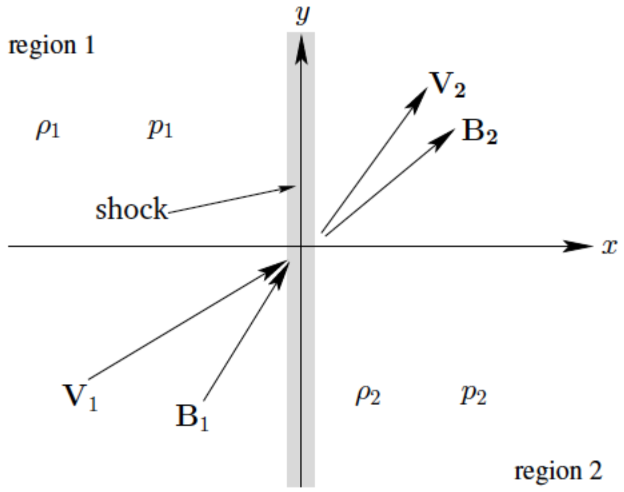

Figure 2.6: Orientation of magnetic field and velocity field with respect to shock plane, in the rest frame of the shock. Shock normal in this case would be along the $-x$ direction i.e., into upstream region 1. (Fitzpatrick, 2000)

The appropriate conservation equations are

$$[\rho v_x] = 0 \tag{2.35a}$$

$$[\rho v_x^2 + p + \frac{B_y^2}{2\mu}] = 0 \tag{2.35b}$$

$$[\rho v_x v_y - \frac{B_x B_y}{\mu}] = 0 \tag{2.35c}$$

$$[\frac{1}{2}v^2 + \frac{\gamma p}{(\gamma - 1)\rho} + \frac{B_y(v_x B_y - v_y B_x)}{\mu \rho v_x}] = 0 \tag{2.35d}$$

$$[B_x] = 0 \tag{2.35e}$$

$$[v_x B_y - v_y B_x] = 0 \tag{2.35f}$$

These are the general MHD shock jump conditions where v is the fluid velocity and B is the magnetic field (with their corresponding components 'x' or 'y'), ρ is the mass density, p is the thermal pressure, and γ is the ratio of specific heats (or the polytropic index). The meaning of the square brackets is $[F] \equiv F_1 - F_2$, for any quantity F, and the 1 or 2 subscripts represent upstream or downstream values of each quantity F, respectively. These set of jump conditions differ only from the purely acoustic ones due the presence of the magnetic field. For example, taking (4a), (4b), and (4d) and setting $B_x = B_y = 0$ we obtain the jump conditions for a neutral gas. Each conservation equation has a specific meaning;

- (4a) is a mass conservation equation whereby the mass flux entering the shock must equal the mass flux leaving. It has units of $\mathrm{kg\,m^{-2}\,s^{-1}}$.
- (4b) indicates that if mass flux $\rho_1 v_{x,1}$ enters the shock with momentum $(\rho_1 v_{x,1})v_{x,1}$ it leaves the shock with momentum $(\rho_1 v_{x,1})v_{x,2}$, the difference being equal to the the changing force per unit area across the shock. In this case both thermal and magnetic pressures contribute to change in momentum flux. (4c) implies the same process but relates the x and y components of the v and B vector fields. Both equations have units of momentum flux $\equiv (\mathrm{kg\,m^{-2}\,s^{-1}})(\mathrm{m\,s^{-1}}) = (\mathrm{kg\,m\,s^{-2}m^{-2}}) = \mathrm{N\,m^{-2}} \equiv$ pressure.
- (4c) is an energy conservation term, accounting for the rate at which gas and magnetic pressure do work per unit area at the shock and equates this to the growth (or loss) in internal energy and kinetic energy across the shock. All components of magnetic field pressure are taken into in the last term on the left of the equation. All quantities are in units of $\mathrm{J{\cdot}kg^{-1}}$.
- (4d) simply states that the x component of the magnetic field i.e., the component of the field that is (anti-)parallel to the shock normal $\hat{n}$ is unaffected by the shock transition.
- (4f) relates the orientations of the upstream and downstream magnetic field to the flow speed tangential and perpendicular to the shock normal. Magnetic field orientation and hence the distribution of low speed amongst the

velocity components largely depends on the whether the shock is slow-mode, intermediate, or fast mode. The equation has units of T·m·s^{-1} = V·m^{-1} $\equiv$ electric field.

4(a-f) are the general case of the jump conditions across an MHD shock, they are usually known as the MHD Rankine-Hugoniot (RH) equations. Their generality make the solution of the six unknowns from the six equations quite complicated. However the extreme cases of parallel and perpendicular shocks provide very useful and simplified expressions. It can be shown that parallel shocks i.e., $\hat{v} \parallel \hat{B} \parallel \hat{n}$ reduces to the jump conditions of a hydrodynamic shock in a neutral gas (here parallel and anti-parallel are used synonymously). The more interesting case when considering radiating shockwaves in the low solar corona is the perpendicular (or quasi-perpendicular) MHD shock, in this case the flow speed is parallel to the shock normal, and the magnetic field is perpendicular (or at a high angle) to it i.e., $\hat{v} \parallel \hat{n}$ and $\hat{B} \perp \hat{n}$. As will be shown it is this special case of quasi-perpendicular shocks that lead to efficient shock drift particle acceleration, a necessary precursor to the generation of radio emission at a coronal shockwave.

In the case of fully $\perp$ shocks there is no need for the decomposition of the magnetic and velocity vector fields, meaning the x and y subscripts on 4(a) and 4(b) can be dropped. 4(c) is an obsolete jump condition, likewise for 4(e) since no B_x field exists. We can also rid the B_xB_y terms from the last quotient in the energy conservation 4(d) –replacing it simply with $B^2/2\mu\rho$. 4(f) reduces to a simpler form of $[Bv] = 0$. Such a reduction in the generalized jump conditions allows us to express the upstream and downstream plasma properties in terms of the shock compression ratio $\chi = \dfrac{\rho_2}{\rho_1}$ as well as the upstream sonic Mach number

$M_1 = \frac{v_1}{c_1}$ (Priest & Forbes, 2000) e.g.,

$$\frac{v_2}{v_1} = \frac{1}{\chi} \tag{2.36a}$$
$$\frac{B_2}{B_1} = \chi \tag{2.36b}$$
$$\frac{p_2}{p1} = \gamma M_1^2\left(1 - \frac{1}{\chi}\right) - \frac{1-\chi^2}{\beta_1} \tag{2.36c}$$

where $\beta_1 = 2\mu p/B_1^2$ is the upstream plasma beta parameter. The exact value of the compression ratio may be obtained by using 4(b) to eliminate p from the energy flux equation 4(d) and incorporating 4(a,c,e,f) (and a lot of algebra) a quadratic for χ may be obtained

$$2(2-\gamma)\chi^2 + [2\beta_1 + (\gamma-1)\beta_1 M_1^2 + 2]\gamma\chi - \gamma(\gamma+1)\beta_1 M_1^2 = 0 \tag{2.37}$$

Equation (6) has one positive real root such that

$$1 < \chi < \frac{\gamma+1}{\gamma-1} \tag{2.38}$$

Using a ploytropic index of $\gamma = 5/3$ (monatomic) means the shock compression can be no more than a factor of 4. Another extremely important fact arising from this is that magnetic compression can also be no greater than 4 i.e., from equation 4(b) $B_2/B_1 = \chi$. $\chi < 4$ has consequences for the shock drift acceleration mechanism and provides an upper limit to the particle energy gain (Section 2.X)

2.3.3 Shock Particle Acceleration

The framework of shock particle acceleration for solar type II radio bursts is called the shock drift acceleration (SDA) mechanism. The mechanism involves a

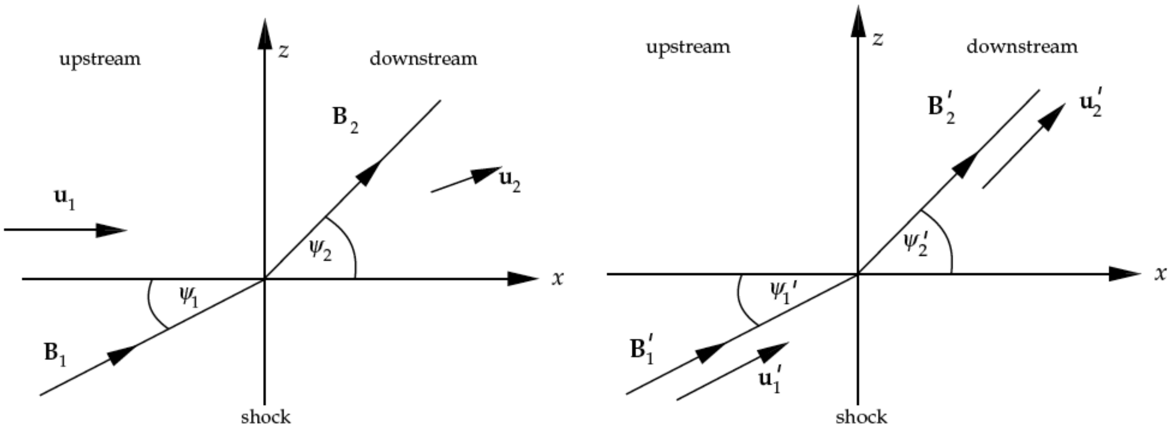

Figure 2.7: (Left) Normal incidence frame (NIF) where the shock is at rest and the upstream plamsa approaches the shock head-on at velocity $\mathbf{u}_1$. The magnetic field makes some arbitrary angle θ_{Bn} with the shock normal. (Right) Transformation to a de Hoffman-Teller frame ensures that the plasma velocity and magnetic field are in the same direction on both sides of the shock.

gyrating particle encountering the magnetic gradient caused by the shock, resulting in a guide center drift and an energy gain due to the presence of a convective electric field at the shock.

There are two important frames of reference through which SDA is studied. In the rest frame of the shock, known as the 'normal incidence frame' (NIF), the upstream plasma has velocity $\mathbf{u}_1$ along the normal $\hat{n}$ to the shock front. The upstream magnetic field $\mathbf{B}_1$ creates an angle θ_{Bn} with the shock normal $\hat{n}$, and the downstream counterparts have values $\mathbf{u}_2$ and $\mathbf{B}_2$, Figure 2.7(left).

Due to the motion of the plasma across the magnetic field, there is a convective electric field given by $\mathbf{E} = \mathbf{v} \times \mathbf{B}$, which causes a drift of the particles with speed $\mathbf{v}_E = \mathbf{E} \times \mathbf{B}/B^2$. The kinematics of the particle in the shock drift acceleration mechanism are best treated in a frame where there the convective electric field vanishes such that $\mathbf{E} = |\mathbf{v} \times \mathbf{B}| = v_x B_y - v_y B_x = 0$. The frame where this criterion is fulfilled is known as the de Hoffmann-Teller frame (dHTf) and has a frame velocity with respect to the NIF frame given by.

$$v_{HT} = v_y = u_1 \tan\theta_{Bn} \tag{2.39}$$

This frame guarantees the plasma motion is in the same direction as the magnetic field on both sides of the shock. Given the absence of any electric fields in this frame, the particle motions may be treated as having a conserved magnetic moment

$$\mu = \frac{mv_{1\perp}^2}{B_1} = \frac{mv_{2\perp}^2}{B_2} = \text{const} \tag{2.40}$$

where the subscripts [1,2] represent pre an post-encounter shock values respectively. In the dHTf, the conservation of the magnetic moment may be used to derive the particle kinematics given either reflection or transmission though the shock. Rearrangement of equation shows that particles with a pitch angle fulfilling the relationship

$$\alpha > \alpha_c \quad \text{where} \quad \sin^2\alpha_c = \frac{B_1}{B_2} \tag{2.41}$$

will be reflected at the shock. This pitch angle α_c defines a 'loss-cone' in velocity space $f(v_\perp, v_{||})$, whereby any particle within the cone (large $v_{||}$) will be lost downstream, while particles outside the loss cone will be reflected at the shock. This is known as a 'magnetic mirroring', a process that shocks are known to exhibit (Feldman *et al.*, 1983). Inside the dHT reference frame, the particles energy (whether reflected or transmitted) is completely conserved and there is no energy gain. Conceptually, the best way to see where the acceleration takes place is in the normal indicidence frame (NIF).

In the NIF, the particles gyrate about the upstream magnetic field $\mathbf{B}_1$, while

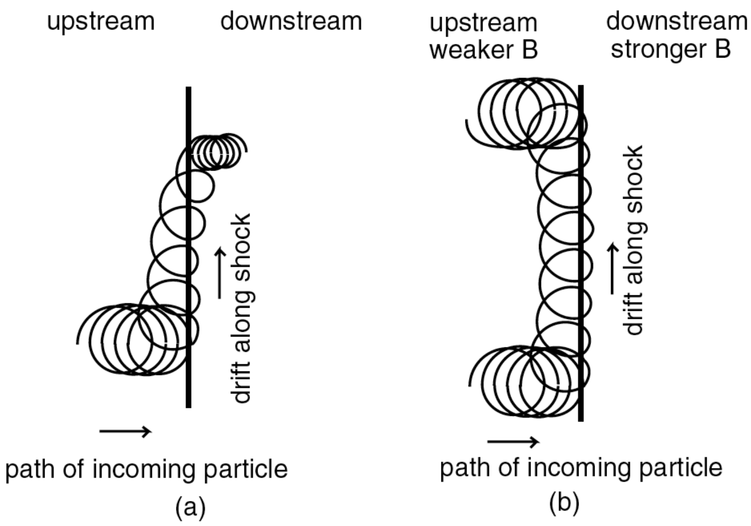

Figure 2.8: Particle drift paths due during both a transmitted (a) and reflected (b) motion. The increased magnetic field in the downstream region caused a drift along the surface. This drift occurs in the presence of a convective electric field (which will have a component parallel to the drift), allowing the field to do work on the particle and hence increase its energy.

there is a convective electric causes a small drift of magnitude $\mathbf{v}_E = \mathbf{E} \times \mathbf{B}/B^2$ towards the shock. If the particle speed is much greater than the shock speed $v >> u$, the particle undergoes many Larmor gyrations while in contact with the shock. The difference between the Larmor radius of the orbit ahead of and behind the shock front (due to the increased downstream magnetic field) will cause the particle to drift parallel to the shock surface, Figure 2.8. This is equivalent to a 'grad-B' drift in an inhomogeneous magnetic field. This drift allows a charged particle to move parallel to the convective electric field, allowing the E-field to do positive work on the particle and produce an energy increase. Overall, a grad-B drift at the shock surface gives the particle a component of velocity that may interact with the convective electric field, hence the process is known as 'drift-acceleration'.

While the energy gain is most apparent in the NIF frame, particle reflection and transmission is best handled mathematically in the dHT frame. Hence firstly, the magnetic mirroring process is described in dHT, while the post-encounter speed and energy gain are then obtained by converting back to the rest frame of the upstream plasma (NIF). Reference has shown that the particle energy gain upon reflection from the shock is given by

$$\frac{E_r}{E_i} = \frac{1+\sqrt{1-B_1/B_2}}{1-\sqrt{1-B_1/B_2}} \tag{2.42}$$

The energy gain is limited to the magnetic field strength jump across the shock, and since this field strength is limited by equation 2.38, the energy gain is limited to a factor of 13.93. A similar treatment may also give the reflected velocity in terms of the incident velocity.

$$v_{||}^{r} = 2u_1 \mathrm{sec}\theta_1 - v_{||}^{i} \tag{2.43}$$

shock drift acceleration has been used to explain the presence of $1-100\,\mathrm{keV}$ electron at Earth's magnetospheric bow shock (Wu, 1984), in the context of radio bursts have used it to explain the acceleration of electrons during type II and herringbone bursts (Holman & Pesses, 1983; Mann & Klassen, 2005; Schmidt & Cairns, 2012b) More sophisticated models involve multiple reflections at the shock that increase the energy gain each time, thereby producing energies that are observed in the vicinity of shocks. This multiple reflection process plays an important role in some theoretical treatments of herringbone emission; we will return to this point in Chapter 5.

2.3.4 Wave-Particle Interaction

The treatment of the interaction of particles and waves in a plasma is in determining what the oscillatory response of a plasma is to a velocity distribution function (Inan & Golkowski, 2011). In order to see how the distribution function effects wave growth we start with an equilibrium distribution f_0 and impose a perturbation $f_1(\mathbf{r}, \mathbf{v}, t)$, so that the total distribution function is $f(\mathbf{r}, \mathbf{v}, t) = f_0 + f_1(\mathbf{r}, \mathbf{v}, t)$. The perturbation quantities will take the form $e^{i(\omega t + \mathbf{k}r)}$ i.e., perturbation quantities that are periodic in space and time with eave number $\mathbf{k}$ and angular frequency ω.

To see how $f(\mathbf{r}, \mathbf{v}, t)$ evolves in time we insert it into the Vlasov equation and linearize, ignoring any terms higher than second order

$$\frac{\partial f_1}{\partial t} + (\mathbf{v} \cdot \nabla) f_1 + \frac{q_e}{m_e}(\mathbf{E} + \mathbf{v} \times \mathbf{B}) \cdot \nabla_v f_0 = 0 \tag{2.44}$$

Assuming an isotropic f_0 then $(\mathbf{v} \times \mathbf{B}) \cdot \nabla_v f_0 = 0$. Then using Poisson's equation (Maxwell 1) and noting that the perturbation solutions are oscillatory, the perturbed Vlasov equation may be rearranged to give

$$f_1 = \frac{q_e}{m_e} \frac{j}{\omega - \mathbf{k} \cdot \mathbf{v}} \mathbf{E} \cdot \nabla_v f_0 \tag{2.45}$$

This equation relates the perturbed quantity f_1 to the unperturbed distribution function and the electric field. The most important aspect of this equation is the $\omega - \mathbf{k} \cdot \mathbf{v}$ term in the denominator, implying the possibility of resonance. Now, integrating both sides of 2.45 over all velocity space and again using Poisson's equation results in

$$1 + \frac{q_e}{\epsilon_0 m_e} \frac{1}{k^2} \mathbf{k} \cdot \int_v \frac{\nabla_v f_0}{\omega - \mathbf{k} \cdot \mathbf{v}} d^3 v = 0 \tag{2.46}$$

Any electrostatic normal mode oscillations satisfy this relationship and integrating over all space will result in a dispersion relation for the oscillations of the plasma property f_1. The equation effectively tells how oscillations and velocity distributions interact in a plasma. However, as mentioned, there is the possibility of resonances in this equation and the integral is non-trivial at $v \rightarrow \frac{\omega}{k}$ i.e., there is a singularity at the point $v = \frac{\omega}{k}$. If there are electrons in the particle distribution function that match the phase speed of oscillations in the plasma then the integral become non-trivial with a singularity or 'pole'. To avoid the singularity producing unphysical results, the integration is performed in complex space using a method called contour integration (Melrose, 1989). The use of contour integration means there will be complex solutions of the dispersion relation of the form $\omega = \omega_r + i\gamma$. The real part of the solution applies as normal where the integral is well behaved, far from the singularity. However, integration over the singularity necessitates a complex solution (from the contour integration), hence the ω consists of both real and imaginary parts. The complex $i\gamma$ means that a time dependency of the periodic solutions to the perturbations f_1 will be

$$e^{j\omega t} = e^{(i[\omega_r + i\gamma])} = e^{i\omega_r t} e^{-\gamma t} \tag{2.47}$$

This solution is a damped wave with damping factor γ, meaning the solutions to (equation!!!) in the region $v \sim \omega/k$ provides a wave decay term. These are the essential elements of Landau damping e.g., if the phase speed of the waves in a plasma match the speed of electrons in the distribution function then those waves will experience a damping. However, the damping term is dependent on the negative of the velocity space gradient at $v = \frac{\omega}{k}$ (Melrose, 1989)

$$\gamma \sim -\nabla_v f_0|_{v=\frac{\omega}{k}} \tag{2.48}$$

If there are a group of electrons that have the same speed of a particular wave in the plasma they may exchange energy with this wave efficiently. If there is a negative gradient on the velocity distribution at $v = \frac{\omega}{k}$, this will lead to wave damping. However, a positive gradient in the velocity distribution will result in $\gamma < 0$ and a wave growth term that increases exponentially. Effectively, a group of electrons is promoted to a velocity range that closely matches the phase speed of some type of waves in a medium $v \sim \omega/k$. In such a speed range the integrand of (equation) approaches the point at which there is a singularity in the solution. Such a point necessitates a complex solution to the integral, thus providing an imaginary part to the dispersion relation that gives an $e^{-\gamma t}$ term. If the promotion of electrons to a range $v \sim \omega/k$ is combined with a positive gradient of the distribution function in this velocity range, it results in $\gamma < 0$ and $e^{-\gamma t} > 0$, leading to wave growth. This is why $v - \omega/k = 0$ is known as the resonance condition (Melrose, 1989). Since electron beams in the corona match the phase speed of Langmuir waves, the beam results in the generation of Langmuir waves. This group of electrons in the beam is called a bump-on-tail, since it is described by a Gaussian bump on the high velocity tail of a Maxwell distribution function. The growth of Langmuir waves in a resonant response to this beam is called the bump-on-tail instability. Once these Langmuir waves are generated they may undergo decay or coalescence with other waves to produce electromagnetic radiation.

2.3.5 Three-Wave Interaction and Plasma Emission

Once the Langmuir waves are produced from the bump-on-tail instability a number of wave interaction processes occur in order to bring about plasma emission. This involves the interaction of various wave modes in the plasma described by a mathematical formalism called the three-wave interaction (Robinson *et al.*, 1993, 1994). In this process three wave modes in a plasma M, P, and Q are described by their distribution functions in a wave-number space (k-space). the distribution functions are given by $N_M(k_M)$, $N_P(k_P)$, $N_Q(k_Q)$, where the N describe the occupation number of wave quanta between k and $k + dk$ in the wave-number space. Waves in P and Q mode may interact to such that wave quanta are removed from the P and Q k-space and added to the M k-space. This is essentially an emission of an energy packet from the P and Q -space to the M k-space. The rate of change of occupation numbers in the three k-spaces are given by

$$\frac{dN_M(\mathbf{k}_M)}{dt} = -\int \frac{d^3\mathbf{k}_P}{(2\pi)^3} \int \frac{d^3\mathbf{k}_Q}{(2\pi)^3} g(\mathbf{k}_M, \mathbf{k}_P, \mathbf{k}_Q) \tag{2.49}$$

$$\frac{dN_P(\mathbf{k}_P)}{dt} = -\int \frac{d^3\mathbf{k}_M}{(2\pi)^3} \int \frac{d^3\mathbf{k}_Q}{(2\pi)^3} g(\mathbf{k}_M, \mathbf{k}_P, \mathbf{k}_Q) \tag{2.50}$$

$$\frac{dN_Q(\mathbf{k}_Q)}{dt} = -\int \frac{d^3\mathbf{k}_M}{(2\pi)^3} \int \frac{d^3\mathbf{k}_P}{(2\pi)^3} g(\mathbf{k}_M, \mathbf{k}_P, \mathbf{k}_Q) \tag{2.51}$$

where $g(\mathbf{k_M}, \mathbf{k_P}, \mathbf{k_Q})$ is an expression that incorporates a transition probability for wave quanta into and out of energy states in the various k-spaces (Robinson *et al.*, 1994). The transition probability of waves amongst states M, P and Q is given by (Melrose, 1986)

$$u_{MPQ}(\mathbf{k}_M, \mathbf{k}_P, \mathbf{k}_Q) \propto \delta(\omega_M - \omega_P - \omega_Q)\delta^3(\mathbf{k}_M - \mathbf{k}_P - \mathbf{k}_Q) \tag{2.52}$$

where the ω are the frequency of the corresponding wave and and δ are delta functions. This is analogous to transition probabilities given by the Einstein coefficients for transferring energy packets from and atomic state to a photon state (photon emission) i.e., whereas the Einstein coefficients are used in atom-wave (atom-photon) energy exchanges, u_{MPQ} describes wave-wave energy exchanges. Given the presence of delta functions in the transition probability expression, we can see that an exchange of energy quanta amongst the wave modes can only occur when

$$\omega_M = \omega_P + \omega_Q \tag{2.53}$$

$$\mathbf{k}_M = \mathbf{k}_P + \mathbf{k}_Q \tag{2.54}$$

Hence for an a conversion wave modes in a plasma such as $M \rightarrow P + Q$ (a decay of mode M into P and Q), or it's reverse process $P + Q \rightarrow M$ (a coupling of P and Q to produce M) is described by equations (2.1) to (2.7).

The production of plasma emission after a bump-on-tail instability has occurred requires a three wave interaction amongst a Langmuir wave L, ion acoustic wave S, and electromagnetic wave T. Fundamental emission during a radio burst occurs via a decay of Langmuir waves into an electromagnetic and ion sound wave

$$L \rightarrow T + S \tag{2.55}$$

while second harmonic first requires the decay $L \rightarrow L^{'} + S$, where $L^{'}$ is a product Langmuir wave propagating in the opposite direction to the first. This is followed by a coalescence of the original and product Langmuir waves

$$L + L^{'} \rightarrow T' \tag{2.56}$$

In the case of these three interacting waves then

$$\omega_T = \omega_L + \omega_S \quad (2.57)$$

$$\omega_{T'} = \omega_L + \omega_{L'} \quad (2.58)$$

where the relevant dispersion relations are

$$\omega_L = \omega_p + \frac{3V^2}{2\omega_p}k_L^2 \quad (2.59)$$

$$\omega_T = (\omega_p^2 + k_T^2c^2)^{1/2} \quad (2.60)$$

$$\omega_S = k_s\sqrt{\frac{\gamma k_B T_e}{m_i}} \quad (2.61)$$

where

$$\omega_p = \left(\frac{n_e e^2}{m_e \epsilon_0}\right)^{\frac{1}{2}} \quad (2.62)$$

In order to investigate the amount of energy emitted by the electromagnetic wave, elements of the three wave interaction theory need to be combined with what is known as stochastic growth theory (Robinson & Cairns, 1993)(SGT). Stochastic growth theory was first developed in response to a number of criticisms of the theory of a beam-driven Langmuir wave hypothesis of type III radio bursts first proposed by Ginzburg & Zhelezniakov (1958). It was pointed out that if the beam was to remain in instability continuously over space and time in the absence of saturation mechanism, then it would quickly lose all of its energy to the Langmuir waves and consequently the beam electrons would stop propagating after a short distance (Sturrock, 1964). This is clearly not the case, since type III electrons are observed to propagate over distances of 1 A.U or more. SGT overcomes this by describing an electron beam propagation in a state of marginal stability. The beam propagates in an inhomogeneous medium whereby it encounters pockets of localised density enhancement where it is unstable intermittently. As the beam propagates through this localised clump, it is unstable to the growth of Langmuir wave, giving up some of its energy to the wave, diminishing the beam slightly. Once it exits the clump it becomes stable again, allowing the beam to reform until it reaches another localised clump to give up some energy again. The Langmuir waves would then experience a growth at intermittent regions in space and time (which is actually observed (Lin *et al.*, 1986)), while the beam would be unstable for only small fractions of its lifetime. Overall, the beam energy loss is on average low enough to allow its continued propagation, but instantaneous and finite enough to allow the growth of waves. Combining elements of the stochastic growth model and the three-wave interaction process allows a calculation of the mount of energy that ends up in the electromagnetic waves, and consequently the volume emissivity of the emission (Robinson & Cairns, 1993, 1998)

$$j_M(r) \approx \frac{\Phi_M}{\Delta\Omega_M} \frac{n_b m_e v_b^3}{3l(r)} \frac{\Delta v_b}{v_b} \tag{2.63}$$

here the M stands for either fundamental F or harmonic H emission. $\Delta\Omega_M$ is the solid angle over which the emission is spread, n_b is the electron beam number density, v_b is the beam speed, $l(r)$ is the distance from emission point to observer, Δv_b is the width of the beam in velocity space. Φ_M are known as the conversion efficiencies and are different for fundamental and harmonic emission, see Appendix X. These expressions have been used to simulate radio burst flux resulting in $\sim 10^{-17}\,\mathrm{W\,m^{-2}\,Hz^{-1}}$, which have been compared to type II and III radio bursts (Knock *et al.*, 2001; Schmidt & Cairns, 2012a). Knock *et al.* (2003) and Cairns *et al.* (2003) used the theory to predict interplanetary type II burst flux as a function of a variety of shock parameters e.g., shocks speed Fig. 2.9.

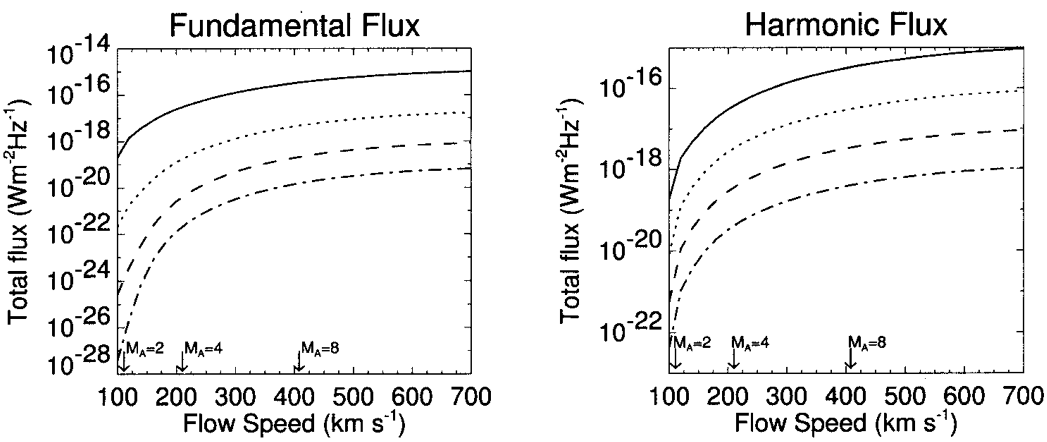

Figure 2.9: Theoretical flux of the fundamental and harmonic emission bands of a type II radio burst using three wave interaction and stochastic growth theory Cairns *et al.* (2003).

2.3.6 Frequency Drift of Radio Bursts

In the previous section it was shown that when plasma emission is excited in the corona, the frequency of emission is close to the plasma oscillation frequency given by equation 2.62 As the exciter of the plasma emission moves to greater heights in the corona it will produce plasma emission at continually decreasing frequency due to the dropping density. For example a typical signature of a coronal shock wave in dynamic spectra is two narrow emission lanes (at f_{plasma} and $2f_{plasma}$) drifting toward lower frequency as time passes. A type III radio burst is excited by a much faster source, hence its frequency drift is much faster in dynamic spectra. Generally different types of radio burst have different morphologies when viewed in dynamic spectra owing to their movement (or lack of movement) into regions of different density in the corona. A summary of the burst types is given in Figure 2.10

Generally, the frequency drift of the radio burst depends on the velocity of the exciter and the density variation in the corona. It is possible to estimate the speed of the exciter from a set of frequency time values (f_i, t_i). Such as set of values are

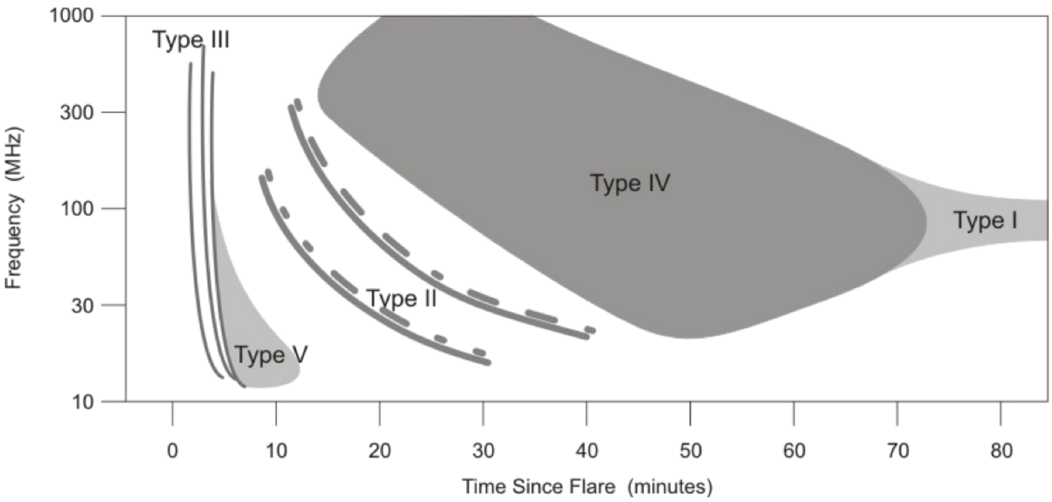

Figure 2.10: The characteristic shapes of various solar radio bursts seen in dynamic spectra. Type II radio burst are a signature of shock transit from high number density into low number density, as indicated by their drift from high to low frequency. The presence of two distinct bands is indicative of radio emission at the plasma frequency (fundamental) and its second harmonic. These two bands may also be further split themselves, a feature known as band-splitting.

a direct diagnostic of the number density of the environment of emission versus time e.g., using $f \approx 9000\sqrt{n_e}$, frequency versus time gives number density versus time, $(f_i, t_i) \rightarrow (n_i, t_i)$. Now, in general the number density of the corona is inversely proportional to height, varying according to some exponential decrease. A very simple model is the hydrostatic case $n(r) = n_0\exp(-r/H)$ where r is distance from sun center, and H is the scale height given by $H = kT/mg$, where k is Boltzman's constant, T is the coronal temperature, m is proton mass and g is gravity. Generally using this $n(r)$, the set of values (n_i, t_i) can be converted to as set of (r_i, t_i)

$$(f_i, t_i) \rightarrow (n_i, t_i) \rightarrow n(r) \rightarrow (r_i, t_i). \tag{2.64}$$

Hence, by some appropriate choice of coronal density model $n(r)$, a set of frequency and time values may be converted to a set of height vs time values, from which the velocity may be derived. Common practice is to use an $n(r)$ that is

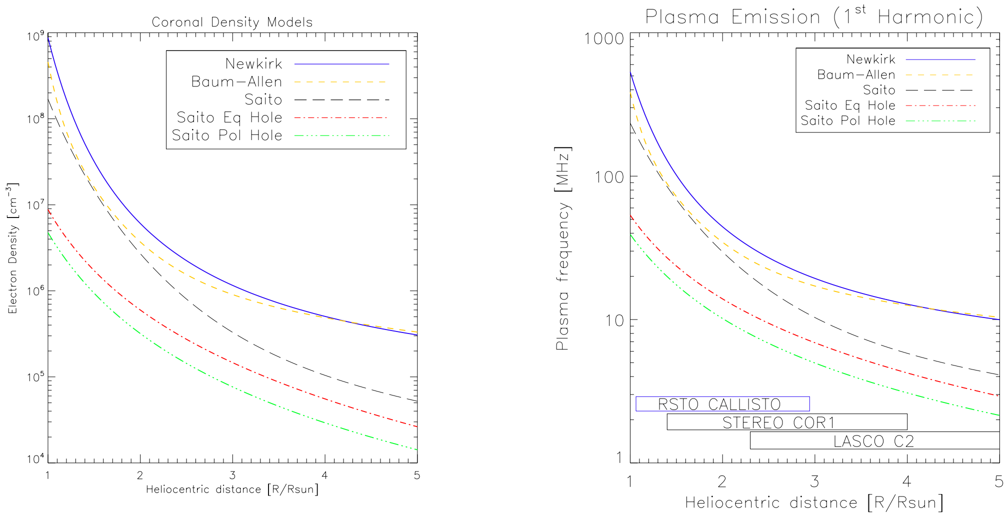

Figure 2.11: (Left) Electron number density as a function of height as defined by each of the models listed. The Newkirk, Baumbach Allen, and Saito models each describe an equatorial quiet corona electron density profile. The Saito Eq Hole and Pol Hol describe equatorial and polar hole profiles, respectively. These models are generally used to specify the height of a radio burst in the corona, and the choice of model is often arbitrary. (Right) The first harmonic of the plasma frequency as a function of height defined by the models.

derived semi-empirically. For example, there exists a set of models that describe the density fall off with height of the equatorial quiet corona, coronal holes, and active regions Allen (1947); **?**); **?**, shown in Figure 2.11. The choice of model affects both the resulting height of the radio emission and the derived speed. A much better diagnostic of radio bursts would be to use actual density measurements of the corona in places of these models, but this is generally not usual practice.

3

Observation and Instrumentation

3.1 Thompson Scattering Theory

3.1.1 Thomson Scattering in the Corona

The first evidence for the existence of the corona was through observations during solar eclipses. The occultation of the solar disk by the moon revealed a visible outer atmosphere structured into streamers and plumes and extending far from the solar surface (Fig. ??). This is known as the white-light corona and is due to Thomson scattering of photospheric light by free electrons in the corona.

Figure 3.1: The white-light corona during a solar eclipse. Occultation of the bright solar disk by the moon reveals the faint outer atmosphere of the Sun, known as the corona. It is highly structured, showing features like streamers and plumes. *Eclipse photograph courtesy of Miloslav Druckmüller http://www.zam.fme.vutbr.cz*

The tangential component (I_T), radial component (I_R), and polarization (I_P) of the scattered intensity are given by the expressions

$$I_T = I_0 \frac{\pi \sigma_e}{2z^2}[(1-u)C + uD] \tag{3.1}$$

$$I_P = I_0 \frac{\pi \sigma_e}{2z^2} \sin^2 \chi [(1-u)A + uB] \tag{3.2}$$

with $I_R = I_T - I_P$. A, B, C, and D are the van de Hulst coefficients and are a trigonometric function only of the solid angle subtended by the Sun at the scattering point (see Appendix). I_0 is incident intensity, σ_e is the electron scattering cross section, z is the distance from scatterer to observer, u is a limb darkening coefficient, and χ is the angle between a radial vector from sun centre to the scattering electron and a position vector from observer to the electron.

The total scattered intensity is given by

$$I_{tot} = 2I_T - I_p \sim I_0 \frac{\pi\sigma_e}{z^2}\left(1 - \frac{\sin^2\chi}{2}\right) \tag{3.3}$$

The van de Hulst coefficients are solutions of a set of integrals to obtain the brightness of each component of the radiation scattered by a single electron in the solar corona. They are a result of scattering theory applied to the case of an electron receiving radiation from the entire solar disk, as opposed to a simpler point source of incident radiation. They are as follows

$$A = \cos\Omega \sin^2\Omega \tag{a}$$

$$B = -\frac{1}{8}\left[1 - 3\sin^2\Omega - \frac{\cos^2\Omega}{\sin\Omega}(1 + 3\sin^2\Omega)\ln\left(\frac{1 + sin\Omega}{\cos\Omega}\right)\right] \tag{b}$$

$$C = \frac{4}{3} - \cos\Omega - \frac{\cos^3\Omega}{3} \tag{c}$$

$$D = \frac{1}{8}\left[5 + \sin^2\Omega - \frac{\cos^2\Omega}{\sin\Omega}(5 - \sin^2\Omega)\ln\left(\frac{1 + \sin\Omega}{\cos\Omega}\right)\right] \tag{d}$$

where Ω is the angle between the lines QS and QT. Q is the scattering point, S is Sun center, and T is the point where the scattered point vector crosses the Sun at a tangent (Howard & Tappin, 2009a).

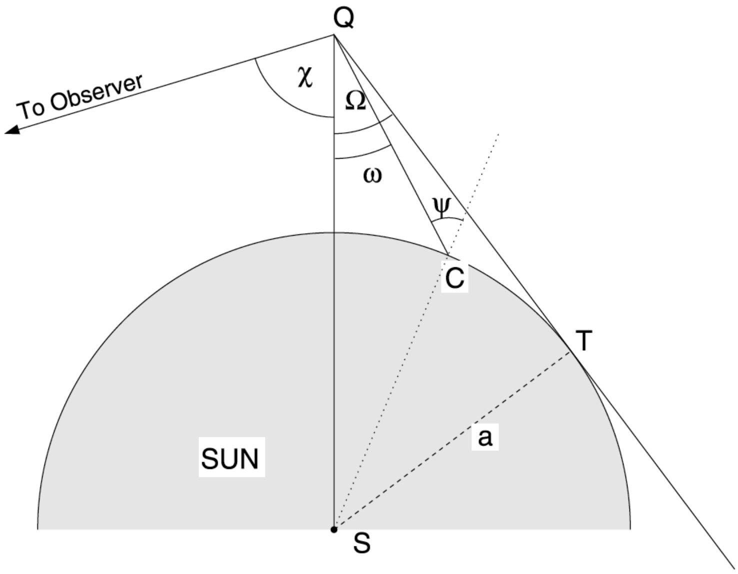

Figure 3.2: Geometry of single electron scattering in the solar atmosphere, with angles Ω and χ.

3.1.2 White-light observations of CMEs

3.2 Coronagraphs

Before the early 20th century the only way to view the corona was for a short period during a solar eclipse when the moon blocks direct photospheric light. Under normal conditions direct sunlight overwhelms the faint corona. In 1939 the French Astronomer Bernard Lyot developed a telescope, known as a coronagraph, which allowed observation of the corona at any time (Lyot, 1939). A coronagraph is an optical system that provides an artificial eclipse of direct photospheric light so the much fainter corona can be imaged.

3.2.1 Lyot Coronagraph

The Lyot Coronagraph is the name given to the first optical design of a coronagraph developed by Bernard Lyot. A basic schematic of the instrument is given in Figure 3.3. The optical element O1 is a lens that is extremely polished to prevent scattering and reflections of incident light. O1 creates an image of the Sun onto its focal plane at F1 where the occulting disk, D1, reflects away the unwanted solar disk image. F1 then images the objective lens and the occulting disk onto the plane of O2. Lyot's key invention was the Lyot stop and Lyot spot. These are devices onto which light diffracted at the occulting disk is directed and subsequently blocked from being imaged by the final lens O2. O2 then images the faint corona and occulting disk onto the detector plane.

The Lyot coronagraph is described as internally occulting due to the placement of the occulting disk behind the first objective lens. This is to distinguish it from a externally occulted system in which the disk is placed in front of the objective lens. Modern coronagraphs follow the same basic design of Lyot's but contain extra features such as baffles to stop any scattered light in the telescope.

3.2.2 STEREO COR1 and COR2

The *Solar Terrestrial Relations Observatory* (*STEREO*; Kaiser *et al.*, 2008) Ahead and Behind are two nearly identical spacecraft traveling ahead and behind Earth in its orbit. Each spacecraft is receding from Earth at a rate of $\pm 22^{\circ}$ per year, such that they are effectively traveling around the Sun in opposite directions. They carry an identical set of instruments known as the Sun Earth Coronal Connection and Heliospheric Investigation (SECCHI) suite, including in situ detectors and a variety of imagers. On each spacecraft there are two coronagraphs, COR1 and

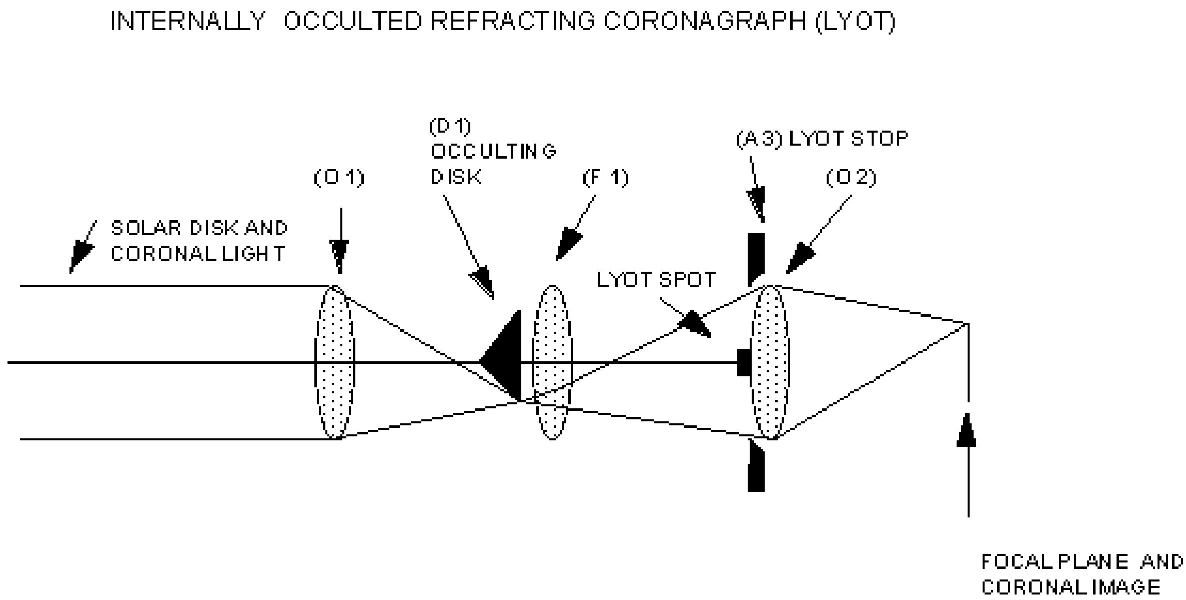

Figure 3.3: A schematic of the basic optical design of the Lyot coronagraph. Lyot's key inventions where the placement of a Lyot stop and Lyot spot at the positions where diffracted light would contaminate the image and obscure the faint corona.

COR2 (Howard *et al.*, 2008). The Ahead COR1 and COR2 combined with Behind COR1 and COR2 offer a stereoscopic view of the corona and any transient event taking place, such as a CME.

COR1 is an internally occulted Lyot coronagraph, see Figure 3.4. It images the inner corona with a field of view from $1.4 - 4.5\,R_\odot$ in a waveband 22.5 nm wide centered on the Hα line at 656 nm. It has an internal polarizer that takes three images at 0°, 120°, and 240°, so that polarized or total brightness images of the inner corona may be produced. It nominally produces 1024×1024 pixel images with platescale of 3.75 arcsec per pixel (Thompson & Reginald, 2008). A typical observing sequence will give an image cadence of 10 minutes.

COR2 is an externally occulted Lyot coronagraph. Externally occulted coronagraphs have an extra occulting disk in front of the objective lens, see Figure 3.5. This is to prevent direct sunlight scattering off of the objective lens, making internally scattered light less of a problem for this type of coronagraph. A downside to this design is that the external occulter does not allow the inner corona to be imaged, hence such coronagraphs are usually used to observe the extended corona to larger heights. COR2 observes the corona in a field of view from $2.5 - 15\,R_{\odot}$ and in a wavelength range of $650 - 750$ nm. It nominally produces 2048×2048 images, with 14.7 arsec per pixel. Like COR1 it has an internal polarizer producing three linearly polarized images per observing sequence (30 minutes).

These white light imagers of the corona allow for a stereoscopic view of CMEs in a total field of view covering $1.4 - 15\,R_{\odot}$. The two viewpoint capabilities of these telescopes offer a more accurate observational estimation of both CME kinematics and CME mass, resulting in a better understanding of CME dynamics.

3.2.3 SOHO LASCO

3.3 Radio Spectrometers and Radioheliographs

3.3.1 RSTO Callisto

3.3.2 STEREO WAVES

3.3.3 Nancay Decametric Array

3.3.4 Nancay Radioheliograph

3.4 EUV imaging

3.4.1 SDO AIA

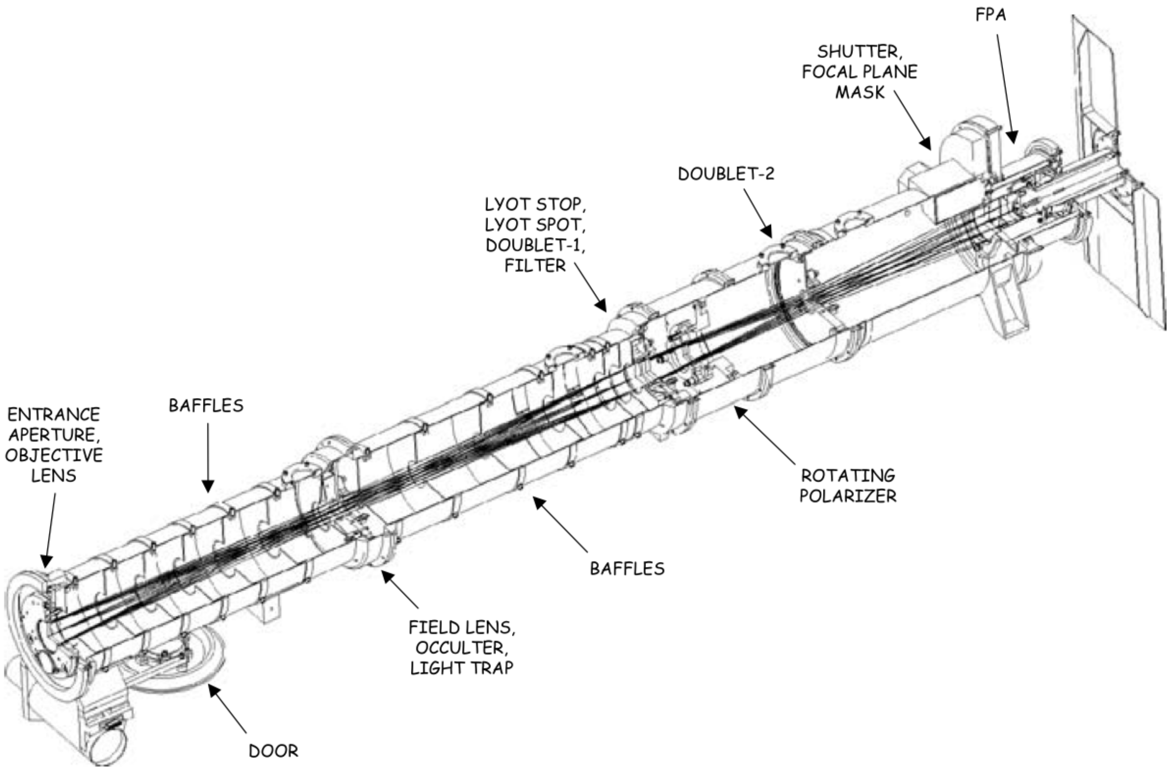

Figure 3.4: A schematic of the basic optical design of the the COR1 coronagraph. There are two such identical instruments, one on the Ahead and one on the Behind spacecraft. It is the same basic design as the Lyot coronagraph with the addition of baffles to prevent scattered light and a polarizer behind the Lyot stop (Thompson & Reginald, 2008).

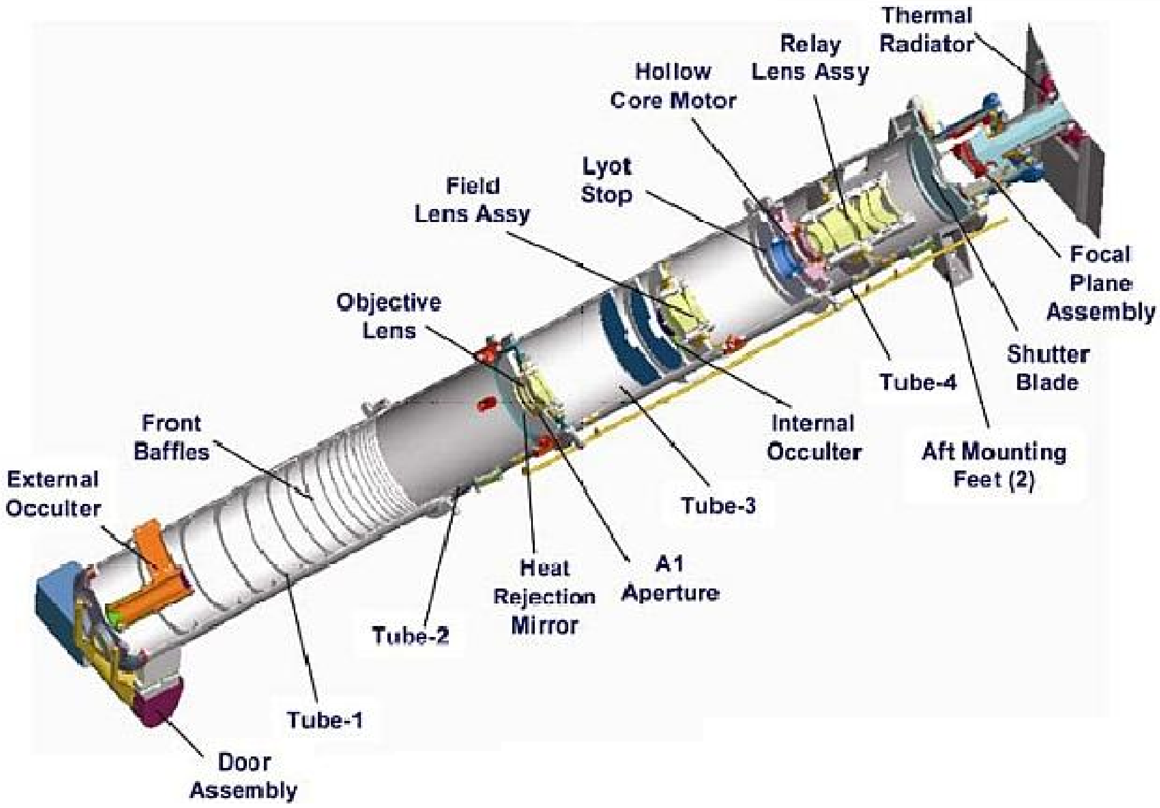

Figure 3.5: A schematic of the basic optical design of the COR2 coronagraph. This is an externally occulted coronagraph, meaning it has an extra occultation disk in front of the objective lens. This results in less internally scattered light, but also results in an obscuration of the inner corona. As with COR1, there are two such identical instruments, one on the Ahead and one on the Behind spacecraft (Howard *et al.*, 2008).

4

Coronal Mass Ejection Masses, Energetics, and Dynamics

4.1 Masses

Despite many years of study, the origin of the forces that drive coronal mass ejections (CMEs) in the solar corona and interplanetary space are not well understood. From an observational viewpoint a complete understanding of CME kinematics, dynamics and forces requires not only a study of CME speed, acceleration and expansion but also an accurate knowledge of CME mass. The measurements of CME mass combined with acceleration measurements can be used to quantify the magnitude of the force that drives a CME. Knowledge of this force magnitude can lead to an identification of the possible origin of the CME driver.

There are numerous theoretical models that attempt to explain the triggering of CME eruption and its consequent propagation. Each describe the destabilization and propagation of a complex magnetic structure, such as a flux rope, via mechanisms that include the catastrophe model (Forbes & Isenberg, 1991; Forbes & Priest, 1995; Lin & Forbes, 2000), magnetic breakout model (Antiochos *et al.*, 1999b; Lynch *et al.*, 2008), or a toroidal instability model (Chen, 1996; Kliem & Török, 2006). The loss of equilibrium induced by such mechanisms results in CME propagation into interplanetary space. The predictions of these models have been investigated in observational studies whereby the CME kinematics are used to constrain what forces might be at play and hence which model best describes CME propagation. Such studies show that early phase propagation can be reasonably described by the existing models (or a combination of them) involving some form of magnetic CME driver (Chen *et al.*, 2006; Lin *et al.*, 2010; Manoharan & Kundu, 2003; **?**), and that aerodynamic drag of the solar wind may have a significant role at later stages of CME propagation (Howard *et al.*, 2007; Maloney & Gallagher, 2010; **?**). Comparisons between modeling and observational estimates of the forces that drive CMEs requires an accurate determination of CME kinematics properties as well as CME mass.

To date, the most prevalent method of determining CME mass has been through the use of white light coronagraph imagers, such as the Large Angle Spectroscopic Coronagraph (LASCO; Brueckner *et al.*, 1995) on board the *So-*

lar and Heliospheric Observatory (*SOHO*; Domingo *et al.*, 1995) and the twin Sun Earth Connection Coronal and Heliospheric Investigation (SECCHI) COR1 and COR2 coronagraphs (Howard *et al.*, 2008) on board the *Solar Terrestrial Relations Observatory* (*STEREO*; Kaiser *et al.*, 2008). The white-light emission imaged by such coronagraphs occurs via Thomson scattering of photospheric light by coronal electrons (Billings, 1966; Minnaert, 1930; van de Hulst, 1950), the so called K-corona. From classical Thomson scattering theory, the intensity of the light detected by an observer depends on the particle density of the scattering plasma. Hence, any density enhancement, such as a CME, over the background coronal density appears as enhanced emission in white light. The enhanced emission allows for a calculation of the total electron content and hence mass.

Some of the first measurement of CME mass using scattering theory were carried out by Munro *et al.* (1979) and Poland *et al.* (1981) using space-based white light coronagraphs on board *SkyLab* and U.S. military satellite *P78-1*. Both the early studies and later statistical investigations determined that the majority of CMEs have masses in the range of 10^{13}–10^{16} g, (Vourlidas *et al.*, 2002, 2010). However, due to only a single viewpoint of observation, the longitudinal angle at which the CME propagates outwards was largely unknown in these studies and it is generally assumed that the CME propagates perpendicular to the observers line-of-sight (LOS). There is also the added assumption that all CME mass lies in the two-dimensional plane-of-sky (POS). Such assumptions can lead to a mass underestimation of up to 50% or more (Vourlidas *et al.*, 2000). More recent studies have employed the two viewpoint capabilities of the *STEREO* mission to determine the mass of numerous CMEs with much less uncertainty (Colaninno & Vourlidas, 2009).

In this paper, we analyze mass development of the 2008 December 12 CME using the *STEREO* COR1 and COR2 coronagraphs.We use a well constrained angle of propagation to determine the mass and position of the CME. Combining the mass measurements with values for CME velocity and acceleration, the kinetic energy and the magnitude of the force influencing propagation is determined for each point in time. Section 2 describes the observations of the event from first appearance of the front in COR1 A and B to the time when the front exits the COR2 A and B fields of view. Section 3 describes the methods by which the mass, energy, and force are calculated with *a priori* knowledge of the propagation angle. Section 4 includes the results and Section 5 discusses the possible forces attributable to the observed accelerations and whether they are magnetic or aerodynamic in origin. This is followed by conclusions in Section 6.

4.1.1 Observations

The COR1 images used in this analysis span from 2008 December 12 04:05 UT to 15:45 UT, with a cadence of 10 minutes. The three polarization states of COR1 were combined to make total brightness images in units of mean solar brightness (MSB). Base difference images were produced using the 04:05 UT image (in both COR1 A and B) as a background to be subtracted from all subsequent images. A sample of such images for both COR1 A and B can be found in Figure 4.1. The COR2 images analyzed range from from 07:22 UT to 17:52 UT, with a cadence of 30 minutes. As with the COR1 images, total brightness images were created for COR2, and a set of base difference images were then produced using the 07:22 UT image as a suitable background. A selected set of images from COR2 can be found in Figure 4.2.

At 04:35 UT the leading edge of a CME appeared in COR1 A and B coronagraphs at a height of $\sim$1.4 $R_\odot$, off the east and west limb respectively. In

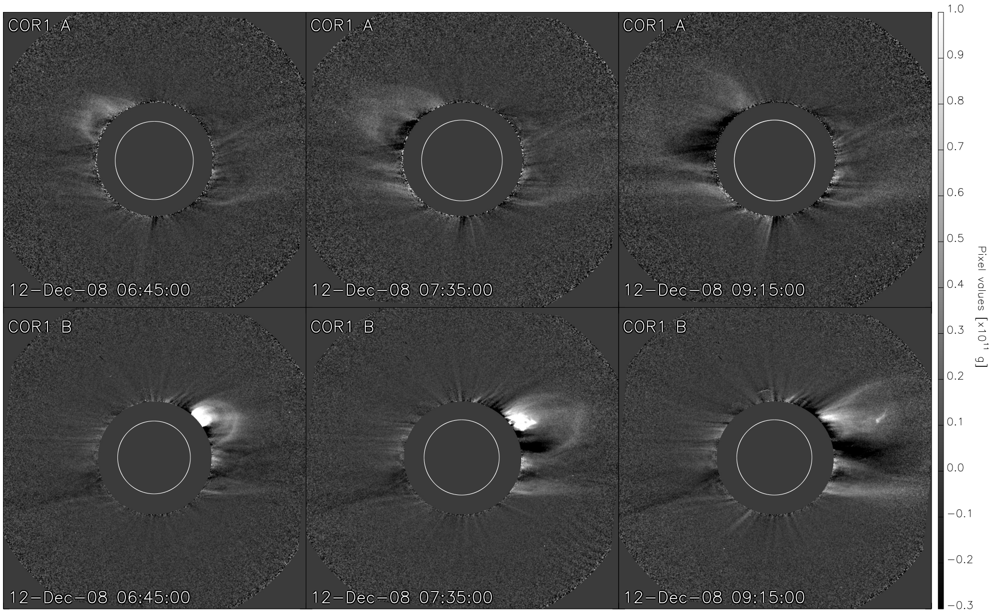

Figure 4.1: Selection of base difference images of the CME in COR1 A (top row) and COR1 B (bottom row), with pixel values of grams. The CME is quite faint in the A images and appears not to have as much structure as in B. There is a large contribution to mass from a near-saturated region to the upper flank of the CME in the B images. Such saturation in the mass images coincides spatially with the prominence in total brightness images.

COR1 B the CME first appears as a set of rising loop-like structures followed by a prominence, part of which appears to fall back to the surface at 08:00 UT while the remainder was ejected and follows the rising loop-like structures which eventually become the CME front. The rising prominence was not apparent at any stage of the propagation in COR1 A and the advancing front remains the only distinguishable facet of the CME from this line-of-sight (LOS).

A noteworthy caveat of using base difference imaging is the assumption that the background corona in the pre-event image has the same brightness in all subsequent images. This may not always be true and any excess brightness in the pre-event image will produce negative pixel values in the base difference. This is apparent in the COR1 images as the CME interacts with a streamer, displacing it as the leading CME front expands laterally as well as moves outward. The

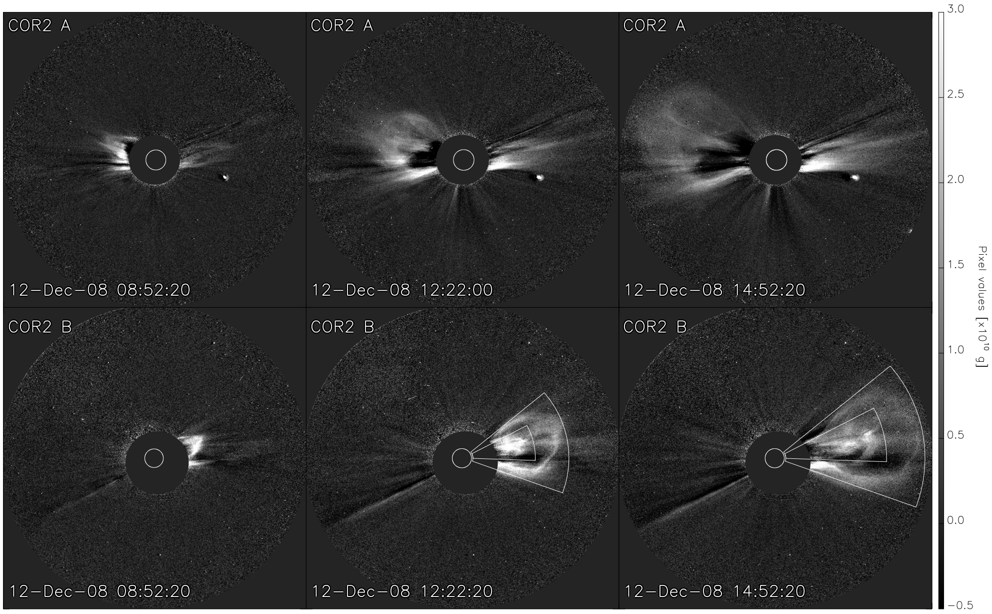

Figure 4.2: Selection of base difference images of the CME in COR2 A (top row) and COR2 B (bottom row), with pixel values of grams. The CME is clearly distinguishable in both fields of view. Only the B field view shows clearly the three part structure of core, cavity and front. The COR2 B images were used to measure core and front mass separately

streamer is visible as a dark feature that grows with time at the southward flank of the CME in the COR1 B images, Figure 4.1. The black areas are indicative of negative pixel values. The COR1 A images also suffer from negative pixels, especially at later times, see Figure 4.1 top row, 09:15 UT image. The front of the CME starts to exit both the A and B field of view at ∼08:35 UT.

The CME first appears in the COR2 field of view at ∼07:52 UT with the CME apex at a height of $\sim 3\,R_\odot$ in both A and B images. In the B coronagraph, by 10:52 UT the three part structure of core, cavity, and bright front is clearly visible and the overall structure grows in size as the CME propagates to larger heights. The core becomes more tenuous and the mass distribution becomes homogenous after 15:52 UT when the front starts to exit the field of view. The distinction between core and front is not as clear in COR2 A and the mass distribution appears more homogenous throughout the propagation. As with the COR1 images, COR2 A is also affected by excess brightness in the pre-event image, as is apparent by a growing dark feature in its southern half. As the pre-event image for COR2 B is the cleanest of the pre-event images (it contains the least contamination by streamers), the COR2 B data are considered the best candidate for accurate CME mass measurements.

4.1.2 Evaluation of Uncertainties

The method by which mass measurements are derived from white light coronagraph images is based on theory first developed by Minnaert (1930) in which the scattering geometry of a single electron at a particular point in the solar atmosphere is considered. Further development of the theory by van de Hulst (1950) led to the derivation of what are now known as the van de Hulst coefficients. The coefficients treat each component of the incident electric field vector separately and take into account the finite size of the solar disk (Billings, 1966; Howard & Tappin, 2009b; Minnaert, 1930). An important fact arising from these expressions is the dependence of scattering intensity on the angle, χ, between the radial vector from sun centre to the scattering electron and a position vector from observer towards the electron–the LOS, see Figure 4.3. Scattering efficiency is minimized when this angle is 90°. However, along the LOS such an angle occurs at the point of minimum distance from sun centre where the incident intensity (that the electron receives) and electron density are maximized. This means scattered light in the corona is most intense along a plane perpendicular to the observer's LOS despite the efficiency of scattering being minimized at such viewing angles (Howard & Tappin, 2009b). This plane perpendicular to the LOS is known as the plane-of-sky (POS)

Studies using single LOS coronagraph data are often hindered by the unknown

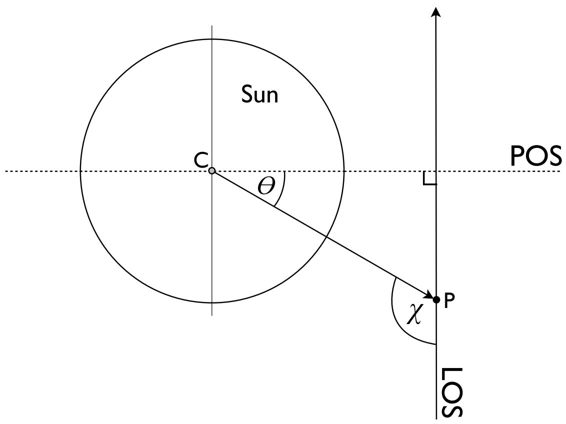

Figure 4.3: Schematic showing the relative orientation of the line-of-sight (LOS), and the plane-of-sky (POS). Electron position is at point P and C is Sun center. The vector CP may also represent CME propagation direction. Scattering efficiency is heavily dependent on the angle θ (or χ) and is least efficient when $\theta = 0°$ ($\chi = 90°$).

CME propagation angle from the POS, e.g., unknown θ (or χ) in Figure 4.3. This leads to the incorrect angle being used when inverting the van de Hulst coefficients to calculate the number of electrons contributing to the scattered light. Furthermore, because the 3-D extent of the CME is unknown it is also assumed that the CME is confined to the 2-D sky plane, leading to a significant CME mass underestimation (Vourlidas *et al.*, 2000).

The CME of 2008 December 12 was Earth-directed (**?**), making it roughly the same angular distance from both the *STEREO* A and B spacecraft, then located ±45 degrees from Earth. This known angle of propagation was used to convert from pixel values of MSB to grams via the expression

$$m_{pixel} = \frac{B_{obs}}{B_e} \times 1.97 \times 10^{-24}\,\mathrm{g} \tag{4.1}$$

where B_{obs} is the observed MSB of the pixel, B_e is the electron brightness calculated from the van de Hulst coefficients, and 1.97×10^{-24} g is a factor that converts the number of electrons to mass, assuming a completely ionized corona with a composition of 90% hydrogen and 10% helium. The known angle of propagation allowed the correct value of B_e to be computed resulting in a significant reduction in the uncertainties associated with the propagation angle. The largest remaining uncertainty is the unknown angular width along the LOS. This uncertainty was quantified in a similar approach to the method outlined in Vourlidas *et al.* (2000). This simulates the brightness of a CME with homogeneous density distribution and finite angular width along the LOS–longitudinal angular width $\Delta\theta_{long}$, allowing calculation of a simulated observed mass. Comparing this to the actual mass allowed for an evaluation of CME mass underestimation for given values of $\Delta\theta_{long}$. Since the values for $\Delta\theta_{long}$ are unknown, the expression derived in **?** for the *latitudinal* angular width of this CME as a function of height, $\Delta\theta_{lat}(r) = 25r^{0.22}$, was used to define an upper limit to $\Delta\theta_{long}$. It was assumed the CME longitudinal angular width is no more than twice the latitudinal angular width, or $\Delta\theta_{long} \leqslant 2 \times \Delta\theta_{lat}$. Such an upper limit is in agreement with simulations of flux-rope CMEs which give a typical aspect ratio of broadside to axial angular extents of $1.6 - 1.9$ (Krall & St. Cyr, 2006). Hence the value for $\Delta\theta_{long}$ at each height was used to obtain the simulated mass underestimation estimates described above. The heights and angular widths used in this study produced CME mass underestimation estimates of between 5–10% for finite angular width uncertainty. An extra mass uncertainty of 6% was added to account for the assumption of coronal abundance of 90% hydrogen and 10% helium which can lead to slight errors while converting from pixel values of MSB to grams (Vourlidas *et al.*, 2010).

To calculate the CME mass a user-selected area (the extent of the CME, for example) of the base difference image was chosen and the pixel values within this area were summed to obtain total mass. Figure 4.2 COR2 B images show an example of the sector over which pixels were summed (the smaller sectors indicate a different summing region used at a later stage). The selected area was chosen for each image in the time sequence of CME propagation so as to determine the mass variation with height in COR1 and 2 using both A and B. The selection of an area by a point and click method is of course a subjective identification of the the extent of the CME, so it is susceptible to user-generated uncertainties. To quantify these uncertainties the mass was obtained for each coronagraph image in the time sequence (as described above) and the process was repeated five times in order to obtain the mean CME mass for each image and the standard error on the mean. This standard error was defined as the uncertainty due to user bias in the point and click method of CME identification. The height at each measurement interval was taken to be the heliocentric distance of the CME apex in the image i.e., the apex of the front was chosen by simple point-and-click method. The uncertainty on the apex height was also found by the standard error on five runs.

The deflection of a small streamer during CME propagation produces negative pixels in the base difference images. The effect is particularly apparent in the COR1 images, Figure 4.1. It is difficult to unambiguously distinguish between streamer and CME, making it difficult to quantify the uncertainty introduced due to streamer interaction. To make an estimate of the streamer's effects, a calculation of its mass in the pre-event image was made. A number of different samples of the area of the streamer in the COR1 B pre-event image that effects all subsequent images produced a mass estimate of $\sim 5\times 10^{14}$ g. This mass was used as a measure of the uncertainty introduced due to streamer interaction in the COR1 B images. A similar analysis of the COR1 A pre-event images gave a streamer mass estimate of $\sim 7\times 10^{14}$ g. COR2 images are relatively unaffected by significant changes in background coronal brightness and do not suffer from negative pixel values to as large an extent as COR1. The pre-event image of COR2 B is particularly clean and free of background streamers, hence COR2 B images are considered to provide most accurate CME mass estimation.

Finally, in order to obtain a more complete and continuous estimate of CME mass growth, the masses determined from both COR1 and COR2 coronagraphs were summed in those cases where image times of the inner and outer coronagraphs overlapped[1]. The overlap in the inner and outer corongraphs' fields of view was also taken into account in this summation.

A concise measurement of the CME kinematics, such as velocity and acceleration, were taken from the results of the study of **?**. Since these kinematics take into account the true three dimensional surface of the front they provide reliable estimates of CME velocity and acceleration in 3-D space. These velocity and acceleration measurements were used in the calculation of kinetic energy and total force on the CME for each point in time. The CME mass used in all energy and force calculations was the asymptotic mass it approaches at later stages of its evolution beyond $10\,R_{\odot}$ as observed from the *STEREO B* spacecraft i.e., $3.4 \pm 1.0 \times 10^{15}$ g. As will be shown, there is good motivation for the use of constant mass in the magnitude of kinetic energy and force estimates.

4.1.3 Masses

The results of the calculation for CME mass development with time and height for both *STEREO* A and B coronagraphs are shown in Figure **??**. In panel (a), the height values are those taken from a point-and-click method of tracking the CME apex; these heights are corrected for CME propagation angle of $\sim 45°$.

[1] A difference in cadence of the inner and outer coronagraphs means that the images closest in time have a three minute offset e.g., a COR1 image taken at 07:25 UT was considered to be coincident in time with the COR2 image at 07:22 UT

In both panels (a) and (b), the mass estimates of *STEREO* A and B follow a similar trend and have similar values at each stage in the propagation. Such good agreement between mass values is a good indicator that $\sim 45°$ is the correct angle of propagation from the sky-plane. A change in the cadence of mass measurements is noticeable at $\sim$08:00 UT (or $\gtrsim 5\,R_\odot$). This is due to the use of only COR1 images (with a cadence of 10 minutes) prior to this time, and the use of the COR2 plus COR1 images after this time (the cadence of these measurements follows that of COR2 – 30 minutes). Comparing A and B below $4.5\,R_\odot$, mass values show a similar trend and increase at the same rate, but at approximately $3\,R_\odot$ the mass measurements in COR1 B appear to increase to a much larger value then fall again. This effect is visible in the COR1 A measurements, albeit diminished. It is probably due to the presence of a prominence which contains a significant mass content and therefore contributes a large amount to total measured CME mass. Also, early on in its propagation, the prominence may still be emitting H-α line radiation (656.28 nm) due to the larger fraction of neutral hydrogen at its cooler temperatures.

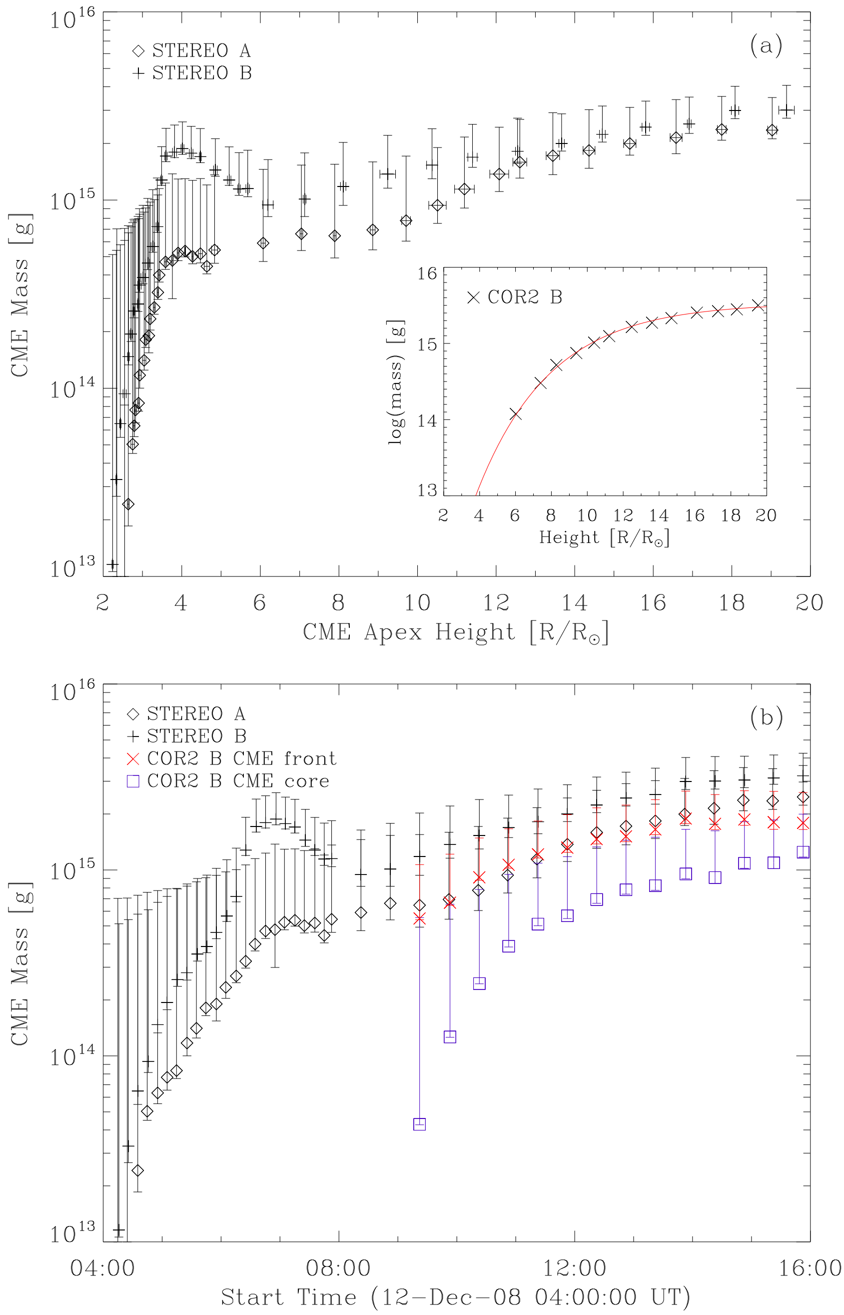

Figure 4.4: CME mass development with height (a) and time (b), for the 2008 December 12 CME. After ~08:00 UT ($\gtrsim 5\,R_\odot$) the masses from the inner and outer coronagraphs are summed to show uninterrupted mass development from ~2–20 $R_\odot$ over a period of 12 hours. The small bump in the CME mass at ~07:00 UT (~4 $R_\odot$) is probably due to an unknown amount of H-α emission from the prominence. Mass of CME front and core are also shown, red '×' and blue square, for COR2 B, panel (b). After 14:52 UT they share approximately equal mass. The inset of (a) shows mass development with height for COR2 B only; the red curve represents a fit to the data whereby the mass asymptotically approaches $3.4 \pm 1.0 \times 10^{15}$ g.

The COR1 imaging passband is centered on H-α so any emission in the prominence from neutral hydrogen could be contributing to light received by the COR1 coronagraphs, this is apparent from the saturation region in the COR1 B images in Figure 4.1. Since this is resonance line emission, and not Thomson scattered emission, it leads to an erroneous measurement in CME mass. Thus, it is assumed the larger rise and fall in CME mass is caused by the prominence entering and exiting the COR1 B field of view. The effect is diminished in COR1 A since the prominence does not enter the FOV to as large an extent as in COR1 B. The interpretation that the 'mass bump' is not actual mass growth (or loss) is supported by previous measurements where CME mass increase follows a trend with height described by $M_{cme}(h) = M_a(1 - e^{-h/h_a})$, where M_a is the final mass the CME approaches asymptotically and h_a is the height at which the CME reaches $0.63M_a$ (Colaninno & Vourlidas, 2009), with no 'bump' in mass earlier on. The decline in mass after the peak may be explained by the ionization of neutral hydrogen such that H-α emission diminishes and simply becomes Thomson scattering of free electrons, as with the rest of the CME material.

In order to produce a fit to the data, the COR2 B mass results were chosen because its pre-event image was largely free of any bright streamers or other features which introduce unwanted effects in the production of base difference images, as described above. A fit with the above equation resulted in a final asymptotic CME mass of $3.4 \pm 1.0 \times 10^{15}$ g, with a scale height of $h_a = 2.9\,R_\odot$. This fit is plotted along with the COR2 B data in the inset panel of Figure **??**(a). Note that the mass increase is due to material coming up from below the occulting disk, and not actual mass gain of the CME. The uncertainty on the above asymptotic mass value was taken to be 30%, from the largest uncertainty due to finite width, the conversion factor uncertainty as described above, the standard error user-generated uncertainty, and uncertainty due to streamer interaction.

In each image where the CME core and front are distinguishable, their masses were measured separately. This was carried out by user selected regions demarcating the areas of core and front, see COR2 B at 12:22 UT and 14:52 UT in Figure 4.2 for an example of the separate core and front sectors over which pixel values were summed to obtain total mass. The uncertainties due to finite width of the observed object also apply to the core and front measurements, however, since the widths of these particular areas of the CME are unknown we chose the maximum uncertainty of 10% from the above analysis since neither core nor front can be any wider than the maximum width assigned to this CME. The remaining uncertainties described above were also applied. The mass development of core and front with time is shown in Figure **??**(b). The two mass measurements are subject to an observational effect of apparent exponential mass growth, however by the time the CME is fully in the field of view at 14:45 UT the core and front share approximately equal mass.

4.2 Energies and Dynamics

In the following calculations, all measurements of force and kinetic energy use the asymptotic mass of $3.4 \pm 1.0 \times 10^{15}$ g and not the instantaneous mass values calculated from each coronagraph image i.e., the CME is considered to begin its propagation with this mass and does not acquire any mass as it propagates.

Estimates of the force and kinetic energy use the 3-D velocity and acceleration measurements produced by **?**. Their method firstly identifies the CME front in each coronagraph image using a multiscale edge detection filter. The front edges were then used to define a quadrilateral in space into which an ellipse is fit, this method is known as elliptical tie-pointing. This was done for multiple horizontal planes through the CME so that the fit ellipses outline a curved front in 3-D space. The speed and acceleration were then deduced from the change in position of the front, with time, through the *STEREO* COR1, COR2 and HI fields of view. Since mass measurements in this study use only the COR1 and COR2 coronagraphs, HI kinematics measurements have been excluded here. The CME front position uncertainty in *STEREO* A and B coronagraphs was determined from the filter width in the multiscale analysis. Velocity and acceleration uncertainties were then propagated from position uncertainty. Figure **??**(a) shows CME velocity as a function of heliocentric distance, along with acceleration in panel (b).

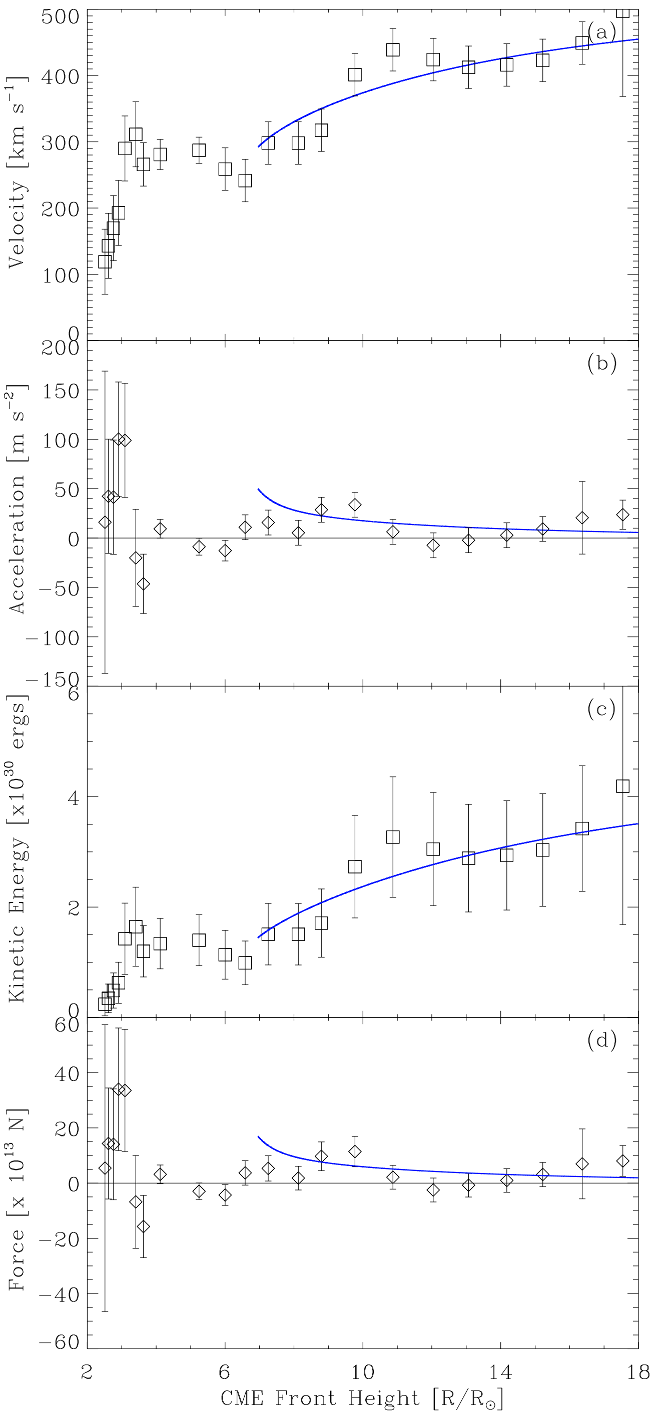

Figure 4.5: (a) CME velocity as a function of heliocentric distance, including a fit to the data produced using an aerodynamic drag model beyond $\sim 7\,R_\odot$ (**?**). (b) Acceleration of CME, including fit, derived from the velocity data and fit. Panel (c) and (d) show the kinetic energy and force, respectively, both calculated using constant CME mass of $3.4 \pm 1.0 \times 10^{15}$ g and kinematics results from (a) and (b). Also shown are the fits to energy and force produced from fits to velocity and acceleration.

The CME kinetic energy was calculated using $E_{kin} = 1/2 M_{cme} v_{cme}^2$, where M_{cme} is the final asymptotic mass of $3.4 \pm 1.0 \times 10^{15}$ g and v_{cme} are the instantaneous velocity measurements, results of this calculation are shown in Figure **??**(c). The kinetic energy shows an initial rise towards $6.3 \pm 3.7 \times 10^{29}$ ergs at $\sim 3\,R_{\odot}$, beyond which it rises steadily to $4.2 \pm 2.5 \times 10^{30}$ ergs at $\sim 18\,R_{\odot}$, these values are similar to those reported in Vourlidas *et al.* (2000, 2010) and Emslie *et al.* (2004).

The total force on the CME was calculated using $F_{total} = M_{cme} a_{cme}$, where M_{cme} is as above and a_{cme} is taken from the instantaneous acceleration values. As shown in panel (d) of Figure **??**, the force initially grows significantly, reaching a maximum value of $3.4 \pm 2.2 \times 10^{14}$ N at $\sim 3\,R_{\odot}$. The early rise and fall in acceleration (or force) is in agreement with a previous study of a CME observed to reach peak acceleration at $\sim 1.7\,R_{\odot}$ after which it reaches a constant velocity beyond $\sim 3.4\,R_{\odot}$ (Gallagher *et al.*, 2003). Such results are also found in a statistical study which shows that the majority of CMEs have peak acceleration in the low corona with a mean height of maximum acceleration at $1.5\,R_{\odot}$ (Bein *et al.*, 2011). Similarly, observational studies by Zhang *et al.* (2001) and Zhang *et al.* (2004) also show early phase peak acceleration between 2–5 $R_{\odot}$ and forces on the order of 10^{15} N and 10^{12} N, depending on whether the CME shows large initial acceleration or a slow, more gradual acceleration.

After this early peak, the force drops to an average value of $3.8 \pm 5.4 \times 10^{13}$ N at distances between 7–18 $R_{\odot}$. It is apparent from Figure **??**(a) that the velocity continues to increase beyond $7\,R_{\odot}$, implying that a positive radial force must be present. To clarify this, a fit to the velocity data using a model for solar wind drag on the CME beyond $7\,R_{\odot}$ (as outlined in **?**) is shown in Figure **??**(a). Although the data suggest a non-monotonic increase in velocity, the fit reveals that propagation is best described by a steadily increasing velocity between 7–

$18\,R_\odot$. The acceleration and kinetic energy curves derived from this velocity fit are shown in Figure **??**(b) and (c). In Figure **??**(d), the curve for the force derived from the velocity fit initially deviates from the data at $\sim 7\,R_\odot$, however beyond this distance there is good agreement with the data and the derived force is entirely positive. This suggests that the solar wind exerts a positive aerodynamic drag force on the CME, resulting in a velocity that approaches the asymptotic solar wind speed at large heliospheric distances.

4.2.1 Forces acting on CMEs

It should be noted that Figure **??** shows an overall exponential increase in CME mass with height which could be interpreted as the CME rapidly gaining mass as it propagates. Care should be taken with this interpretation since this apparent exponential mass increase is almost certainly due to the CME moving into the field of view, therefore allowing us to measure more of its mass content; such an interpretation is in agreement with similar assertions made in Vourlidas *et al.* (2010). It is difficult to distinguish between actual CME mass growth and an apparent growth due to more of the CME being observed. If the initial early rise in CME mass is assumed to be an observational artifact then we can interpret the CME mass to be in the range of $(3\text{–}3.5)\times10^{15}$ g for most of its early propagation i.e., the CME already has such a mass before launch and does not acquire more mass (via inflows or otherwise) during propagation. Such an interpretation is in agreement with CME mass measurements calculated from dimmings in *STEREO* Extreme Ultraviolet Image (EUVI) images, which show the mass calculated from EUV images to be approximately equal to CME mass in COR2 images, $m_{EUVI}/m_{COR2} = 1.1 \pm 0.3$ (Aschwanden *et al.*, 2009). Once the CME bubble is in the field of view at $\sim 10\,R_\odot$ the mass in its entirety can be measured and the increase beyond this point, if any, is slow and steady, Figure **??**.

The early stages of CME propagation are dominated by a sharp rise to a peak force of $3.4 \pm 2.2{\times}10^{14}$ N at $\sim 3\,R_{\odot}$ followed by a sharp decline, Figure **??**(d). The catastrophe model (Forbes & Isenberg, 1991; Forbes & Priest, 1995; Lin & Forbes, 2000), magnetic breakout model (Antiochos *et al.*, 1999b; Lynch *et al.*, 2008), and toroidal instability model (Chen, 1996; Kliem & Török, 2006) employ a number of forces acting on the CME to produce an over all acceleration into interplanetary space. For example, the toroidal instability model used by Chen (1996) uses a Lorentz hoop force (or Lorentz self-force), solar wind drag, and gravity to provide a net force acting on the CME between 2–3 $R_{\odot}$ that quickly rises to a peak total force of $\sim 10^{16}$ N and then falls rapidly.

If we assume that the peak force observed for the 2008 December 12 CME is the net force due to similar forces used in the above models, such as the solar wind drag, gravity, and some form of magnetic CME driver e.g., a $\mathbf{J} \times \mathbf{B}$ force, we may estimate their relative contribution. The force due to solar wind drag on the CME is given by

$$\mathbf{F}_d = -\frac{1}{2} C_d \rho_{sw} A_{cme} (\mathbf{v} - \mathbf{v}_{sw}) \mid \mathbf{v} - \mathbf{v}_{sw} \mid \tag{4.2}$$

where M_{cme} is the CME mass, $\mathbf{v}$ is the CME velocity, C_d is the drag coefficient, ρ_{sw} is the solar wind mass density, A_{cme} is the CME area exposed to solar wind drag and $\mathbf{v}_{sw}$ is the solar wind velocity (Maloney & Gallagher, 2010). To estimate the effects of this force we use $\rho_{sw} = n_p m_p$, where m_p is proton mass, and assume ionization fraction of $\chi = 1$ such that $n_p = n_e\,[cm^{-3}]$. Electron density, and hence proton density, is then given by an interplanetary density model derived from a special solution of the Parker solar wind equation (Mann *et al.*, 1999), solar wind velocity values as a function of height are also determined using this model. A_{cme}

is estimated using the expression derived in **?** for latitudinal angular width of the CME as a function of height, $\Delta\theta_{lat}(r) = 26r^{0.22}$. This is used to derive an arc length of the CME front and, as above, making the assumption $\Delta\theta_{long} = 2\times\Delta\theta_{lat}$, the two arc lengths derived from these angles then give the surface that the solar wind acts on, thus $A_{cme} = 1352r^{2.44}$. Setting the drag coefficient $C_d = 1$, and using the Mann *et al.* (1999) model to derive a density and a solar wind velocity of $2.3\times10^5\,\mathrm{cm^{-3}}$ and $70\,\mathrm{km\,s^{-1}}$, respectively, equation [1] then gives a force of $\mathbf{F}_d = -8.0\times10^{12}\,\hat{r}$ N for solar wind drag at $\sim3\,R_\odot$, where $\hat{r}$ is a unit vector in the positive radial direction.

A simple estimate of force due to gravity is given by $\mathbf{F}_g = GM_\odot M_{cme}/\mathbf{r}^2$, where G is the universal gravitational constant, $M_\odot$ is solar mass, M_{cme} is CME mass, and $\mathbf{r}$ is a heliocentric position vector[1]. Given a CME mass of 3.4×10^{15} g the force due to gravity at a heliocentric distance of $3\,R_\odot$ is $\mathbf{F}_g = -1.0\times10^{14}\,\hat{r}$ N. The only remaining contribution is due to some form of magnetic CME driver, F_{mag}, which is estimated using

$$\mathbf{F}_{mag} = \mathbf{F}_{total} - \mathbf{F}_d - \mathbf{F}_g \tag{4.3}$$

(the pressure gradient in the CME equation of motion is assumed to be negligible and has been omitted here). Using the above values, the total magnetic contribution to CME force is calculated to be $\mathbf{F}_{mag} \approx 4.5\times10^{14}\,\hat{r}$ N at $3\,R_\odot$, indicating that this is the largest driver of CMEs at low coronal heights. Lorentz force dominated dynamics in early phase CME propagation are reported in Bein *et al.* (2011), in which a statistical study of a large sample of CMEs in EUVI,

[1]Ideally the heliocentric distance of the CME centre of mass would be used here. However an unknown amount of mass is obscured by the coronagraphs occulting disk, making the mass distribution and hence COM difficult to determine. Thus the CME front height is used in the calculation of force due to gravity

COR1, and COR2 indicated an early phase acceleration for the majority of CMEs that is attributable to a Lorentz force. A similar result of an observational study by Vršnak (2006) found that the Lorentz force plays a dominant role within a few solar radii. It should be noted that although we have labelled the force F_{mag}, there is no distinction on the exact form of this force e.g., whether it is magnetic pressure, magnetic tension, or a Lorentz self-force that acts as the driver. Also, any non-radial motion of the CME, such as that described in **?**, is not taken into account here; any force estimates are purely radial in direction.

4.3 Conclusion

The *STEREO* COR1/2 coronagraphs have been used to determine the mass development of the 2008 December 12 CME. Knowledge of the longitudinal propagation angle of the CME allowed for a significant reduction in the mass uncertainty, giving a final estimate of $3.4 \pm 1.0 \times 10^{15}$ g. Using kinematics results of a previous study (**?**), the velocity and acceleration of the CME were combined with the mass measurements to determine the kinetic energy and total force on the CME. The early phase propagation of the CME was found to be dominated by a force of peak magnitude of $3.4 \pm 2.2 \times 10^{14}$ N at $\sim 3.0\,R_{\odot}$, after which the magnitude declines rapidly and settles to and average of $3.8 \pm 5.4 \times 10^{13}$ N. This early rise and fall in total force (or acceleration) is in agreement with previous observations of CME kinematics (Bein *et al.*, 2011; Gallagher *et al.*, 2003). Similarly results of observational studies by Zhang *et al.* (2001) and Zhang *et al.* (2004) also show early phase peak acceleration between 2–5 $R_{\odot}$ and forces on the order of 10^{15} N and 10^{12} N. The kinetic energy shows an initial rise towards $6.3 \pm 3.7 \times 10^{29}$ ergs at $\sim 3\,R_{\odot}$, beyond which it rises steadily to $4.2 \pm 2.5 \times 10^{30}$ ergs at $\sim 18\,R_{\odot}$, such order of magnitudes are similar to those reported in Emslie *et al.* (2004); Vourlidas *et al.* (2000) and are typical of CME kinetic energies (Vourlidas *et al.*, 2010).

Such CME kinematics and dynamics property estimates cannot be carried out when unknown propagation angle hinders an accurate calculation of CME mass, hence adding unacceptable uncertainty to any subsequent calculations. This highlights the need for similar studies using the *STEREO* mission's ability to accurately determine the physical properties of CMEs, such as mass, with remarkably reduced uncertainty. Increasing the accuracy of force estimates of other well studied CMEs will allow for a more complete view of the magnitude of the forces influencing CME propagation and will allow model parameters to be more accurately constrained.

5

Coronal Mass Ejection Masses, Shocks, and Particle Acceleration

5.1 Radio Bursts

5.1.1 Type II, Type III, and Herringbones

5.2 EUV Wave and Radio Source

5.2.1 Relationship with Radio Spectra

5.3 Role of the CME

5.3.1 CME Bow Shock

5.3.2 Relationship Between CME, CBF, and Radio bursts

A

A Nice Appendix

If we assume the herringbones are due to the shock drift acceleration process then the velocity upon a reflection from the shock is

$$v_{r,||} = 2v_{shock}\sec\theta_{Bn} - v_{i,||} \tag{A.1}$$

where $v_{r,||}$ is the reflected parallel velocity of the particle, $v_{i,||}$ is the incident parallel velocity of the paticle, v_{shock} is the shock velocity, and θ is the angle between upstream $B-$field and shock normal n. Taking the shock speed to be the speed of the 150 MHz radio source, $550 \times 10^3\,\mathrm{m\,s^{-1}}$, and $v_{i,||}$ to be the thermal speed of an electron

$$v_{thermal} = \sqrt{\frac{3k_bT}{m_e}} \tag{A.2}$$

At 1×10^6 K, $v_{thermal} = v_{i,||} = 6.7 \times 10^6\,\mathrm{m\,s^{-1}}$. Now, the herringbone electron speed 0.15 c, this is the reflected speed $v_{r,||}$ in equation A1. Rearranging A1 we get

$$\theta_{Bn} = \sec^{-1}\left(\frac{1}{2}\frac{v_{r,||} + v_{i,||}}{v_{shock}}\right) \tag{A.3}$$

Substituting the above values we get $\theta_{Bn} = 88°$. Independent verification of a quasi-perpendicular shock orientation!

A.1 Radio burst intensity

$$\Phi_F \approx 72\sqrt{3}\frac{\gamma_{L'}}{\gamma_S}\frac{v_e^3}{c^3}\frac{v_b}{\Delta v_b}\frac{e^{-u_c^2}}{u_c\sqrt{\pi}}\zeta_F \tag{A.4}$$

$$\Phi_H \approx \frac{18\sqrt{3}}{5\gamma_t}\sqrt{\frac{m_i}{\gamma_t m_e}}\frac{v_e^3 v_b^3}{c^5}\frac{v_b}{\Delta v_b}\zeta_H \tag{A.5}$$

the expression involving u_c represent an 'escape factor' for the fundamental taking into account absorption and scattering of the radiation. $\frac{\gamma_{L'}}{\gamma_S}$ is the ratio of the damping rates of the product waves out of processes in equations 2.56 and 2.55. The ζ terms are the fractions of Langmuir waves that are kinematically able to contribute to the fundamental or harmonic emission, given by

$$\zeta_F \approx \exp\left[-\frac{4\gamma_t m_e}{45 m_i}\left(\frac{v_b}{\Delta v_b}\right)^2\left(\frac{3}{2}\sqrt{\frac{m_i}{\gamma_t m_e}} - \frac{v_b}{v_e}\right)^2\right] \tag{A.6}$$

$$\zeta_H \approx \frac{c}{2v_b}\sqrt{\frac{\pi}{6}}\frac{\beta\Delta v_b}{v_b}\left[\mathrm{erf}\left(\frac{\frac{v_e\sqrt{3}}{c} + \frac{2}{3}\sqrt{\frac{\gamma_t m_e}{m_i}}}{\frac{v_e}{v_b}\frac{\beta\Delta v_b}{v_b}\sqrt{2}}\right) + \mathrm{erf}\left(\frac{\frac{v_e\sqrt{3}}{c} - \frac{2}{3}\sqrt{\frac{\gamma_t m_e}{m_i}}}{\frac{v_e}{v_b}\frac{\beta\Delta v_b}{v_b}\sqrt{2}}\right)\right] \tag{A.7}$$

where erf is the error function.

A.2 Band-splitting

Using a ploytropic index of $\gamma = 5/3$ (monatomic) means the shock compression can be no more than a factor of 4. Another extremely important fact arising from this is that magnetic compression can also be no greater than 4 i.e., from equation 4(b) $B_2/B_1 = \chi$. $\chi < 4$ has consequences for the shock drift acceleration mechanism and provides an upper limit to the particle energy gain

may also provide an upper limit to the level of band splitting in type II radio bursts (since this effect is thought to be related to the emission induced up/downstream of the shock). Although the maximum compression ration of 4 was derived from the roots of the quadratic for χ for the perpendicular shock, a similar analysis for the much more general oblique shock also leads to the same result. The density compression and tangential magnetic compression can be no more than a factor of $(\gamma + 1)/(\gamma - 1)$ for any MHD shock.

Polynomials such as (6) are extremely useful, and can lead to simple expressions for the Alfvénic-Mach number in terms of χ, in this case

$$M_A = \sqrt{\frac{\chi(\chi + 5 + 5\beta)}{2(4 - \chi)}} \tag{A.8}$$

for a perpendicular shock. If the shock speed and compression ratio are known, this equation provides a means of measuring the Alfvén speed in the shock medium.

This technique is exploited in the analysis of type II radio bursts. As the shock propagates into the corona it emits EM radiation at the local plasma frequency (1) (see section 4), and since the density drops as the shock travels into the heliosphere, so too does the frequency of emission. From frequency drift rate an estimate of shock speed is possible. If band splitting of the emission is present this is interpreted as emission from upstream and downstream of the shock, which provides a diagnostic of upstream/downstream densities via (1) and hence an estimate of χ (Vršnak & Gopalswamy, 2002). However, use of (8) in calculating Mach number and Alfvén speed in the corona has some clear shortcomings such that it clearly ignores any dependency of the angle between magnetic field, velocity vector and shock normal i.e., (8) only applies to a purely perpendicular shock.

The general oblique shock case requires extra terms in the polynomial such as θ_{Bn} and θ_{vn} (θ_{Bn} is the angle between shock normal and magnetic field, and θ_{vn} is the angle between shock normal and plasma flow). For the oblique case the polynomial becomes

$$(A^2-\chi)^2\left[A^2-\frac{2\chi S^2}{\chi+1-\gamma(\chi-1)}\right]-\chi k^2 A^2\left[\frac{2\chi-\gamma(\chi-1)}{\chi+1-\gamma(\chi-1)}A^2-\chi\right]=0 \quad (A.9)$$

where $A = \frac{M_A \cos\theta_{vn}}{cos(\theta_{Bv}-\theta_{bn})}$, $S = \frac{c_s}{v_A}$, $k = \tan(\theta_{vn} - \theta_{Bv})$ [1] (Kabin, 2001). Equation (6) is a quadratic of variable χ, the more general equation (9) is a cubic equation for χ, the roots of which give the compression for the oblique case. Since it is a function of M_A, θ_{vn}, and θ_{bv}, χ may have a range of values depending not only on Mach number but also shock orientation. Figure 2 illustrates the broad range in compressions of $0< \chi <3.5$ across the shock depending on both flow and magnetic field orientation with respect to the shock normal, and in this case $M_A = 2.5$. This is a very general case, however, permitting any angle of orentation of B and v. Since type II bursts are thought to be from shocks that are quasi perpendicular,

[1] θ_{Bv} is angle between magnetic field and velocity vector, it has a simple relationship with θ_{Bn}

this places restriction on the values for θ_{vn}, and θ_{Bn}, especially when the flow is considered to be head-on i.e. $\theta_{vn} = 0°$. Therefore in the quasi-perpendicular case their is a tighter constraint on the amount of compression across the shock. Further constraining the Mach number to a limited range of values puts quite a limiting range on the compression ratio, and hence a limiting range of band splitting of type II radio bursts since $f_{plasma} \approx 9000\sqrt{n_e}$, hence

$$\delta_{bs} \equiv \frac{f_{upper}}{f_{lower}} \approx \sqrt{\frac{n_{e,d}}{n_{e,u}}} = \sqrt{\chi} \tag{A.10}$$

where $n_{e,d}$ and $n_{e,u}$ are downstream and upstream plasma number densities, and δ_{bs} is the ratio of upper to lower band frequencies, f_{upper} and f_{lower} respectively, in a split radio burst. Figure 3 shows the expected range in band splitting ($\delta_{bs} = \sqrt{\chi}$) for a type II given a range in Alfvén Mach numbers $1 < M_A < 4$, and quasi-perpendicular magnetic field orientations $45° < \theta_{Bn} < 90°$. This analysis shows that for a quasi-perpendicular shock the theoretically predicted range in type II band-spliting is $1 < \delta_{bs} < 1.8$. Such an upper limit to the level of band-splitting seems excessive and is probably due to a large upper limit to the Mach number being used to calculate the compression ratio. This is especially relevant in the low corona where Alfvén speed can be quite large, making it difficult for a CME or blast wave to drive a shock at $M_A = 4$. Also, given a typical band-splitting ratio of $\delta_{bs} = 1.21 \pm 0.7$ at metric wavelengths (Vršnak *et al.*, 2004), this would indicate typical Alfvén-Mach number of ~ 1.5 in the low corona. This seems reasonable, however Mach numbers of $\sim$3 are possible, and figure 3 would suggest a possible band-split ratio of $\delta_{bs} \sim 1.7$ for such a Mach number. Such a level of band-splitting seems very unlikely, suggesting a quasi-perpendicular shock with a head on flow is a limiting case. More likely is a quasi-perpendicular shock with a flow orientation $\theta_{vn} \neq 0$. For example if $\theta_{Bn} = 90°$ and $\theta_{vn} = 45°$ then band splitting

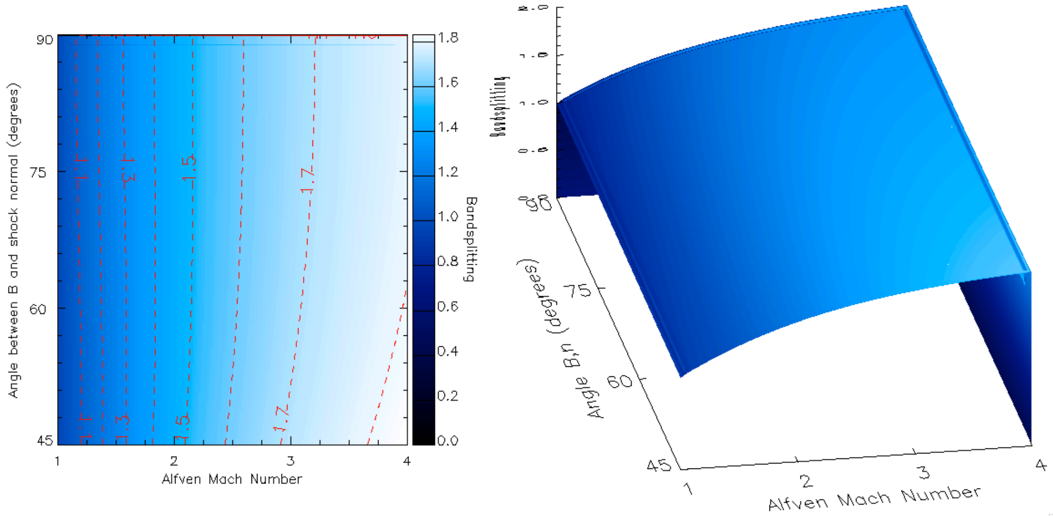

Figure A.1: Predicted band splitting ratio δ_{bs} as a function of Mach number and magnetic field orientation with respect to shock normal. Flow is anti-parallel to shock normal (head-on). Both image and surface are shown, left and right respectively. On the left, the red contours show specific values of of band-splitting. Note that for small mach numbers the level of band splitting is independent of magnetic field orientation. It is only at Mach numbers greater than ~2.1 that the B-field orientation becomes important.

can be $\delta_{bs} \sim 1.5$ for M_A=3, which is under the upper limit of observed type II band-split ratios of $\sim$ 1.58. Allowing $\theta_{vn} \neq 0$ can allow larger, more realistic Mach numbers to produce smaller and more realistic bandsplitting.

It is clear that the distribution in the level of band splitting in type II radio bursts depends not only on Mach number but the relative orientations of flow and magnetic field with respect to shock normal. A statistical analysis could possibly give an observationally predicted distribution in θ_{Bn} (provided M_A is known) that would confirm the quasi-perpendicularlity of type II-generating shocks.

References

Allen, C.W. (1947). Solar Radio-Noise of 200 Mc. /s. and its relation to Solar Observations. *Monthly Notices of the Royal Astronomical Society*, **107**, 386. (Cited on pages 38 and 94.)

Aly, J.J. (1991). How much energy can be stored in a three-dimensional force-free magnetic field? *Astrophysical Journal Letters*, **375**, L61–L64. (Cited on page 70.)

Antiochos, S.K., DeVore, C.R. & Klimchuk, J.A. (1999a). A Model for Solar Coronal Mass Ejections. *Astrophysical Journal*, **510**, 485–493. (Cited on pages 65 and 69.)

Antiochos, S.K., DeVore, C.R. & Klimchuk, J.A. (1999b). A Model for Solar Coronal Mass Ejections. *Astrophysical Journal*, **510**, 485–493. (Cited on pages 105 and 123.)

Aschwanden, M.J. (2004). *Physics of the Solar Corona. An Introduction*. Praxis Publishing Ltd. (Cited on page 63.)

Aschwanden, M.J., Nitta, N.V., Wuelser, J.P., Lemen, J.R., Sandman, A., Vourlidas, A. & Colaninno, R.C. (2009). First Measurements of the Mass of Coronal Mass Ejections from the EUV Dimming Observed with STEREO EUVI A+B Spacecraft. *Astrophysical Journal*, **706**, 376–392. (Cited on pages 31 and 122.)

Attrill, G.D.R., Harra, L.K., van Driel-Gesztelyi, L. & Démoulin, P. (2007). Coronal "Wave": Magnetic Footprint of a Coronal Mass Ejection? *Astrophysical Journal Letters*, **656**, L101–L104. (Cited on page 49.)

Aulanier, G., DeLuca, E.E., Antiochos, S.K., McMullen, R.A. & Golub, L. (2000). The Topology and Evolution of the Bastille Day Flare. *Astrophysical Journal*, **540**, 1126–1142. (Cited on page 71.)

Aurass, H. & Mann, G. (2004). Radio Observation of Electron Acceleration at Solar Flare Reconnection Outflow Termination Shocks. *Astrophysical Journal*, **615**, 526–530. (Cited on page 45.)

Aurass, H., Vršnak, B. & Mann, G. (2002). Shock-excited radio burst from reconnection outflow jet? *Astronomy & Astrophysics*, **384**, 273–281. (Cited on page 45.)

Babcock, H.W. (1961). The Topology of the Sun's Magnetic Field and the 22-YEAR Cycle. *Astrophysical Journal*, **133**, 572. (Cited on page 10.)

Bain, H.M., Krucker, S., Glesener, L. & Lin, R.P. (2012). Radio Imaging of Shock-accelerated Electrons Associated with an Erupting Plasmoid on 2010 November 3. *Astrophysical Journal*, **750**, 44. (Cited on page 41.)

Balfour, S. (1861). On the Great Magnetic Disturbance Which Extended from August 28 to September 7, 1859, as Recorded by Photography at the Kew Observatory. *Philosophical Transactions of the Royal Society of London*, **151**, 423. (Cited on page 21.)

Bein, B.M., Berkebile-Stoiser, S., Veronig, A.M., Temmer, M., Muhr, N., Kienreich, I., Utz, D. & Vršnak, B. (2011). Impulsive Acceleration of Coronal Mass Ejections. I. Statistics and Coronal Mass Ejection Source Region Characteristics. *Astrophysical Journal*, **738**, 191–+. (Cited on pages 36, 121, 124 and 125.)

Biesecker, D.A., Myers, D.C., Thompson, B.J., Hammer, D.M. & Vourlidas, A. (2002). Solar Phenomena Associated with "EIT Waves". *Astrophysical Journal*, **569**, 1009–1015. (Cited on page 47.)

Billings, D.E. (1966). *A guide to the solar corona*. (Cited on pages 106 and 110.)

Bong, S.C., Moon, Y.J., Cho, K.S., Kim, Y.H., Park, Y.D. & Choe, G.S. (2006). Direct Observation of Low Coronal Breakout: Does Breakout Precede or Follow Solar Eruption? *Astrophysical Journal Letters*, **636**, L169–L172. (Cited on page 71.)

Bougeret, J.L., Zarka, P., Caroubalos, C., Karlický, M., Leblanc, Y., Maroulis, D., Hillaris, A., Moussas, X., Alissandrakis, C.E., Dumas, G. & Perche, C. (1998). A shock associated (SA) radio event and related phenomena observed from the base of the solar corona to 1 AU. *Geophysical Research Letters*, **25**, 2513–2516. (Cited on page 45.)

Brueckner, G.E., Howard, R.A., Koomen, M.J., Korendyke, C.M., Michels, D.J., Moses, J.D., Socker, D.G., Dere, K.P., Lamy, P.L., Llebaria, A., Bout, M.V., Schwenn, R., Simnett, G.M., Bedford, D.K. & Eyles, C.J. (1995). The Large Angle Spectroscopic Coronagraph (LASCO). *Solar Physics*, **162**, 357–402. (Cited on page 105.)

Burkepile, J.T., Hundhausen, A.J., Stanger, A.L., St. Cyr, O.C. & Seiden, J.A. (2004). Role of projection effects on solar coronal mass ejection properties: 1. A study of CMEs associated with limb activity. *Journal of Geophysical Research (Space Physics)*, **109**, 3103. (Cited on pages 23, 24 and 26.)

Byrne, J.P., Maloney, S.A., McAteer, R.T.J., Refojo, J.M. & Gallagher, P.T. (2010). Propagation of an Earth-directed coronal mass ejection in three dimensions. *Nature Communications*, **1**. (Cited on page 25.)

Cairns, I.H. & Robinson, R.D. (1987). Herringbone bursts associated with type II solar radio emission. *Solar Physics*, **111**, 365–383. (Cited on page 43.)

Cairns, I.H., Knock, S.A., Robinson, P.A. & Kuncic, Z. (2003). Type II Solar Radio Bursts: Theory and Space Weather Implications. *Space Science Reviews*, **107**, 27–34. (Cited on pages 91 and 92.)

Cane, H.V. & Erickson, W.C. (2005). Solar Type II Radio Bursts and IP Type II Events. *Astrophysical Journal*, **623**, 1180–1194. (Cited on page 41.)

Cane, H.V. & White, S.M. (1989). On the source conditions for herringbone structure in type II solar radio bursts. *Solar Physics*, **120**, 137–144. (Cited on page 43.)

Cargill, P.J. (2004). On the Aerodynamic Drag Force Acting on Interplanetary Coronal Mass Ejections. *Solar Physics*, **221**, 135–149. (Cited on page 35.)

Carrington, R.C. (1859). Description of a Singular Appearance seen in the Sun on September 1, 1859. *Monthly Notices of the Royal Astronomical Society*, **20**, 13–15. (Cited on page 21.)

Chapman, S. & Ferraro, V.C.A. (1930). A New Theory of Magnetic Storms. *Nature*, **126**, 129–130. (Cited on page 21.)

Charbonneau, P. (2010). Dynamo Models of the Solar Cycle. *Living Reviews in Solar Physics*, **7**, 3. (Cited on page 10.)

Chen, J. (1989). Effects of toroidal forces in current loops embedded in a background plasma. *Astrophysical Journal*, **338**, 453–470. (Cited on pages 65, 72 and 73.)

Chen, J. (1996). Theory of prominence eruption and propagation: Interplanetary consequences. *Journal of Geophysical Research*, **1012**, 27499–27520. (Cited on pages 105 and 123.)

Chen, J., Marqué, C., Vourlidas, A., Krall, J. & Schuck, P.W. (2006). The Flux-Rope Scaling of the Acceleration of Coronal Mass Ejections and Eruptive Prominences. *Astrophysical Journal*, **649**, 452–463. (Cited on page 105.)

Chen, P.F. (2011). Coronal Mass Ejections: Models and Their Observational Basis. *Living Reviews in Solar Physics*, **8**, 1. (Cited on page 66.)

Chen, P.F., Wu, S.T., Shibata, K. & Fang, C. (2002). Evidence of EIT and Moreton Waves in Numerical Simulations. *Astrophysical Journal Letters*, **572**, L99–L102. (Cited on page 49.)

Cho, K.S., Lee, J., Moon, Y.J., Dryer, M., Bong, S.C., Kim, Y.H. & Park, Y.D. (2007). A study of CME and type II shock kinematics based on coronal density measurement. *Astronomy & Astrophysics*, **461**, 1121–1125. (Cited on pages 41 and 42.)

Cho, K.S., Bong, S.C., Moon, Y.J., Shanmugaraju, A., Kwon, R.Y. & Park, Y.D. (2011). Relationship between multiple type II solar radio bursts and CME observed by STEREO/SECCHI. *Astronomy & Astrophysics*, **530**, A16. (Cited on page 41.)

Classen, H.T. & Aurass, H. (2002). On the association between type II radio bursts and CMEs. *Astronomy & Astrophysics*, **384**, 1098–1106. (Cited on page 40.)

Colaninno, R.C. & Vourlidas, A. (2009). First Determination of the True Mass of Coronal Mass Ejections: A Novel Approach to Using the Two STEREO Viewpoints. *Astrophysical Journal*, **698**, 852–858. (Cited on pages 31, 106 and 117.)

Davis, R., Harmer, D.S. & Hoffman, K.C. (1968). Search for Neutrinos from the Sun. *Physical Review Letters*, **20**, 1205–1209. (Cited on page 4.)

de Koning, C.A., Pizzo, V.J. & Biesecker, D.A. (2009). Geometric Localization of CMEs in 3D Space Using STEREO Beacon Data: First Results. *Solar Physics*, **256**, 167–181. (Cited on page 25.)

Delannée, C., Török, T., Aulanier, G. & Hochedez, J.F. (2008). A New Model for Propagating Parts of EIT Waves: A Current Shell in a CME. *Solar Physics*, **247**, 123–150. (Cited on page 49.)

Domingo, V., Fleck, B. & Poland, A.I. (1995). The SOHO Mission: an Overview. *Solar Physics*, **162**, 1–37. (Cited on pages 22 and 106.)

Emslie, A.G., Kucharek, H., Dennis, B.R., Gopalswamy, N., Holman, G.D., Share, G.H., Vourlidas, A., Forbes, T.G., Gallagher, P.T., Mason, G.M., Metcalf, T.R., Mewaldt, R.A., Murphy, R.J., Schwartz, R.A. & Zurbuchen, T.H. (2004). Energy partition in two solar flare/CME events. *Journal of Geophysical Research (Space Physics)*, **109**, A10104. (Cited on pages 37, 121 and 125.)

Emslie, A.G., Dennis, B.R., Shih, A.Y., Chamberlin, P.C., Mewaldt, R.A., Moore, C.S., Share, G.H., Vourlidas, A. & Welsch, B.T. (2012). Global Energetics of Thirty-eight Large Solar Eruptive Events. *Astrophysical Journal*, **759**, 71. (Cited on page 37.)

Fan, Y. (2005). Coronal Mass Ejections as Loss of Confinement of Kinked Magnetic Flux Ropes. *Astrophysical Journal*, **630**, 543–551. (Cited on page 65.)

Fan, Y. (2009). Magnetic Fields in the Solar Convection Zone. *Living Reviews in Solar Physics*, **6**, 4. (Cited on page 11.)

Feldman, W.C., Anderson, R.C., Bame, S.J., Gary, S.P., Gosling, J.T., McComas, D.J., Thomsen, M.F., Paschmann, G. & Hoppe, M.M. (1983). Electron velocity distributions near the earth's bow shock. *Journal of Geophysical Research*, **88**, 96–110. (Cited on page 82.)

Fitzpatrick, R. (2000). *The Physics of Plasmas*. (Cited on page 77.)

Fontenla, J., Reichmann, E.J. & Tandberg-Hanssen, E. (1988). The Lyman-alpha line in various solar features. I - Observations. *Astrophysical Journal*, **329**, 464–481. (Cited on pages 14, 15 and 16.)

Forbes, T.G. & Isenberg, P.A. (1991). A catastrophe mechanism for coronal mass ejections. *Astrophysical Journal*, **373**, 294–307. (Cited on pages 66, 105 and 123.)

Forbes, T.G. & Priest, E.R. (1995). Photospheric Magnetic Field Evolution and Eruptive Flares. *Astrophysical Journal*, **446**, 377. (Cited on pages 65, 66, 67, 105 and 123.)

Forbush, S.E. (1946). Three Unusual Cosmic-Ray Increases Possibly Due to Charged Particles from the Sun. *Physical Review*, **70**, 771–772. (Cited on page 22.)

Foukal, P.V. (2004). *Solar Astrophysics, 2nd, Revised Edition*. Wiley-VCH. (Cited on page 2.)

Fukuda, Y., Hayakawa, T., Ichihara, E., Inoue, K., Ishihara, K., Ishino, H., Itow, Y., Kajita, T., Kameda, J., Kasuga, S., Kobayashi, K., Kobayashi, Y., Koshio, Y., Martens, K., Miura, M., Nakahata, M., Nakayama, S., Okada, A., Oketa, M., Okumura, K., Ota, M., Sakurai, N., Shiozawa, M., Suzuki, Y., Takeuchi, Y., Totsuka, Y., Yamada, S., Earl, M., Habig, A., Hong, J.T., Kearns, E., Kim, S.B., Masuzawa, M., Messier, M.D., Scholberg, K., Stone, J.L., Sulak, L.R., Walter, C.W., Goldhaber, M., Barszczak, T., Gajewski, W., Halverson, P.G., Hsu, J., Kropp, W.R., Price, L.R., Reines, F., Sobel, H.W., Vagins, M.R., Ganezer, K.S., Keig, W.E., Ellsworth, R.W., Tasaka, S., Flanagan, J.W., Kibayashi, A., Learned, J.G., Matsuno, S., Stenger, V., Takemori, D., Ishii, T., Kanzaki, J., Kobayashi, T., Nakamura, K., Nishikawa, K., Oyama, Y., Sakai, A., Sakuda, M., Sasaki, O., Echigo, S., Kohama, M., Suzuki, A.T., Haines, T.J., Blaufuss, E., Sanford, R., Svoboda, R., Chen, M.L., Conner, Z., Goodman, J.A., Sullivan, G.W., Mori, M., Hill, J., Jung, C.K., Mauger, C., McGrew, C., Sharkey, E., Viren, B., Yanagisawa, C., Doki, W., Ishizuka, T., Kitaguchi, Y., Koga, H., Miyano, K., Okazawa, H., Saji, C., Takahata, M., Kusano, A., Nagashima, Y., Takita, M., Yamaguchi, T., Yoshida, M., Etoh, M., Fujita, K., Hasegawa, A., Hasegawa, T., Hatakeyama, S., Iwamoto, T., Kinebuchi, T., Koga, M., Maruyama, T., Ogawa, H., Suzuki, A., Tsushima, F., Koshiba, M., Nemoto, M., Nishijima, K., Futagami, T., Hayato, Y., Kanaya, Y., Kaneyuki, K., Watanabe, Y., Kielczewska, D., Doyle, R., George, J., Stachyra, A., Wai, L., Wilkes, J. & Young, K. (1998). Measurements of the Solar Neutrino Flux from Super-Kamiokande's First 300 Days. *Physical Review Letters*, **81**, 1158–1162. (Cited on page 5.)

Gabriel, A.H. (1976). A magnetic model of the solar transition region. *Royal Society of London Philosophical Transactions Series A*, **281**, 339–352. (Cited on pages 14, 15 and 16.)

Gallagher, P.T., Lawrence, G.R. & Dennis, B.R. (2003). Rapid Acceleration of a Coronal Mass Ejection in the Low Corona and Implications for Propagation. *Astrophysical Journal Letters*, **588**, L53–L56. (Cited on pages 26, 28, 121 and 125.)

Ginzburg, V.L. & Zhelezniakov, V.V. (1958). On the Possible Mechanisms of Sporadic Solar Radio Emission (Radiation in an Isotropic Plasma). *Soviet Astronomy*, **2**, 653. (Cited on page 90.)

Gold, T. (1962). Magnetic Storms. *Space Science Reviews*, **1**, 100–114. (Cited on page 22.)

Goossens, M., ed. (2003). *An introduction to plasma astrophysics and magnetohydrodynamics*, vol. 294 of *Astrophysics and Space Science Library*. (Cited on page 57.)

Gopalswamy, N. & Kundu, M.R. (1992). Estimation of the mass of a coronal mass ejection from radio observations. *Astrophysical Journal Letters*, **390**, L37–L39. (Cited on page 31.)

Gopalswamy, N. & Thompson, B.J. (2000). Early life of coronal mass ejections. *Journal of Atmospheric and Solar-Terrestrial Physics*, **62**, 1457–1469. (Cited on pages 21 and 26.)

Gopalswamy, N., Yashiro, S., Temmer, M., Davila, J., Thompson, W.T., Jones, S., McAteer, R.T.J., Wuelser, J.P., Freeland, S. & Howard, R.A. (2009). EUV Wave Reflection from a Coronal Hole. *Astrophysical Journal Letters*, **691**, L123–L127. (Cited on page 47.)

Gopalswamy, N., Nitta, N., Akiyama, S., Mäkelä, P. & Yashiro, S. (2012). Coronal Magnetic Field Measurement from EUV Images Made by the Solar Dynamics Observatory. *Astrophysical Journal*, **744**, 72. (Cited on page 51.)

Gosling, J.T. (1993). The solar flare myth. *Journal of Geophysical Research*, **98**, 18937–18950. (Cited on page 65.)

Gosling, J.T., Hildner, E., MacQueen, R.M., Munro, R.H., Poland, A.I. & Ross, C.L. (1976). The speeds of coronal mass ejection events. *Solar Physics*, **48**, 389–397. (Cited on page 40.)

Grechnev, V.V., Afanasyev, A.N., Uralov, A.M., Chertok, I.M., Eselevich, M.V., Eselevich, V.G., Rudenko, G.V. & Kubo, Y. (2011a). Coronal Shock Waves, EUV Waves, and Their Relation to CMEs. III. Shock-Associated CME/EUV Wave in an Event with a Two-Component EUV Transient. *Solar Physics*, **273**, 461–477. (Cited on pages 48 and 49.)

Grechnev, V.V., Uralov, A.M., Chertok, I.M., Kuzmenko, I.V., Afanasyev, A.N., Meshalkina, N.S., Kalashnikov, S.S. & Kubo, Y. (2011b). Coronal Shock Waves, EUV Waves, and Their Relation to CMEs. I. Reconciliation of "EIT Waves", Type II Radio Bursts, and Leading Edges of CMEs. *Solar Physics*, **273**, 433–460. (Cited on page 47.)

Guo, F. & Giacalone, J. (2010). The Effect of Large-scale Magnetic Turbulence on the Acceleration of Electrons by Perpendicular Collisionless Shocks. *Astrophysical Journal*, **715**, 406–411. (Cited on page 44.)

Hey, J.S. (1946). Solar Radiations in the 4-6 Metre Radio Wave-Length Band. *Nature*, **157**, 47–48. (Cited on page 38.)

Holman, G.D. & Pesses, M.E. (1983). Solar type II radio emission and the shock drift acceleration of electrons. *Astrophysical Journal*, **267**, 837–843. (Cited on page 84.)

Howard, R.A., Moses, J.D., Vourlidas, A., Newmark, J.S., Socker, D.G., Plunkett, S.P., Korendyke, C.M., Cook, J.W., Hurley, A., Davila, J.M., Thompson, W.T., St Cyr, O.C., Mentzell, E., Mehalick, K., Lemen, J.R., Wuelser, J.P., Duncan, D.W., Tarbell, T.D., Wolfson, C.J., Moore, A., Harrison, R.A., Waltham, N.R., Lang, J., Davis, C.J., Eyles, C.J., Mapson-Menard, H., Simnett, G.M., Halain, J.P., Defise, J.M., Mazy, E., Rochus, P., Mercier, R., Ravet, M.F., Delmotte, F., Auchere, F., Delaboudiniere, J.P., Bothmer, V., Deutsch, W., Wang, D., Rich, N., Cooper, S., Stephens, V., Maahs, G., Baugh, R., McMullin, D. & Carter, T. (2008). Sun Earth Connection Coronal and Heliospheric Investigation (SECCHI). *Space Science Reviews*, **136**, 67–115. (Cited on pages 100, 103 and 106.)

Howard, T.A. & Tappin, S.J. (2009a). Interplanetary Coronal Mass Ejections Observed in the Heliosphere: 1. Review of Theory. *Space Science Reviews*, **147**, 31–54. (Cited on page 97.)

Howard, T.A. & Tappin, S.J. (2009b). Interplanetary Coronal Mass Ejections Observed in the Heliosphere: 1. Review of Theory. *Space Science Reviews*, **147**, 31–54. (Cited on page 110.)

Howard, T.A., Fry, C.D., Johnston, J.C. & Webb, D.F. (2007). On the Evolution of Coronal Mass Ejections in the Interplanetary Medium. *Astrophysical Journal*, **667**, 610–625. (Cited on page 105.)

Hundhausen, A. (1999). Coronal Mass Ejections. In K.T. Strong, J.L.R. Saba, B.M. Haisch & J.T. Schmelz, eds., *The many faces of the sun: a summary of the results from NASA's Solar Maximum Mission.*, 143. (Cited on page 22.)

Hundhausen, A.J. (1972). Coronal Expansion and Solar Wind. *Physics and Chemistry in Space*, **5**. (Cited on page 39.)

Illing, R.M.E. & Hundhausen, A.J. (1985). Observation of a coronal transient from 1.2 to 6 solar radii. *Journal of Geophysical Research*, **90**, 275–282. (Cited on page 23.)

Inan, U. & Golkowski, M. (2011). *Principles of Plasma Physics for Engineers and Scientists*. (Cited on pages 57 and 85.)

Kabin, K. (2001). A note on the compression ratio in MHD shocks. *Journal of Plasma Physics*, **66**, 259–274. (Cited on page 132.)

Kaiser, M.L., Kucera, T.A., Davila, J.M., St. Cyr, O.C., Guhathakurta, M. & Christian, E. (2008). The STEREO Mission: An Introduction. *Space Science Reviews*, **136**, 5–16. (Cited on pages 22, 99 and 106.)

Khan, J.I. & Aurass, H. (2002). X-ray observations of a large-scale solar coronal shock wave. *Astronomy & Astrophysics*, **383**, 1018–1031. (Cited on pages 38 and 48.)

Kim, R.S., Gopalswamy, N., Moon, Y.J., Cho, K.S. & Yashiro, S. (2012). Magnetic Field Strength in the Upper Solar Corona Using White-light Shock Structures Surrounding Coronal Mass Ejections. *Astrophysical Journal*, **746**, 118. (Cited on page 51.)

Klassen, A., Aurass, H., Mann, G. & Thompson, B.J. (2000). Catalogue of the 1997 SOHO-EIT coronal transient waves and associated type II radio burst spectra. *Astronomy & Astrophysics Supplemental*, **141**, 357–369. (Cited on page 47.)

Klassen, A., Bothmer, V., Mann, G., Reiner, M.J., Krucker, S., Vourlidas, A. & Kunow, H. (2002). Solar energetic electron events and coronal shocks. *Astronomy & Astrophysics*, **385**, 1078–1088. (Cited on page 48.)

Klein, K.L., Khan, J.I., Vilmer, N., Delouis, J.M. & Aurass, H. (1999). X-ray and radio evidence on the origin of a coronal shock wave. *Astronomy & Astrophysics*, **346**, L53–L56. (Cited on page 41.)

Kliem, B. & Török, T. (2006). Torus Instability. *Physical Review Letters*, **96**, 255002–+. (Cited on pages 105 and 123.)

Knock, S.A., Cairns, I.H., Robinson, P.A. & Kuncic, Z. (2001). Theory of type II radio emission from the foreshock of an interplanetary shock. *Journal of Geophysical Research*, **106**, 25041–25052. (Cited on page 91.)

Knock, S.A., Cairns, I.H., Robinson, P.A. & Kuncic, Z. (2003). Theoretically predicted properties of type II radio emission from an interplanetary foreshock. *Journal of Geophysical Research (Space Physics)*, **108**, 1126. (Cited on page 91.)

Kosugi, T. (1976). Type II-IV radio bursts and compact and diffuse white-light clouds in the outer corona of December 14, 1971. *Solar Physics*, **48**, 339–356. (Cited on page 39.)

Kozarev, K.A., Korreck, K.E., Lobzin, V.V., Weber, M.A. & Schwadron, N.A. (2011). Off-limb Solar Coronal Wavefronts from SDO/AIA Extreme-ultraviolet Observations - Implications for Particle Production. *Astrophysical Journal Letters*, **733**, L25. (Cited on page 48.)

Krall, J. & St. Cyr, O.C. (2006). Flux-Rope Coronal Mass Ejection Geometry and Its Relation to Observed Morphology. *Astrophysical Journal*, **652**, 1740–1746. (Cited on page 112.)

Krall, J., Chen, J., Duffin, R.T., Howard, R.A. & Thompson, B.J. (2001). Erupting Solar Magnetic Flux Ropes: Theory and Observation. *Astrophysical Journal*, **562**, 1045–1057. (Cited on pages 65, 72 and 74.)

Krucker, S., Larson, D.E., Lin, R.P. & Thompson, B.J. (1999). On the Origin of Impulsive Electron Events Observed at 1 AU. *Astrophysical Journal*, **519**, 864–875. (Cited on page 48.)

Lantos, P. (1999). Low Frequency Observations of the Quiet Sun: a Review. In T.S. Bastian, N. Gopalswamy & K. Shibasaki, eds., *Proceedings of the Nobeyama Symposium*, 11–24. (Cited on page 18.)

Lewis, D.J. & Simnett, G.M. (2002). Bulk flow velocities in the solar corona at solar maximum. *Monthly Notices of the Royal Astronomical Society*, **333**, 969–976. (Cited on page 34.)

Lin, C.H., Gallagher, P.T. & Raftery, C.L. (2010). Investigating the driving mechanisms of coronal mass ejections. *Astronomy & Astrophysics*, **516**, A44. (Cited on page 105.)

Lin, J. & Forbes, T.G. (2000). Effects of reconnection on the coronal mass ejection process. *Journal of Geophysical Research*, **105**, 2375–2392. (Cited on pages 66, 105 and 123.)

Lin, R.P., Levedahl, W.K., Lotko, W., Gurnett, D.A. & Scarf, F.L. (1986). Evidence for nonlinear wave-wave interactions in solar type III radio bursts. *Astrophysical Journal*, **308**, 954–965. (Cited on page 91.)

Lindemann, F. (1919). Note on the Theory of Magnetic Storms. *Philosophical Magazine Series 6*, **38**, 669. (Cited on page 21.)

Long, D.M., Gallagher, P.T., McAteer, R.T.J. & Bloomfield, D.S. (2011). Deceleration and dispersion of large-scale coronal bright fronts. *Astronomy & Astrophysics*, **531**, A42. (Cited on page 47.)

Lynch, B.J., Antiochos, S.K., MacNeice, P.J., Zurbuchen, T.H. & Fisk, L.A. (2004). Observable Properties of the Breakout Model for Coronal Mass Ejections. *Astrophysical Journal*, **617**, 589–599. (Cited on pages 69 and 71.)

Lynch, B.J., Antiochos, S.K., DeVore, C.R., Luhmann, J.G. & Zurbuchen, T.H. (2008). Topological Evolution of a Fast Magnetic Breakout CME in Three Dimensions. *Astrophysical Journal*, **683**, 1192–1206. (Cited on pages 70, 105 and 123.)

Lyot, B. (1939). The study of the solar corona and prominences without eclipses (George Darwin Lecture, 1939). *Monthly Notices of the Royal Astronomical Society*, **99**, 580. (Cited on page 98.)

MacNeice, P., Antiochos, S.K., Phillips, A., Spicer, D.S., DeVore, C.R. & Olson, K. (2004). A Numerical Study of the Breakout Model for Coronal Mass Ejection Initiation. *Astrophysical Journal*, **614**, 1028–1041. (Cited on page 71.)

MacQueen, R.M., Csoeke-Poeckh, A., Hildner, E., House, L., Reynolds, R., Stanger, A., Tepoel, H. & Wagner, W. (1980). The High Altitude Observatory Coronagraph/Polarimeter on the Solar Maximum Mission. *Solar Physics*, **65**, 91–107. (Cited on page 22.)

Magdalenić, J., Marqué, C., Zhukov, A.N., Vršnak, B. & Veronig, A. (2012). Flare-generated Type II Burst without Associated Coronal Mass Ejection. *Astrophysical Journal*, **746**, 152. (Cited on page 41.)

Maia, D., Pick, M., Vourlidas, A. & Howard, R. (2000). Development of Coronal Mass Ejections: Radio Shock Signatures. *Astrophysical Journal Letters*, **528**, L49–L51. (Cited on pages 40 and 41.)

Maia, D.J.F. & Pick, M. (2004). Revisiting the Origin of Impulsive Electron Events: Coronal Magnetic Restructuring. *Astrophysical Journal*, **609**, 1082–1097. (Cited on page 49.)

MALONEY, S.A. & GALLAGHER, P.T. (2010). Solar Wind Drag and the Kinematics of Interplanetary Coronal Mass Ejections. *Astrophysical Journal Letters*, **724**, L127–L132. (Cited on pages 105 and 123.)

MALONEY, S.A. & GALLAGHER, P.T. (2011). STEREO Direct Imaging of a Coronal Mass Ejection-driven Shock to 0.5 AU. *Astrophysical Journal Letters*, **736**, L5. (Cited on page 51.)

MANCUSO, S. (2011). Combined Analysis of Ultraviolet and Radio Observations of the 7 May 2004 CME/Shock Event. *Solar Physics*, **273**, 511–523. (Cited on page 41.)

MANCUSO, S. & RAYMOND, J.C. (2004). Coronal transients and metric type II radio bursts. I. Effects of geometry. *Astronomy & Astrophysics*, **413**, 363–371. (Cited on pages 41 and 43.)

MANN, G. & CLASSEN, H.T. (1995). Electron acceleration to high energies at quasi-parallel shock waves in the solar corona. *Astronomy & Astrophysics*, **304**, 576. (Cited on page 43.)

MANN, G. & KLASSEN, A. (2005). Electron beams generated by shock waves in the solar corona. *Astronomy & Astrophysics*, **441**, 319–326. (Cited on pages 43 and 84.)

MANN, G., KLASSEN, A., CLASSEN, H.T., AURASS, H., SCHOLZ, D., MACDOWALL, R.J. & STONE, R.G. (1996). Catalogue of solar type II radio bursts observed from September 1990 to December 1993 and their statistical analysis. *Astronomy & Astrophysics Supplemental*, **119**, 489–498. (Cited on page 37.)

MANN, G., JANSEN, F., MACDOWALL, R.J., KAISER, M.L. & STONE, R.G. (1999). A heliospheric density model and type III radio bursts. *Astronomy & Astrophysics*, **348**, 614–620. (Cited on pages 123 and 124.)

MANOHARAN, P.K. & KUNDU, M.R. (2003). Coronal Structure of a Flaring Region and Associated Coronal Mass Ejection. *Astrophysical Journal*, **592**, 597–606. (Cited on page 105.)

MAXWELL, A. & THOMPSON, A.R. (1962). Spectral Observations of Solar Radio Bursts. II. Slow-Drift Bursts and Coronal Streamers. *Astrophysical Journal*, **135**, 138. (Cited on page 39.)

MELROSE, D.B. (1986). *Instabilities in Space and Laboratory Plasmas*. Cambridge University Press. (Cited on page 88.)

Melrose, D.B. (1989). *Instabilities in Space and Laboratory Plasmas*. (Cited on pages 86 and 87.)

Mierla, M., Inhester, B., Marqué, C., Rodriguez, L., Gissot, S., Zhukov, A.N., Berghmans, D. & Davila, J. (2009). On 3D Reconstruction of Coronal Mass Ejections: I. Method Description and Application to SECCHI-COR Data. *Solar Physics*, **259**, 123–141. (Cited on page 25.)

Mikheev, S.P. & Smirnov, A.I. (1986). Resonant amplification of neutrino oscillations in matter and solar-neutrino spectroscopy. *Nuovo Cimento C Geophysics Space Physics C*, **9**, 17–26. (Cited on page 5.)

Minnaert, M. (1930). On the continuous spectrum of the corona and its polarisation. With 3 figures. (Received July 30, 1930). *Zeitschrift fur Astrophysik*, **1**, 209–+. (Cited on pages 106 and 110.)

Mitalas, R. & Sills, K.R. (1992). On the photon diffusion time scale for the sun. *Astrophysical Journal*, **401**, 759. (Cited on page 5.)

Miteva, R. & Mann, G. (2007). The electron acceleration at shock waves in the solar corona. *Astronomy & Astrophysics*, **474**, 617–625. (Cited on page 43.)

Moon, Y.J., Choe, G.S., Wang, H., Park, Y.D., Gopalswamy, N., Yang, G. & Yashiro, S. (2002). A Statistical Study of Two Classes of Coronal Mass Ejections. *Astrophysical Journal*, **581**, 694–702. (Cited on page 26.)

Moran, T.G. & Davila, J.M. (2004). Three-Dimensional Polarimetric Imaging of Coronal Mass Ejections. *Science*, **305**, 66–71. (Cited on page 24.)

Moses, D., Clette, F., Delaboudinière, J.P., Artzner, G.E., Bougnet, M., Brunaud, J., Carabetian, C., Gabriel, A.H., Hochedez, J.F., Millier, F., Song, X.Y., Au, B., Dere, K.P., Howard, R.A., Kreplin, R., Michels, D.J., Defise, J.M., Jamar, C., Rochus, P., Chauvineau, J.P., Marioge, J.P., Catura, R.C., Lemen, J.R., Shing, L., Stern, R.A., Gurman, J.B., Neupert, W.M., Newmark, J., Thompson, B., Maucherat, A., Portier-Fozzani, F., Berghmans, D., Cugnon, P., van Dessel, E.L. & Gabryl, J.R. (1997). EIT Observations of the Extreme Ultraviolet Sun. *Solar Physics*, **175**, 571–599. (Cited on page 46.)

Munro, R.H., Gosling, J.T., Hildner, E., MacQueen, R.M., Poland, A.I. & Ross, C.L. (1979). The association of coronal mass ejection transients with other forms of solar activity. *Solar Physics*, **61**, 201–215. (Cited on pages 31 and 106.)

Nelson, G.J. & Melrose, D.B. (1985). *Type II bursts*, 333–359. (Cited on page 37.)

Ontiveros, V. & Vourlidas, A. (2009). Quantitative Measurements of Coronal Mass Ejection-Driven Shocks from LASCO Observations. *Astrophysical Journal*, **693**, 267–275. (Cited on page 51.)

Parker, E.N. (1963). The Solar-Flare Phenomenon and the Theory of Reconnection and Annihiliation of Magnetic Fields. *Astrophysical Journal Supplemental Series*, **8**, 177. (Cited on page 62.)

Payne-Scott, R., Yabsley, D.E. & Bolton, J.G. (1947). Relative Times of Arrival of Bursts of Solar Noise on Different Radio Frequencies. *Nature*, **160**, 256–257. (Cited on page 38.)

Petschek, H.E. (1964). Magnetic Field Annihilation. *NASA Special Publication*, **50**, 425. (Cited on page 64.)

Phillips, K.J.H., Feldman, U. & Landi, E. (2008). *Ultraviolet and X-ray Spectroscopy of the Solar Atmosphere*. Cambridge University Press. (Cited on pages 14 and 15.)

Pick, M. & Vilmer, N. (2008). Sixty-five years of solar radioastronomy: flares, coronal mass ejections and Sun Earth connection. *Astronomy & Astrophysics Review*, **16**, 1–153. (Cited on page 45.)

Pick, M., Forbes, T.G., Mann, G., Cane, H.V., Chen, J., Ciaravella, A., Cremades, H., Howard, R.A., Hudson, H.S., Klassen, A., Klein, K.L., Lee, M.A., Linker, J.A., Maia, D., Mikic, Z., Raymond, J.C., Reiner, M.J., Simnett, G.M., Srivastava, N., Tripathi, D., Vainio, R., Vourlidas, A., Zhang, J., Zurbuchen, T.H., Sheeley, N.R. & Marqué, C. (2006). Multi-Wavelength Observations of CMEs and Associated Phenomena. Report of Working Group F. *Space Science Reviews*, **123**, 341–382. (Cited on page 23.)

Poland, A.I., Howard, R.A., Koomen, M.J., Michels, D.J. & Sheeley, N.R., Jr. (1981). Coronal transients near sunspot maximum. *Solar Physics*, **69**, 169–175. (Cited on pages 31 and 106.)

Priest, E. & Forbes, T. (2000). *Magnetic Reconnection*. (Cited on pages 66, 67, 68 and 80.)

Priest, E.R. & Forbes, T.G. (1986). New models for fast steady state magnetic reconnection. *Journal of Geophysical Research*, **91**, 5579–5588. (Cited on page 64.)

Reiner, M.J., Kaiser, M.L., Gopalswamy, N., Aurass, H., Mann, G., Vourlidas, A. & Maksimovic, M. (2001). Statistical analysis of coronal shock dynamics implied by radio and white-light observations. *Journal of Geophysical Research*, **106**, 25279–25290. (Cited on pages 41 and 42.)

Robbrecht, E., Berghmans, D. & Van der Linden, R.A.M. (2009). Automated LASCO CME Catalog for Solar Cycle 23: Are CMEs Scale Invariant? *Astrophysical Journal*, **691**, 1222–1234. (Cited on page 24.)

Robinson, P.A. & Cairns, I.H. (1993). Stochastic Growth Theory of Type III Solar Radio Emission. *Astrophysical Journal*, **418**, 506. (Cited on pages 90 and 91.)

Robinson, P.A. & Cairns, I.H. (1998). Fundamental and Harmonic Emission in Type III Solar Radio Bursts - II. Dominant Modes and Dynamic Spectra. *Solar Physics*, **181**, 395–428. (Cited on page 91.)

Robinson, P.A., Willes, A.J. & Cairns, I.H. (1993). Dynamics of Langmuir and ion-sound waves in type III solar radio sources. *Astrophysical Journal*, **408**, 720–734. (Cited on page 88.)

Robinson, P.A., Cairns, I.H. & Willes, A.J. (1994). Dynamics and efficiency of type III solar radio emission. *Astrophysical Journal*, **422**, 870–882. (Cited on page 88.)

ROBINSON, R.D. & STEWART, R.T. (1985). A positional comparison between coronal mass ejection events and solar type II bursts. *Solar Physics*, **97**, 145–157. (Cited on page 40.)

RUSSELL, C.T. & MULLIGAN, T. (2002). On the magnetosheath thicknesses of interplanetary coronal mass ejections. *Planet. Space Sci.*, **50**, 527–534. (Cited on page 51.)

RUST, D.M. (1972). Flares and Changing Magnetic Fields. *Solar Physics*, **25**, 141–157. (Cited on page 66.)

SCHMIDT, J.M. & CAIRNS, I.H. (2012a). Type II radio bursts: 1. New entirely analytic formalism for the electron beams, Langmuir waves, and radio emission. *Journal of Geophysical Research (Space Physics)*, **117**, 4106. (Cited on page 91.)

SCHMIDT, J.M. & CAIRNS, I.H. (2012b). Type II radio bursts: 2. Application of the new analytic formalism. *Journal of Geophysical Research (Space Physics)*, **117**, 11104. (Cited on page 84.)

SCHRIJVER, C.J., ELMORE, C., KLIEM, B., TÖRÖK, T. & TITLE, A.M. (2008). Observations and Modeling of the Early Acceleration Phase of Erupting Filaments Involved in Coronal Mass Ejections. *Astrophysical Journal*, **674**, 586–595. (Cited on pages 65 and 74.)

SHEELEY, N.R., WALTERS, J.H., WANG, Y.M. & HOWARD, R.A. (1999). Continuous tracking of coronal outflows: Two kinds of coronal mass ejections. *Journal of Geophysical Research*, **104**, 24739–24768. (Cited on page 26.)

SHEELEY, N.R., JR., MICHELS, D.J., HOWARD, R.A. & KOOMEN, M.J. (1980). Initial observations with the SOLWIND coronagraph. *Astrophysical Journal Letters*, **237**, L99–L101. (Cited on page 22.)

SHEELEY, N.R., JR., WANG, Y.M., HAWLEY, S.H., BRUECKNER, G.E., DERE, K.P., HOWARD, R.A., KOOMEN, M.J., KORENDYKE, C.M., MICHELS, D.J., PASWATERS, S.E., SOCKER, D.G., ST. CYR, O.C., WANG, D., LAMY, P.L., LLEBARIA, A., SCHWENN, R., SIMNETT, G.M., PLUNKETT, S. & BIESECKER, D.A. (1997). Measurements of Flow Speeds in the Corona between 2 and 30 R sub sun. *Astrophysical Journal*, **484**, 472. (Cited on page 35.)

SONNERUP, B.U.Ö. (1970). Magnetic-field re-connexion in a highly conducting incompressible fluid. *Journal of Plasma Physics*, **4**, 161. (Cited on page 64.)

SPITZER, L. (1962). *Physics of Fully Ionized Gases*. (Cited on page 61.)

SPREITER, J.R., SUMMERS, A.L. & ALKSNE, A.Y. (1966). Hydromagnetic flow around the magnetosphere. *Planet. Space Sci.*, **14**, 223. (Cited on page 51.)

STEELE, C.D.C., HOOD, A.W., PRIEST, E.R. & AMARI, T. (1989). Non-equilibrium of a cylindrical magnetic arcade. *Solar Physics*, **123**, 127–141. (Cited on page 69.)

STEWART, R.T. & MAGUN, A. (1980). Radio evidence for electron acceleration by transverse shock waves in herringbone Type II solar bursts. *Proceedings of the Astronomical Society of Australia*, **4**, 53–55. (Cited on page 45.)

STEWART, R.T., MCCABE, M.K., KOOMEN, M.J., HANSEN, R.T. & DULK, G.A. (1974). Observations of Coronal Disturbances from 1 to 9 R_{sun}. I: First Event of 1973, January 11. *Solar Physics*, **36**, 203–217. (Cited on page 39.)

STURROCK, P.A. (1964). Type III Solar Radio Bursts. *NASA Special Publication*, **50**, 357. (Cited on page 90.)

STURROCK, P.A. (1991). Maximum energy of semi-infinite magnetic field configurations. *Astrophysical Journal*, **380**, 655–659. (Cited on page 70.)

SUBRAMANIAN, P. & VOURLIDAS, A. (2007). Energetics of solar coronal mass ejections. *Astronomy & Astrophysics*, **467**, 685–693. (Cited on page 34.)

SWEET, P.A. (1958). The Neutral Point Theory of Solar Flares. In B. Lehnert, ed., *Electromagnetic Phenomena in Cosmical Physics*, vol. 6 of *IAU Symposium*, 123. (Cited on page 62.)

TEMMER, M., VERONIG, A.M., KONTAR, E.P., KRUCKER, S. & VRŠNAK, B. (2010). Combined STEREO/RHESSI Study of Coronal Mass Ejection Acceleration and Particle Acceleration in Solar Flares. *Astrophysical Journal*, **712**, 1410–1420. (Cited on page 28.)

THERNISIEN, A.F.R., HOWARD, R.A. & VOURLIDAS, A. (2006). Modeling of Flux Rope Coronal Mass Ejections. *Astrophysical Journal*, **652**, 763–773. (Cited on page 25.)

Thompson, B.J. & Myers, D.C. (2009). A Catalog of Coronal "EIT Wave" Transients. *Astrophysical Journal Supplemental Series*, **183**, 225–243. (Cited on page 47.)

Thompson, B.J., Plunkett, S.P., Gurman, J.B., Newmark, J.S., St. Cyr, O.C. & Michels, D.J. (1998). SOHO/EIT observations of an Earth-directed coronal mass ejection on May 12, 1997. *Geophysical Research Letters*, **25**, 2465–2468. (Cited on pages 46 and 47.)

Thompson, M.J., Christensen-Dalsgaard, J., Miesch, M.S. & Toomre, J. (2003). The Internal Rotation of the Sun. *Annual Review of Astronomy & Astrophysics*, **41**, 599–643. (Cited on page 8.)

Thompson, W.T. & Reginald, N.L. (2008). The Radiometric and Pointing Calibration of SECCHI COR1 on STEREO. *Solar Physics*, **250**, 443–454. (Cited on pages 100 and 102.)

Tousey, R. (1973). The solar corona. In M. J. Rycroft & S. K. Runcorn, ed., *Space Research XIII, Vol. 2, p. 713 - 730*, 713–730. (Cited on page 22.)

Turck-Chièze, S. & Couvidat, S. (2011). Solar neutrinos, helioseismology and the solar internal dynamics. *Reports on Progress in Physics*, **74**, 086901. (Cited on pages 4, 6 and 7.)

Uchida, Y. (1960). On the Exciters of Type II and Type III Solar Radio Bursts. *Publications of the Astronomical Society of Japan*, **12**, 376. (Cited on page 39.)

Uchida, Y. (1974). Behavior of the flare produced coronal MHD wavefront and the occurrence of type II radio bursts. *Solar Physics*, **39**, 431–449. (Cited on page 39.)

van de Hulst, H.C. (1950). The electron density of the solar corona. *Bulletin of the Astronomical Institutes of the Netherlands*, **11**, 135. (Cited on pages 106 and 110.)

Vandas, M. & Karlický, M. (2011). Electron acceleration in a wavy shock front. *Astronomy & Astrophysics*, **531**, A55. (Cited on page 44.)

Vernazza, J.E., Avrett, E.H. & Loeser, R. (1981). Structure of the solar chromosphere. III - Models of the EUV brightness components of the quiet-sun. *Astrophysical Journal Supplemental Series*, **45**, 635–725. (Cited on pages 14, 15 and 16.)

Veronig, A.M., Muhr, N., Kienreich, I.W., Temmer, M. & Vršnak, B. (2010). First Observations of a Dome-shaped Large-scale Coronal Extreme-ultraviolet Wave. *Astrophysical Journal Letters*, **716**, L57–L62. (Cited on page 47.)

Vourlidas, A. & Bemporad, A. (2012). A decade of coronagraphic and spectroscopic studies of CME-driven shocks. In J. Heerikhuisen, G. Li, N. Pogorelov & G. Zank, eds., *American Institute of Physics Conference Series*, vol. 1436 of *American Institute of Physics Conference Series*, 279–284. (Cited on page 50.)

Vourlidas, A., Subramanian, P., Dere, K.P. & Howard, R.A. (2000). Large-Angle Spectrometric Coronagraph Measurements of the Energetics of Coronal Mass Ejections. *Astrophysical Journal*, **534**, 456–467. (Cited on pages 31, 32, 33, 106, 111, 112, 121 and 125.)

Vourlidas, A., Buzasi, D., Howard, R.A. & Esfandiari, E. (2002). Mass and energy properties of LASCO CMEs. In A. Wilson, ed., *Solar Variability: From Core to Outer Frontiers*, vol. 506 of *ESA Special Publication*, 91–94. (Cited on pages 31 and 106.)

Vourlidas, A., Wu, S.T., Wang, A.H., Subramanian, P. & Howard, R.A. (2003). Direct Detection of a Coronal Mass Ejection-Associated Shock in Large Angle and Spectrometric Coronagraph Experiment White-Light Images. *Astrophysical Journal*, **598**, 1392–1402. (Cited on page 51.)

Vourlidas, A., Howard, R.A., Esfandiari, E., Patsourakos, S., Yashiro, S. & Michalek, G. (2010). Comprehensive Analysis of Coronal Mass Ejection Mass and Energy Properties Over a Full Solar Cycle. *Astrophysical Journal*, **722**, 1522–1538. (Cited on pages 21, 31, 32, 34, 106, 112, 121, 122 and 126.)

Vourlidas, A., Lynch, B.J., Howard, R.A. & Li, Y. (2013). How Many CMEs Have Flux Ropes? Deciphering the Signatures of Shocks, Flux Ropes, and Prominences in Coronagraph Observations of CMEs. *Solar Physics*, **284**, 179–201. (Cited on page 50.)

Vršnak, B. (2006). Forces governing coronal mass ejections. *Advances in Space Research*, **38**, 431–440. (Cited on pages 35, 36 and 125.)

Vršnak, B. & Cliver, E.W. (2008). Origin of Coronal Shock Waves. Invited Review. *Solar Physics*, **253**, 215–235. (Cited on page 41.)

VRŠNAK, B. & GOPALSWAMY, N. (2002). Influence of the aerodynamic drag on the motion of interplanetary ejecta. *Journal of Geophysical Research (Space Physics)*, **107**, 1019. (Cited on page 132.)

VRŠNAK, B., MAGDALENIĆ, J. & ZLOBEC, P. (2004). Band-splitting of coronal and interplanetary type II bursts. III. Physical conditions in the upper corona and interplanetary space. *Astronomy and Astrophysics*, **413**, 753–763. (Cited on page 133.)

VRŠNAK, B., SUDAR, D. & RUŽDJAK, D. (2005). The CME-flare relationship: Are there really two types of CMEs? *Astronomy & Astrophysics*, **435**, 1149–1157. (Cited on pages 26 and 48.)

VRŠNAK, B., MARIČIĆ, D., STANGER, A.L., VERONIG, A.M., TEMMER, M. & ROŠA, D. (2007). Acceleration Phase of Coronal Mass Ejections: I. Temporal and Spatial Scales. *Solar Physics*, **241**, 85–98. (Cited on page 28.)

WANG, Y.M. (2000). EIT Waves and Fast-Mode Propagation in the Solar Corona. *Astrophysical Journal Letters*, **543**, L89–L93. (Cited on page 47.)

WARMUTH, A., VRŠNAK, B., MAGDALENIĆ, J., HANSLMEIER, A. & OTRUBA, W. (2004). A multiwavelength study of solar flare waves. II. Perturbation characteristics and physical interpretation. *Astronomy & Astrophysics*, **418**, 1117–1129. (Cited on page 47.)

WEBB, D.F. & HOWARD, T.A. (2012). Coronal Mass Ejections: Observations. *Living Reviews in Solar Physics*, **9**, 3. (Cited on page 26.)

WEBB, D.F. & HUNDHAUSEN, A.J. (1987). Activity associated with the solar origin of coronal mass ejections. *Solar Physics*, **108**, 383–401. (Cited on page 23.)

WILD, J.P. (1964). Radio Observations of Solar Flares. *NASA Special Publication*, **50**, 161. (Cited on page 45.)

WILD, J.P., MURRAY, J.D. & ROWE, W.C. (1954). Harmonics in the Spectra of Solar Radio Disturbances. *Australian Journal of Physics*, **7**, 439. (Cited on page 38.)

WILD, J.P., SHERIDAN, K.V. & TRENT, G.H. (1959). The transverse motions of the sources of solar radio bursts. In R.N. Bracewell, ed., *URSI Symp. 1: Paris Symposium on Radio Astronomy*, vol. 9 of *IAU Symposium*, 176. (Cited on page 21.)

WILD, J.P., SMERD, S.F. & WEISS, A.A. (1963). Solar Bursts. *Annual Review of Astronomy & Astrophysics*, **1**, 291. (Cited on page 22.)

WOLFENSTEIN, L. (1978). Neutrino oscillations in matter. *Physical Review Letters*, **17**, 2369–2374. (Cited on page 5.)

WOLFSON, R. & SARAN, S. (1998). Energetics of Coronal Mass Ejections: Role of the Streamer Cavity. *Astrophysical Journal*, **499**, 496. (Cited on page 65.)

WU, C.S. (1984). A fast Fermi process - Energetic electrons accelerated by a nearly perpendicular bow shock. *Journal of Geophysical Research*, **89**, 8857–8862. (Cited on page 84.)

YASHIRO, S., GOPALSWAMY, N., MICHALEK, G., ST. CYR, O.C., PLUNKETT, S.P., RICH, N.B. & HOWARD, R.A. (2004). A catalog of white light coronal mass ejections observed by the SOHO spacecraft. *Journal of Geophysical Research (Space Physics)*, **109**, 7105. (Cited on pages 24, 25 and 26.)

YURCHYSHYN, V., YASHIRO, S., ABRAMENKO, V., WANG, H. & GOPALSWAMY, N. (2005). Statistical Distributions of Speeds of Coronal Mass Ejections. *Astrophysical Journal*, **619**, 599–603. (Cited on pages 26 and 27.)

ZHANG, J. & DERE, K.P. (2006). A Statistical Study of Main and Residual Accelerations of Coronal Mass Ejections. *Astrophysical Journal*, **649**, 1100–1109. (Cited on pages 27, 29 and 36.)

ZHANG, J., DERE, K.P., HOWARD, R.A., KUNDU, M.R. & WHITE, S.M. (2001). On the Temporal Relationship between Coronal Mass Ejections and Flares. *Astrophysical Journal*, **559**, 452–462. (Cited on pages 29, 30, 121 and 125.)

ZHANG, J., DERE, K.P., HOWARD, R.A. & VOURLIDAS, A. (2004). A Study of the Kinematic Evolution of Coronal Mass Ejections. *Astrophysical Journal*, **604**, 420–432. (Cited on pages 29, 121 and 125.)

ZLOBEC, P., MESSEROTTI, M., KARLICKY, M. & URBARZ, H. (1993). Fine structures in time profiles of type II bursts at frequencies above 200 MHz. *Solar Physics*, **144**, 373–384. (Cited on page 44.)